S.T. Yau High School Science Award

Research Report

The Team

Name of team member: Evan Xie

School: Deerfield Academy

City, Country: 7 Boyden Ln, Deerfield, MA 01342 USA

Name of supervising teacher: Xijun Wang

Job Title: Postdoctoral Scholar

School/Institution: Northwestern University

City, Country: 633 Clark St, Evanston, IL 60208 USA

Title of Research Report

Computational and AI-Assisted Design of Dual-Metal Single-Atom Catalyst for Oxygen Reduction Reaction

Date: 8/18/2023

Title: Computational and AI-Assisted Design of Dual-Metal Single-Atom Catalyst for Oxygen Reduction Reaction

Author: Evan Xie Research Instructor: Dr. Xijun Wang

Abstract

The electrocatalytic oxygen reduction reaction (ORR) plays a crucial role in numerous energy and sustainability systems, such as fuel cells, metal-air batteries, and water electrolysers. It holds significant potential for renewable energy generation, transportation, and storage, heralding a cleaner and more sustainable future. Recent trends have shown increased use of single-atom catalysts (SACs), particularly metal-N_4 moieties grown on graphene-based 2D materials, for enhancing ORR efficiency. However, the rational design of SACs for high-performance ORR faces challenges due to unclear structure-property relationships and the limits of conventional experimental trial-and-error approaches. In this study, we leveraged the power of the density functional theory (DFT) calculations, combined with cutting-edge machine learning (ML) techniques, to explore 144 SACs featuring dual interacting M_1-N_4 and M_2-N_4 moieties (M_1, M_2 = Mn, Fe, Co, Ni, Cu, Ru, Rh, Pd, Ag Ir, Pt, Au), denoted as M_1-M_2, grown on graphene. Of all the catalysts we examined, Fe-Pd emerged as the top performer, achieving an impressive overpotential of 0.980 V in alkaline conditions — outperforming most previously reported SACs. Even more striking, 25 of the evaluated SACs surpassed the renowned Fe-N_4 SAC in catalytic efficiency, including more economically viable alternatives like Fe-Ag. Venturing further, we developed three ML models that accurately predict the overpotentials of various M_1-M_2 SACs, showing their strong ability to capture the relationship between single-atom metal site properties and overpotential. These models provide useful navigation toolkits for the rational design of effective electrocatalysts. Our study sheds light on the path toward achieving efficient SAC-catalyzed ORR, contributing to a more sustainable and energy-efficient future.

Keywords: single-atom catalyst, oxygen reduction reaction, density functional theory, machine learning, catalysis

Acknowledgment

In an ever-evolving society, it becomes crucial not to overlook the impacts we leave behind. To address this challenge, I dedicated myself to researching clean and efficient energy storage and conversion through catalysis.

I would like to thank Dr. Xijun Wang, whose guidance and support made this project possible. Under his mentorship, I independently conducted computational chemistry calculations to explore the properties of single atom catalysts. Using these properties, I developed a highly effective SISSO model capable of predicting the catalytic performance of these materials. The analysis of the results was carried out with inspiration from Dr. Wang, and I took responsibility for writing the final thesis.

I am particularly thankful for the S.T. Yau High School Science Award for providing me with a platform to present my findings. This recognition encouraged and motivated me to delve deeper into the realm of catalysis and its potential positive impact on energy and sustainability.

Commitments on Academic Honesty and Integrity

We hereby declare that we

1. are fully committed to the principle of honesty, integrity and fair play throughout the competition.
2. actually perform the research work ourselves and thus truly understand the content of the work.
3. observe the common standard of academic integrity adopted by most journals and degree theses.
4. have declared all the assistance and contribution we have received from any personnel, agency, institution, etc. for the research work.
5. undertake to avoid getting in touch with assessment panel members in a way that may lead to direct or indirect conflict of interest.
6. undertake to avoid any interaction with assessment panel members that would undermine the neutrality of the panel member and fairness of the assessment process.
7. observe the safety regulations of the laboratory(ies) where we conduct the experiment(s), if applicable.
8. observe all rules and regulations of the competition.
9. agree that the decision of YHSA is final in all matters related to the competition.

We understand and agree that failure to honour the above commitments may lead to disqualification from the competition and/or removal of reward, if applicable; that any unethical deeds, if found, will be disclosed to the school principal of team member(s) and relevant parties if deemed necessary; and that the decision of YHSA is final and no appeal will be accepted.

(Signatures of full team below)

X Evan Xie

Name of team member: Evan Xie

X Xijun Wang

Name of supervising teacher: Xijun Wang

Declaration of Academic Integrity

The participating team declares that the paper submitted is comprised of original research and results obtained under the guidance of the instructor. To the team's best knowledge, the paper does not contain research results, published or not, from a person who is not a team member, except for the content listed in the references and the acknowledgment. If there is any misinformation, we are willing to take all the related responsibilities.

Names of team members: Evan Xie

Signatures of team members: Evan Xie

Name of the instructor: Xijun Wang

Signature of the instructor: Xijun Wang

Date: 8/18/2023

Table of Contents

1. Introduction

Oxygen Reduction Reaction (ORR) is a fundamental electrochemical process that plays a crucial role in numerous energy conversion systems and technologies. It involves the reduction of oxygen molecules to form water or other oxygen-containing species[1]. The significance of ORR lies in its direct connection to practical applications, particularly in fuel cells and metal-air batteries, which are considered promising alternatives to conventional combustion-based power sources due to their environmental benefits and high energy efficiency[1-4]. For example, in the galvanic battery reaction (Figure 1a), ORR occurs at the cathode, where oxygen reacts with electrons and protons to produce water (Figure 1b). This reaction is crucial for generating electricity in fuel cells, which have the potential to power various transportation modes and provide clean energy for industrial and residential sectors. Similarly, in metal-air batteries[5], ORR takes place during the discharge phase, where oxygen is reduced to form metal oxides and release electrical energy.

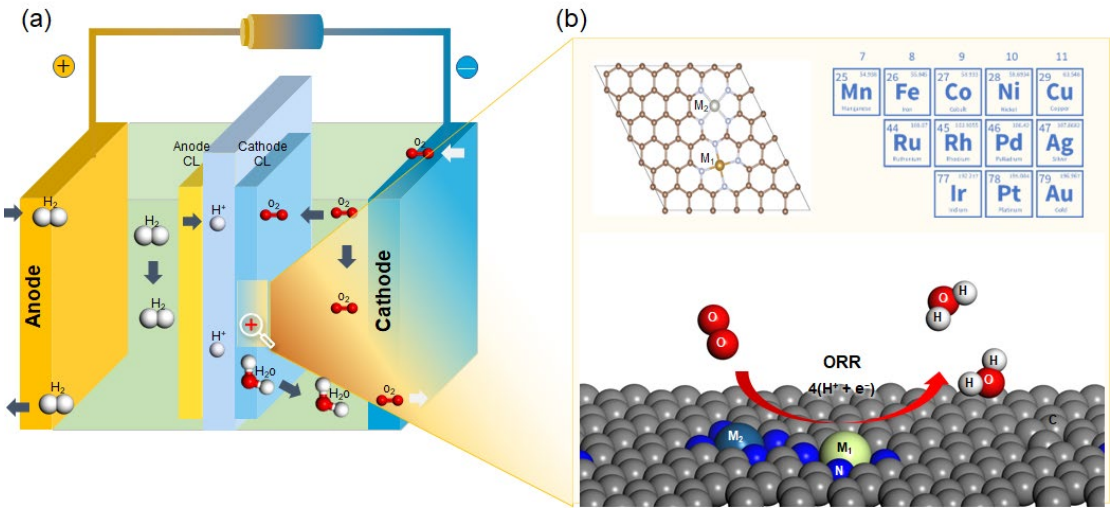

Figure 1. Schematic illustration of (a) the galvanic battery reaction and (b) ORR on M_1-M_2 SACs.

Efficient ORR is paramount for improving the overall performance and longevity of these energy conversion systems. To date, various materials and catalysts have been utilized to facilitate ORR, including Pt-based electrocatalysts[6], carbon nanotubes[7], and transition metals alloys[8]. However, the challenge lies in finding cost-effective catalysts that can enhance the kinetics of the ORR process and reduce energy losses. Researchers and engineers continue to explore new materials and design strategies to enhance ORR efficiency. Among many types of materials, single-atom catalysts (SACs) stand out because of their minimal metal usage, superior efficiency, and

enhanced selectivity[9-11]. Recently, Chen, Ji, *et al.* suggested a metal-organic framework (MOF) supported Fe SAC[12], which demonstrated excellent stability and catalytic performance with a positive half-wave potential of 0.912 V vs. Reversible Hydrogen Electrode (RHE). Liu *et al.* designed carbon-supported Pt SACs to improve the durability and efficiency of Pt SACs, achieving a positive half-wave potential of 0.87 vs RHE[13]. Rao *et al.* used novel "plasma bombing" strategies to design cheap Co single site SACs for enhanced ORR kinetics, with a Tafel slope of 79 mV dec^{-1} [14]. These pioneering studies highlighted the efficacy and potential of SACs in enhancing ORR.

While researchers have made considerable progress in the development of SACs, the rational design of high-performance SACs for ORR remains a challenging task, primarily due to the limited understanding of the complex structure-property relationships governing their catalytic activity, especially at the atomic level[15]. Conventional experimental trial-and-error approaches often suffer from inefficiency and high costs. The iterative nature of this method necessitates a large number of time-consuming experiments and extensive materials testing, resulting in significant resource expenditure. Moreover, without a thorough comprehension of the underlying mechanisms, the outcomes of these experiments may lack consistency and fail to reach their full potential.

To address these challenges and accelerate SAC design, quantum chemistry methods, especially at the first-principles density functional theory (DFT) level[16,17], have been increasingly applied as powerful toolkits to enable a more systematic approach to predict and understand the catalytic behaviors of catalysts[18,19]. These techniques empower researchers to explore a wide range of potential catalyst configurations and identify promising candidates for experimental synthesis, reducing the number of trial-and-error experiments and streamlining the design process. For example, Deng *et al.* adopted DFT to develop Co-based SACs on defective boron nitride (Co/BN) for efficient ORR[20]. Similarly, Yang *et al.* employed DFT to quantify the performance of two-dimensional conjugated aromatic networks (CAN) with a high single-metal-atom-site density that surpassed the performance of a conventional ORR catalyst, Pt/C SAC[21]. Further, Han *et al.* conducted DFT calculations to explore the ORR reaction mechanism and to evaluate the impact of the modulation effect on the ORR performance of Fe-N_4/Pt-N_4 SACs[22].

In recent years, there has been a notable surge in the utilization of cutting-edge machine learning (ML) techniques for materials design[23-25]. By training predictive models on data from

theoretical simulations, researchers have rapidly and accurately screened promising catalytic materials for various applications, including ORR[26,27]. This innovative approach has substantially minimized the need for time-consuming DFT calculations and tedious experimental trial-and-error processes. Furthermore, the integration of DFT and ML offers in-depth insights into the intricate structure-property relationships governing catalyst activity, providing essential guidance for the rational design of SACs. This thereby accelerates the development of efficient and sustainable SACs for enhanced ORR, propelling the progress of clean energy technologies and addressing pressing environmental challenges.

In this study, using DFT and ML, we exhaustively investigated the ORR activity of 144 SACs with two M-N_4 moieties, denoted as M_1-M_2, where M_1 and M_2 = Mn, Fe, Ni, Co, Cu, Ru, Rh, Pd, Ag, Ir, Pt, Au (Figure 1b). These late transition metals were selected due to their promising potential in catalytic applications, especially ORR[28-31]. For each of the 144 SACs, we assessed their ORR performance by determining their overpotential, which refers to the extra voltage necessary beyond the theoretical potential to drive the ORR at a desired rate. Through extensive overpotential calculations under alkaline conditions (pH = 13), we discovered twenty-five highly active SACs that exhibit superior performance compared to pristine Fe-N_4 SACs, previously regarded as active catalysts for ORR. Notably, we identified the Fe-Pd system as the most active SAC among all those investigated. Its overpotential (0.980 V) is even slightly lower than that of the previously discovered Fe-Pt SAC[22]. Furthermore, we found economical alternatives such as Fe-Ag, which exhibit comparable ORR activity with an overpotential of 1.008 V but at a significantly reduced cost. More intriguingly, we harnessed multiple ML methods to investigate the correlation between the intrinsic properties of the single-atom sites and their corresponding overpotentials. These ML models demonstrated high predictive power in estimating the overpotential, thereby effectively predicting promising SAC materials for ORR. These findings illuminate the ORR capabilities of various SAC materials, greatly broadening our understanding of material design and providing theoretical guidance for the future design and optimization of SAC materials, holding implications that transcend the realm of ORR.

2. Methodology

2.1. ORR Pathways

This study primarily focuses on the 4-electron pathway, the most prevalent and desired pathway for ORR. This pathway directly produces water, avoiding the production of intermediate hydrogen peroxide seen in the 2-electron pathway. The reaction, $O_2 + 4H^+ + 4e^- \rightarrow 2H_2O$ ($4e^-$ process), can be broken down into four steps:

(1) $O_2 + H_2O + e^- \rightarrow OOH^* + OH^-$

(2) $OOH^* + e^- \rightarrow O^* + OH^-$

(3) $O^* + H_2O + e^- \rightarrow OH^* + OH^-$

(4) $OH^* + e^- \rightarrow OH^-$

Here, * denotes that the oxygen species are anchored to the single-atom metal sites. Considering the equilibrium condition where $H_2O \leftrightarrow H^+ + OH^-$, H_2O in the original equations were replaced by $H^+ + OH^-$, simplifying the equations to:

(1) $O_2 + H^+ + e^- \rightarrow OOH^*$

(2) $OOH^* + H^+ + e^- \rightarrow O^* + H_2O$

(3) $O^* + H^+ + e^- \rightarrow OH^*$

(4) $OH^* + H^+ + e^- \rightarrow H_2O$

Based on Nørskov's analytic model[32], considering the impact of pH value, the free energy change of each step can be expressed as:

$$\Delta G_1 = G_{OOH^*} - G_{O_2} - \left(\frac{1}{2}G_{H_2} - 0.0592 \cdot PH\right) - G_*$$

$$\Delta G_2 = G_{O^*} + G_{H_2O} - G_{OOH^*} - \left(\frac{1}{2}G_{H_2} - 0.0592 \cdot PH\right)$$

$$\Delta G_3 = G_{OH^*} - G_{O^*} - \left(\frac{1}{2}G_{H_2} - 0.0592 \cdot PH\right)$$

$$\Delta G_4 = G_{H_2O} + G_* - G_{OH^*} - \left(\frac{1}{2}G_{H_2} - 0.0592 \cdot PH\right)$$

The RHE model was used to ensure consistency and standardization in assessing the catalyst performance, allowing for meaningful comparisons and a comprehensive understanding of catalytic activity across varying experimental conditions and material systems. By referencing the electrochemical potentials to the RHE scale, where the RHE potential is taken as 0V, the overpotential (η) is calculated by $\eta = \{\max[(\Delta G_1^{PH=13}),\ (\Delta G_2^{PH=13}),\ (\Delta G_3^{PH=13}),\ (\Delta G_4^{PH=13})] +$

$1.23\}/e$.

In addition, the binding free energies of the intermediates OOH*, O*, and OH* were defined by the following equations respectively:

(1) $\Delta G_{OOH^*} = \Delta G[2H_2O(g) + * \rightarrow OOH* + 3/2\,H_2(g)] = G_{OOH^*} + 1.5 \times G_{H_2} - 2 \times G_{H_2O} - G_*$,

(2) $\Delta G_{OH^*} = \Delta G[H_2O(g) + * \rightarrow OH* + 1/2\,H_2(g)] = G_{OH^*} + 0.5 \times G_{H_2} - G_{H_2O} - G_*$

(3) $\Delta G_{O^*} = \Delta G[H_2O(g) + * \rightarrow O* + H_2(g)] = G_{O^*} + G_{H_2} - G_{H_2O} - G_*$

Based on these definitions, the free energy of each step under alkaline environment (pH = 13) can be written as:

$$\Delta G_1^{PH=13} = \Delta G_{OOH^*}^{PH=13} - 1.8416$$

$$\Delta G_2^{PH=13} = \Delta G_{O^*}^{PH=13} - \Delta G_{OOH^*}^{PH=13}$$

$$\Delta G_3^{PH=13} = \Delta G_{OH^*}^{PH=13} - \Delta G_{O^*}^{PH=13}$$

$$\Delta G_4^{PH=13} = -\Delta G_{OH^*}^{PH=13}$$

2.2. DFT Methods

Understanding a system's electronic structure and energetics is critical for determining its catalytic behavior. In the context of quantum chemistry, this information can be attained through the wavefunction derived from the Schrödinger equation. However, directly solving the Schrödinger equation is typically impractical due to its computational complexity, especially for multi-electron systems. To overcome this challenge, Hohenberg and Kohn introduced the concept of electron density. Their first theorem asserts that the ground state energy and wavefunction of a system are uniquely determined by the functional of its electron density. Their second theorem builds on the first, stating that the energy-minimizing electron density corresponds to the full solution of the Schrödinger equation. These theorems provide a more efficient way to calculate the energy and properties from the viewpoint of electron density[33].

For material systems with a collection of atoms, the electron density can be obtained using the self-consistent field (SCF) method. As depicted in Figure 2, starting from an initial guess of the electron density, the SCF method involves iteratively adjusting the electron density based on wavefunctions until a self-consistent electron density is achieved. This approach relies on the Kohn-

Sham equation[33], $\left[-\frac{1}{2}\nabla^2 + V_{ext}(\vec{r}) + V_H(\vec{r}) + V_{XC}(\vec{r})\right]\psi_i(\vec{r}) = \varepsilon_i\psi_i(\vec{r})$, to determine the new electron density, where ψ_i and ε_i represent the wavefunction and energy; $-\frac{1}{2}\nabla^2$, $V_{ext}(\vec{r})$, $V_H(\vec{r})$, and $V_{XC}(\vec{r})$ are the operators of the kinetic energy, the external potential, the Hartree potential, and the exchange-correlation term, respectively.

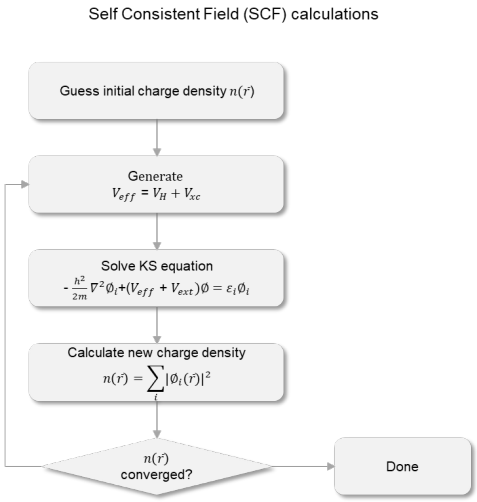

Figure 2. Illustration of self-consistent field (SCF) calculations. The Kohn-Sham (KS) equations are solved iteratively until the electron density converges to a given criterion.

To date, various functionals have been proposed for the exchange-correlation term, each providing varying levels of computational accuracy and efficiency. One of the most widely used functionals is the Perdew-Burke-Ernzerhof (PBE) functional[34]. Renowned for its favorable balance between accuracy and efficiency in modeling condensed materials, the PBE functional was chosen for this study. In addition, periodic boundary conditions (PBC) were utilized to mimic real-world solid-state materials. On this basis, the plane wave basis set was used to express the wavefunction, successfully encapsulating the periodic nature of crystal structures. In addition, the Projector Augmented Wave (PAW) pseudopotential method was used to mimic core electrons, effectively reducing the computational expense[35]. These methodologies empower us to conduct efficient and precise DFT calculations, thus enabling the study of various materials and their properties.

2.3. Performing DFT Calculations using VASP

Herein, we constructed material models based on an earlier work[22] featuring dual M-N_4

moieties, denoted M_1-M_2. We substituted 12 metals, i.e., Mn, Fe, Ni, Co, Cu, Ru, Rh, Pd, Ag, Ir, Pt, and Au, on both the M_1 and M_2 sites, resulting in 144 different configurations. Utilizing the Avogadro software[36], we built the slab, OOH*, O*, and OH* models for one material and then automated the generation of the remaining configurations. As an illustration, Figure 3a displays an example model of M_1-M_2.

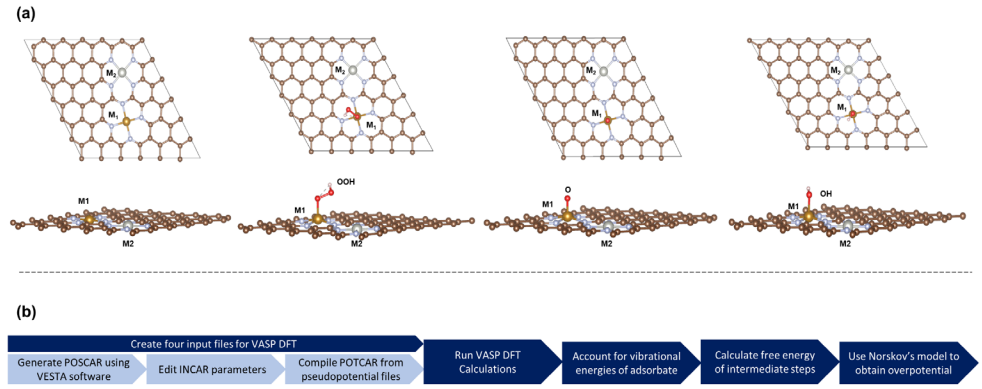

Figure 3. Performing DFT calculations in VASP. (a) Top and side views of Fe-Pd models in order of slab, OOH*, O*, OH*. The gold, silver, brown, red, and white spheres refer to Fe (the M_1 metal), Pd (the M_2 metal), C, O, and H, respectively. (b) Workflow for determining overpotential through DFT calculations utilizing VASP.

The workflow for the DFT calculations in this study is shown in Figure 3b, implemented using the Vienna Ab initio Simulation Package (VASP)[37] for all DFT calculations. We automated the generation of all input files for the 144 SACs, including INCAR (DFT calculation settings), KPOINTS (sampling points in the Brillouin zone), POSCAR (atomic coordinates and lattice parameters), and POTCAR (pseudopotentials for each element), with our custom bash scripts. A kinetic energy cutoff of 450 eV was used for the plane-wave expansion, with convergence criteria for force and energy set at 0.01 eV $Å^{-1}$ and 10^{-5} eV, respectively. Gaussian smearing of 0.1 eV was applied for geometric optimizations, and a 2 × 2 × 1 Gamma-centered mesh k-point grid was used for the SAC models. Strong on-site coulomb interaction involving d-orbital electrons on the transition state metal sites was treated using the GGA+U approach[38]. The U values and initial spin state of each transition metal were adopted from a previous benchmark study[39].

Next, thermodynamic corrections were computed for all the models binding the OOH*, O*, and OH* intermediates using vibrational frequency calculations within the harmonic oscillation approximation. We kept the slab model fixed while relaxing the adsorbates in these calculations, allowing for the efficient computation of thermal corrections associated with respective adsorbates.

These correction values were then added to the DFT total electronic energy values, enabling the computation of free energy profiles for each intermediate step along the reaction pathway. The incorporation of vibrational effects into the overall free energy analysis provided a more comprehensive and accurate assessment of ORR catalytic behavior, as detailed by the Nørskov model mentioned earlier.

2.4. Calculations of Electronic Properties

Our investigation considered both intrinsic and calculated atomic properties pertinent to catalysis. The intrinsic properties, which include electronegativity, atomic radius, ionization energy, and atomic mass, are fundamental characteristics inherent to the metal atoms and are readily accessible from standard reference materials.

We utilized VASPkit[40] and Chargemol[41], computational tools that compute DFT-derived properties, to calculate a set of electronic properties that are often invoked in the context of catalysis. These include the d-band center, HOMO-LUMO gap, partial charge, and spin density. The d-band center represents the average energy level of d orbitals near the Fermi level, providing fundamental insights into the nature of adsorption interactions between the metal and adsorbate species[42]. The energy difference between the highest occupied molecular orbital (HOMO) and the lowest unoccupied molecular orbital (LUMO) is defined as the HOMO-LUMO gap, which is an essential electronic property for metal-adsorbate systems. Partial charge, reflecting the net atomic charge, indicates the unequal sharing of electrons between the metal and adsorbate, thereby offering information about the adsorbate binding strength. Spin density characterizes the distribution of unpaired electrons within the metal-adsorbate system, which helps understand its electronic properties and reactivity. These DFT-calculated properties yield valuable information regarding the electronic structures of the SACs, enabling us to understand their catalytic performance from the viewpoint of electronic structures.

2.5. SISSO Method

The Sure Independence Screening and Sparsity Optimization (SISSO)[43] is an ML algorithm developed to discover accurate and interpretable models that can predict material properties and

behavior. SISSO utilizes the principles of compressed sensing and sparse regression to efficiently handle large feature spaces while maintaining interpretability. It focuses on identifying the most relevant features (or descriptors) that contribute significantly to the target property or behavior being studied. By diminishing the dimensionality of the feature space, SISSO improves model interpretability and reduces computational costs. Notably, the effectiveness of SISSO is not heavily reliant on the availability of big data, a characteristic that sets it apart from many conventional ML algorithms. This is particularly beneficial for material science studies, where access to extensive data sets can be challenging. In this project, we used SISSO to generate effective and interpretable descriptors that can predict the overpotential and adsorbate binding energies of different SACs.

2.6. ETR Method

We utilized the Extra Trees Regressor (ETR)[44] ML algorithm, implemented via the Scikit-learn code[45], for both feature importance analysis and regression tasks. It works by building a suite of decision trees during model training. However, unlike conventional decision trees or random forest algorithms, ETR incorporates two key distinctions: random feature selection and random node splitting. These two methods of randomization allow ETR to create a large variety of uncorrelated decision trees. In the prediction phase, the outputs from all individual trees are averaged to obtain the final regression result. This process of averaging helps negates individual errors, resulting in more robust and accurate predictions. ETR is especially adept at managing noisy, high-dimensional datasets and problems where the relationships between features and the target variable are complex and nonlinear. This makes it a fitting choice for our analysis.

3. Results and Discussion

3.1. Overpotential Heatmaps

Overpotential has been widely applied as a quantitative metric for assessing the performance of ORR, which is determined based on the binding free energies of the OOH*, O*, and OH* intermediates, as detailed in Section 2.1. Figure 4 presents the overpotentials of the 144 catalysts investigated in this work. While it is recognized that there is competition between M_1 and M_2 sites in binding the intermediates, for this simulation study that emphasizes the relationship between

structure and properties, we assume that M_1 is the primary site responsible for intermediate binding. Given this premise, it's not surprising that the M_1 site can exert a more substantial influence on the overpotential of the system compared to M_2. This is evidenced by the distinct patterns that emerged for specific M_1 metals. For example, the SACs with M_1 metals Ir, Rh, and Fe tend to exhibit lower overpotential values for most M_2 species, while catalysts involving Pd, Pt, and Ru generally show higher overpotentials. Nevertheless, we also show that the choice of M_2 is not insignificant - it can impact the catalytic behavior of M_1. This is exemplified by the different performances of Fe-Mn and Fe-Pd. Fe-Mn presents a prohibitive overpotential of 1.985 V, denoting poor performance, whereas Fe-Pd demonstrates the lowest overpotential of 0.980 V, indicating superior performance. This observation underlines the importance of tuning the M_1-M_2 composition for optimal ORR activity.

Figure 4. Overpotential of the 144 SACs. Green values indicate low overpotential (high activity), Orange/Red values indicate high overpotential (low activity). Promising SACs with η <1.18 V are highlighted with red squares.

In our exhaustive study of the 144 M_1-M_2 combinations, we have successfully pinpointed twenty-five SACs (highlighted with red squares in Figure 4) exhibiting lower overpotential than that of the benchmark catalyst, pristine Fe-N_4 (1.18 V)[46]. This discovery is especially notable given the well-established efficacy of Fe-N_4 for ORR. Among the promising catalysts identified, Fe-Pt (with an overpotential of 0.983 V) and Fe-Pd (with an overpotential of 0.980 V) have been validated by previous experimental studies[22, 47].

This congruence between computational prediction and experimental validation not only bolsters the reliability of our computational methodology but also substantiates the promising potential of these catalyst candidates. Furthermore, our exploration unveiled four M_1-M_2 combinations (Fe-Ag, Ag-Cu, Ag-Pd, Ag-Ag) that are not only close to the overpotential performance of Fe-Pd but are significantly less expensive. This crucial discovery opens the tantalizing possibility of achieving efficient ORR catalysis at a significantly reduced cost. These advancements could significantly accelerate the development and commercialization of cost-effective, high-performance ORR catalysts.

3.2. Understanding Adsorption Behaviors

3.2.1. Relationship among ΔG_{OOH*}, ΔG_{O*}, and ΔG_{OH*}

Next, we moved on to delve deeper into the determinants of overpotential, which hinges on the binding free energies of the OOH*, O*, and OH* intermediates. Through a comprehensive assessment of the ΔG_{OOH*}, ΔG_{OH*}, and ΔG_{O*} binding free energies, we successfully delineated the scaling relationships between these quantities, as depicted in [1]-[3]:

$$\Delta G_{OOH*} = 0.492657064 \times \Delta G_{O*} + 1.106113111 \quad \text{[1]}$$

$$\Delta G_{OH*} = 0.556863752 \times \Delta G_{O*} - 0.352882071 \quad \text{[2]}$$

$$\Delta G_{OOH*} = 0.826082575 \times \Delta G_{OH*} + 1.445296836 \quad \text{[3]}$$

The strong linear relationships (Figure 5a-c and Table 1) suggested that the binding energies of these intermediates on a given metal site tend to be intertwined, which presents a dilemma: a catalyst cannot simultaneously optimize the binding energy for all intermediates, leading to a trade-off where the optimization of the binding energy for one intermediate may result in a suboptimal binding energy for another intermediate. While overcoming this limitation is an ongoing research pursuit beyond the scope of this study, the discerned correlations offer a powerful analytical tool: they allow for the estimation of ΔG_{OOH*}, ΔG_{O*}, ΔG_{OH*} binding energies directly from each other, significantly streamlining the analysis of the interplay between binding energies and overpotential.

	Multiple R	Standard Error

ΔG_{OOH*} vs. ΔG_{O*}	0.887	0.306
ΔG_{OH*} vs. ΔG_{O*}	0.903	0.314
ΔG_{OOH*} vs. ΔG_{OH*}	0.916	0.265

Table 1. ΔG_{OOH*} vs ΔG_{O*}, ΔG_{OH*} vs ΔG_{O*}, and ΔG_{OOH*} vs ΔG_{OH*} regression statistics for 144 SACs. Correlation between experimental and predicted values of ΔG_{OOH*}, ΔG_{OH*}, and ΔG_{O*} are quantified using Multiple R and standard error.

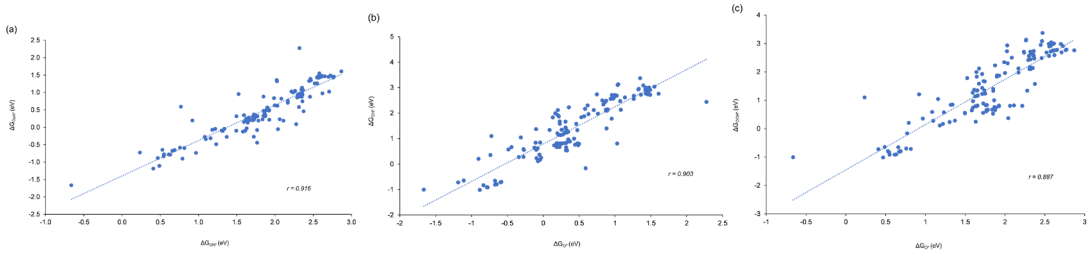

Figure 5. Plots of the relationships between ΔG_{OOH*}, ΔG_{O*}, and ΔG_{OH*} for 144 SACs. (a) ΔG_{OOH*} vs. ΔG_{OH*} (b)ΔG_{OH*} vs. ΔG_{O*}, and (c) ΔG_{OOH*} vs. ΔG_{O*}

3.2.2. Volcano Plots

Using one of the three binding free energies – in this case, ΔG_{OOH*} – as the x-axis and plotting the overpotential as the y-axis, we observed a distinctive volcano-shaped trend, also known as the Sabatier principle[48] shown in Figure 6. The peak of this volcano plot, ranging from approximately 1.59 – 1.78 eV, indicates an optimized region for catalytic activity based on catalysts whose overpotential is affected by ΔG_{OOH*} and has an overpotential ≤1.18 V. Catalysts falling within this optimal range of binding energies demonstrate enhanced activity for ORR, prominently displayed by the five best-performing catalysts: Fe-Pd (η = 0.980 V), Fe-Pt (η = 0.986 V), Fe-Ag (η = 1.008 V), Rh-Mn (η = 1.010 V), and Ir-Ni (η = 1.018 V). The presence of perfect linear correlations on the right wing of the volcano shape in the ΔG_{OOH*} graph (Figure 6) and on the left wing of the volcano shape in the ΔG_{OH*} graph (Appendix 1(a), Section 7.1) signifies that the overpotential-determining step for ORR is primarily contributed either by the first step of *OOH formation or the fourth step of *OH desorption. These findings agree well with previous reports[49,50]. In comparison, the importance of ΔG_{O*} in determining the overpotential is relatively less, as demonstrated in the ΔG_{O*} volcano plot (Appendix 1(b), Section 7.1).

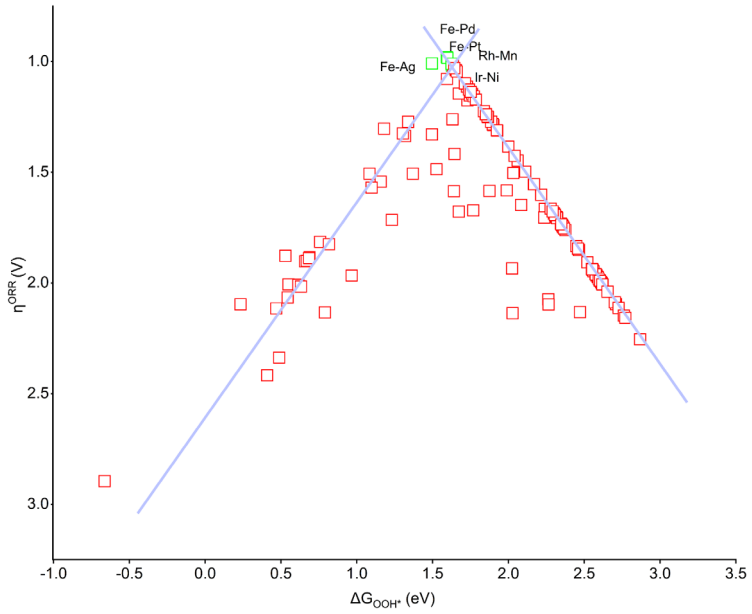

Figure 6. Overpotential as a function of ΔG_{OOH*} for the 144 SACs. The five best-performing M_1-M_2 SACs are highlighted in green and labeled. The peak of the volcano plot underscores the range of optimal binding energies for ΔG_{OOH*} (~1.59-1.78 eV).

Optimizing the ΔG_{OOH*} and/or ΔG_{OH*} values emerge as a compelling strategy to enhance ORR activity. This can be achieved through various strategies, including modifying the coordination environment surrounding the active metal site. For instance, the introduction of ligands, such as an OH group[51] near the active metal site, can alter its electronic structure. This could be achieved by the ligand either donating or withdrawing electrons from the metal center, thereby tuning the metal's electronic properties and enhancing its catalytic activity. Such modifications exert a direct influence on the strength and nature of the interactions between the metal and the adsorbate, thereby shaping the activity of the SACs. This emphasizes the critical significance of precise control over the electronic properties of catalysts, as it empowers the facilitation of efficient and targeted reactions.

3.2.3. Binding Energies of the Metals

Since binding energies play a crucial role in determining the overpotential, we presented them in the form of three distinct heat maps for ΔG_{OOH*} (Figure 7), ΔG_{OH*} (Appendix 2(a) in Section 7.2), and ΔG_{O*} (Appendix 2(b) in Section 7.2). Most of the Ir-M_2, Fe-M_2, and Rh-M_2 combinations exhibit optimal binding energies that are neither too strong nor too weak. These metal pairings enable sufficiently strong interactions to facilitate the reaction while avoiding overly strong binding

that could impede the desorption of reaction intermediates. Conversely, the heat maps indicate that Ru-M_2 combinations generally display relatively weak binding energies with adsorbates. This suggests that the interaction between the Ru and the adsorbates may not be strong enough, which could potentially slow down reaction kinetics. On the other hand, the Pd-M_2, Pt-M_2, and Au-M_2 systems show exceedingly strong binding energies with adsorbates. Such intense interactions may hamper the release of adsorbed intermediates, which could result in decreased reactivity and sluggish reaction rates. These findings emphasize the delicate balancing act required in designing efficient SACs for ORR.

Figure 7. ΔG_{OOH*} for 144 SACs. Optimal binding energies (~1.59 -1.78 eV) are represented in green, overly strong binding energies are marked in red, and excessively weak binding energies are denoted in yellow.

3.3. Synergistic Effect of M_1 and M_2 Sites

To understand how varying M_1-M_2 combinations result in different binding free energies, we directed our attention toward 12 systems with Fe as the M_1 site (Fe-M_2). Previous work by Rosen *et al.*[52] suggested a strong correlation between the binding energies of a molecule on different metal sites and the group number of the metal elements, which is understandable given that the number of outermost electrons tends to increase as one moves across the periodic table. It is therefore reasonable to infer that an increase in M_2's group number may subtly modify M_1's behavior, leading to a gradual change in the binding affinity of intermediates on M_1. In light of this hypothesis, we plotted ΔG_{OOH*} against M_2's group number, as visualized in Figure 8a. Contrary to expectations, a

careful examination of the data from group 7 to group 11 yielded a pattern resembling a volcano plot rather than a clear linear trend. The absence of a linear correlation suggests that different M_2 elements interact uniquely with Fe, beyond simple electron donation or withdrawal mechanisms. Further complicating our understanding, no discernible pattern emerged when comparing the M_2's group number with overpotential (Figure 8b). These observations prompt us to look beyond intrinsic properties and delve into the more complex interactions between the M_1 and M_2 sites. More in-depth analysis, such as molecular orbital hybridization analysis, might offer a more nuanced perspective on the complex interactions between M_1 and M_2, and, in turn, shed more light on how these interactions influence the binding of intermediates on M_1 sites.

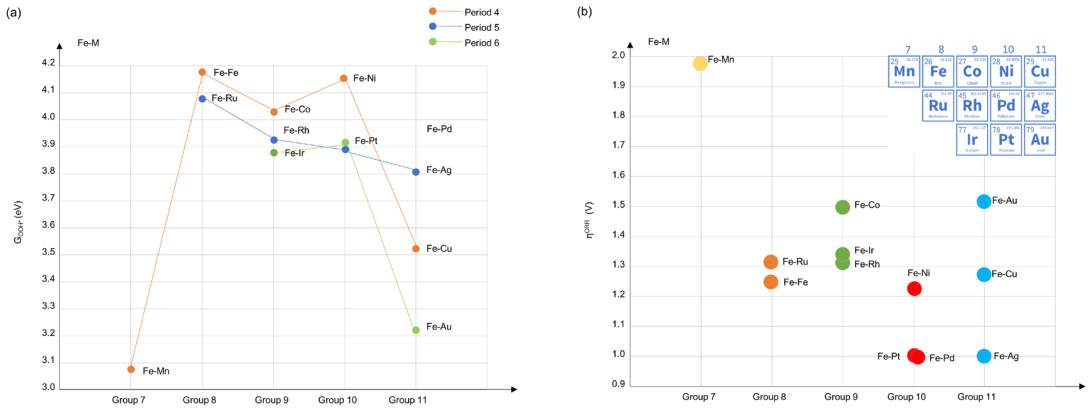

Figure 8. (a) Correlation between the group number of M_2 and ΔG_{OOH^*} for Fe-M_2. (b) Correlation between the group number of M_2 and overpotential for Fe-M_2.

3.4. Case Study: ORR activity of Fe-Pd and Mn-Pd

To further illuminate how binding free energies of the reaction intermediates can influence overpotential, we turned our focus to two extreme cases, Fe-Pd and Mn-Pd, which represent the best and worst-performing SACs, respectively. Their free energy profiles along the 4-electron pathway are shown in Figure 9. The Mn-Pd catalyst displays a significantly higher overpotential of 2.895 V compared to the Fe-Pd catalyst (0.980 V), demonstrating its inferior performance. Under U = 1.23 V, it is apparent that energy increments at each step are more smoothly transitioned in the Fe-Pd catalyst compared to the Mn-Pd catalyst. For the latter, the energy steps on the three binding configurations are significantly more stable than the former, especially for the OH* desorption step. In fact, Mn-Pd showcases the smallest ΔG_{OH^*} value (-1.67 eV) amongst all the 144 systems studied, leading to a prohibitive barrier in the OH* desorption step, leading to a notable decrease in its

activity. Conversely, the Fe-Pd catalyst exhibits an optimal ΔG_{OH*} value (0.35 eV), corresponding to an enhanced ORR activity.

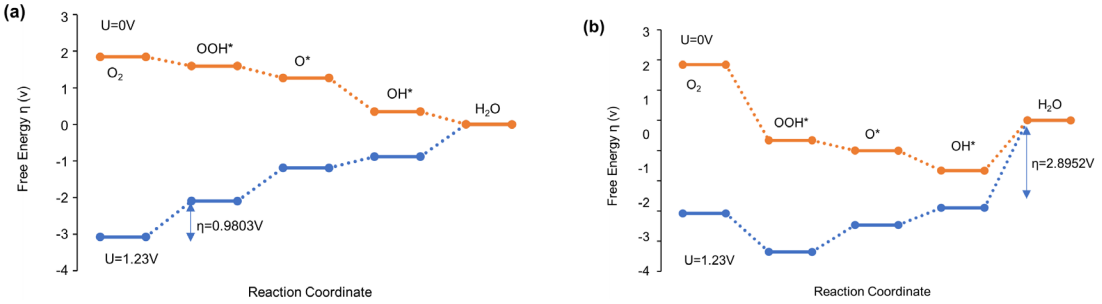

Figure 9. Comparison of the free energy profiles of (a) the best-performing SAC (Fe-Pd) and (b) the worst-performing SAC (Mn-Pd).

To rationalize the huge difference in ΔG_{OH*} between Fe-Pd and Mn-Pd, we computed the projected density of states (PDOS) for the d-orbitals of M_1 sites (Fe and Mn) and p-orbitals of O after OH* binding in both systems. Specifically, we visualized the spatial distribution of molecular orbitals for the electronic states with high density or those close to the Fermi level (E_F). These electronic states are depicted in Figure 10, as they are believed to play a critical role in determining the bonding strength of M_1–OH*. In the case of OH* binding on Fe-Pd (Figure 10a), the frontier orbitals for Fe-O bonding are primarily the π* and σ* antibonding orbitals, leading to relatively weak Fe-OH bonding. In contrast, the orbital energy levels and spatial distributions are remarkably different in the Mn-Pd system (Figure 10b). Near the Fermi level, we observed σ and π bonding orbitals, which considerably strengthens the Mn-O bonding. This leads to a significantly more negative ΔG_{OH*} value of -1.67 eV, which in turn results in a much higher overpotential of 2.895 V (Figure 9). This detailed analysis of molecular orbital hybridization provides further insight into how different M_1-M_2 combinations can dramatically affect the binding free energies and the overall ORR activity.

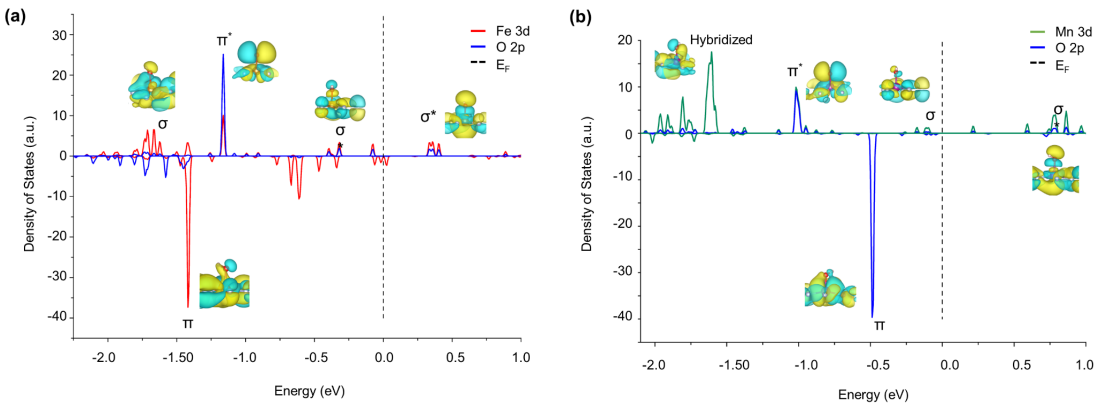

Figure 10. Computed PDOS for (a) Fe-Pd and (b) Mn-Pd, after OH adsorbate binding. The bonding molecular orbitals, denoted as σ and π, correspond to bonding interactions between the d-orbitals of Fe or Mn and the p-orbitals of O. σ* and π* denote the antibonding molecular orbitals arising from interactions between the d orbitals of Fe or Mn and p orbitals of O.

4. Structure-Property Relationships using Machine Learning

While molecular orbital analysis provides qualitative insights into the bonding strength between metal and intermediate reactants, quantitatively predicting overpotential from the readily available intrinsic atomic properties or easy-to-compute electronic properties of single-atom catalysts (SACs) remains a formidable task. This necessitates an in-depth, quantitative grasp of the structure-property relationship, a challenge intensified by the intricate interplay among, in our context, M_1-M_2, and M_1-intermediates. Although DFT is invaluable in analyzing these relationships, its usage is constrained by its time-consuming nature. Consequently, we turn to employing data-driven methodologies like Machine Learning (ML), as a potentially efficient and accurate alternative for overpotential prediction. As illustrated in Figure 11, we considered 16 intrinsic or electronic features, including inherent properties such as electronegativity (χ), atomic radius (r_a), atomic mass (m_a), ionization energy (E_I) of M_1 and M_2 metal atoms (denoted by subscripts $_1$ and $_2$), alongside DFT-derived electronic properties like spin-up and spin-down d-band centers ($\varepsilon_{d\uparrow}$ and $\varepsilon_{d\downarrow}$), partial charge (q), spin density (ρ) on M_1 and M_2, and the HOMO-LUMO gap (E_g) of the M_1-M_2 systems. We employed two types of ML algorithms - the Sure Independence Screening and Sparsifying Operator (SISSO) for feature space dimensional reduction, and Extremely Randomized Trees (ETR), a decision-tree-based approach. These algorithms were trained using 80% of the dataset comprising of 144 SACs and tested on the remaining 20% of the data, as detailed in Sections 2.5 and 2.6.

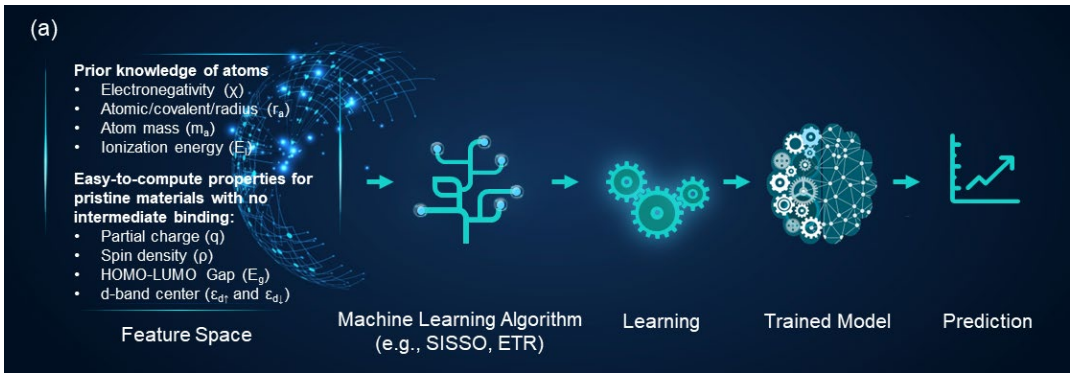

Figure 11. Workflow of the ML process for predicting overpotential from intrinsic atomic properties and DFT-computed electronic properties.

4.1. All-Feature-Trained SISSO Prediction Model (ASPM)

Firstly, we employed the SISSO method to bridge the input features – namely, the intrinsic atomic properties and DFT-computed electronic properties – and the target property (ORR overpotential). For this supervised learning task, SISSO constructed a feature space by mathematically combining each feature using a specified set of operators, represented as $\hat{H} \equiv \{I, +, -, \times, \div, \log, \exp, \exp_-, -1, 2, 3, 6, \sqrt{}, |\ |, \sin, \cos, scd\}$[43]. Only physically meaningful combinations, i.e., those with identical units, were retained. Sure-independence screening (SIS) was then used to rank and select descriptors based on their correlations with the target property. The sparsifying operator (SO) method was subsequently adopted to further promote descriptor space sparsity, effectively reducing the feature space dimensionality. This procedure generated a set of feature-operator combinations, which serve as descriptors for connecting features and overpotential.

The equation derived from these descriptors (eq. [4]) is as follows:

$$\eta_{SISSO-Predicted} = -0.365 \times \left[\cos\left(\frac{m_{a1}}{\chi_1}\right)\right] - 1.408 \times \left|scd(E_{g\downarrow}) - \sin(q_1)\right| + 1.331 \times \left[\frac{\chi_1 - \chi_2}{\left(\frac{\varepsilon_{d\downarrow}}{E_{g\downarrow}}\right)}\right] + 1.915 \qquad [4]$$

This equation demonstrated statistically significant accuracy in predicting overpotential, with a significant correlation coefficient (r) of 0.852 for the training datasets (Figure 12a). The Root Mean Square Error (RMSE) value of 0.193 V falls within the computational error of DFT, signifying a strong agreement between SISSO-predicted and DFT-computed values. When predicting for the testing datasets, the performance slightly deteriorated (r = 0.747, RMSE = 0.271 V, Figure 12b), hinting at possible overfitting. This may be attributed to including too many unrelated or interrelated features or a lack of sufficient datasets (in this instance, 144). Despite comprehensive attempts to

improve the prediction accuracy of the SISSO model — such as incorporating more informative features (refer to Appendix 3 in Section 7.3), refining the selection of input features[53] (detailed in Section 4.2), and exploring alternative approaches to overpotential prediction (Appendix 4 in Section 7.4) — we failed to achieve significant improvement. This outcome underscores the complexity of the problem and invites further investigation into novel predictive methodologies. Nevertheless, the results emphasize the relative precision of the descriptors generated by SISSO in capturing the quantitative relationship between features and overpotential.

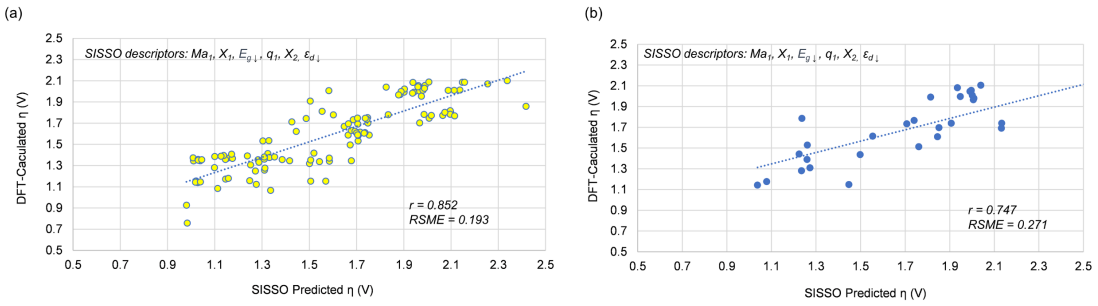

Figure 12. Comparison between DFT-computed and SISSO-predicted overpotential using all the 16 features (ASPM) for the (a) training and (b) testing datasets.

More interestingly, upon closer inspection, eq. 4 is mainly comprised of M_1 properties, which is expected since M_1 is the site directly bonding with the reaction intermediates and should, therefore, govern the overpotential. The equation includes three key terms. The first term, $\cos(\frac{m_{a1}}{\chi_1})$, relates to M_1's intrinsic properties, such as mass and electronegativity, which naturally influence the catalytic properties of the M_1 site. The second term, $scd(E_{g\downarrow}) - \sin(q_1)$, represents the partial charge on the M_1 site and the M_1-M_2 material's electronic bandgap, both crucial to catalytic activity. These parameters are influenced implicitly by the properties of M_2, hence indirectly incorporating M_2's chemical information. The third term's numerator, $\chi_1 - \chi_2$, is the electronegativity difference between M_1 and M_2, conveying the information of charge transfer between the metal sites, while the denominator, $\frac{\varepsilon_{d\downarrow}}{E_{g\downarrow}}$, carries molecular orbital information. These terms validate our hypothesis that the catalytic properties of M_1-M_2 are impacted by the interactions between the M_1-N_4 and M_2-N_4 sites. This happens even though the M_1-N_4 and M_2-N_4 sites are not directly connected, and extends beyond simple electron donation or withdrawal mechanisms. Importantly, these complex interactions can be quantified using the SISSO-generated descriptors.

4.2. Refined-Feature-Trained SISSO Prediction Model (RSPM)

To mitigate the overfitting resulting from the small data problem, it is potentially beneficial to evaluate the relevance and significance of each feature. Less important features may introduce noise or bias, potentially leading to inaccurate predictions. Consequently, we refined the initial sixteen features used for training the model.

The importance analysis for each feature was performed using the ETR algorithm, a commonly utilized decision tree-based ML method. This allowed us to assess the relative importance of each feature in determining the overpotential (Table 2). The refined features were selected based on a mean importance cutoff of 0.05, ensuring only the most informative and impactful features were retained. The refined feature set included the ionization energy of M_1 (E_{I1}), d-band centers ($\varepsilon_{d\uparrow}$ and $\varepsilon_{d\downarrow}$), spin density of M_1 (ρ_1), partial charge of M_1 (q_1), electronegativity of M_1 (χ_1), and atomic radius of M_1 (r_{a1}). Using these refined features, we formulated another SISSO-generated equation as follows:

$$\eta_{SISSO-Predicted} = 0.304 \times [\cos(\varepsilon_{d\uparrow} + \varepsilon_{d\downarrow})] - 0.363 \times \left[\frac{scd(\varepsilon_{d\uparrow})}{\cos(E_{I1})}\right] + 0.000575 \times \left[\frac{{\chi_1}^6}{\sin(r_{a1})}\right] + 1.696 \quad [5]$$

Features	Feature Mean Importance
M_1-Partial-charge (q_1)	0.300
M_1- Ionization (E_{I1})	0.224
M_1- Electronegativity (χ_1)	0.125
M_1-Spin-density (ρ_1)	0.080
Band-Up ($\varepsilon_{d\uparrow}$)	0.062
M_1- Radius (r_{a1})	0.061
Band-Down ($\varepsilon_{d\downarrow}$)	0.053
M_1-Mass (m_{a1})	0.038
Gap Down ($E_{g\downarrow}$)	0.016
M_2-Electronegativity (χ_2)	0.014
M_2-Radius (r_{a2})	0.012
M_2-Ionization (E_{I2})	0.011
M_2-Mass (m_{a2})	0.011

Gap Up ($E_{g\uparrow}$)	0.011
M_2- Partial-charge (q_2)	0.006
M_2-Spin-density (ρ_2)	0.002

Table 2. Evaluation of the mean importance for sixteen input features using the ETR Algorithm. Features with mean importance greater than 0.05 (bolded) were selected for the RSPM.

The refined-feature-trained SISSO prediction model (RSPM) showed a correlation coefficient of r = 0.822 and an RMSE value of 0.209 (Figure 13a). Although its performance is slightly lower than the model trained with ASPM (refer to Section 4.1), the RSPM provides a comparable outcome while requiring fewer computed features in the prediction equations, specifically the HOMO-LUMO gap and partial charge. For the testing set, the RSPM demonstrated a correlation coefficient (r) of 0.736 and an RMSE value of 0.273 for the testing data (Figure 13b), close to the prediction performance of the ASPM model in Section 4.1.

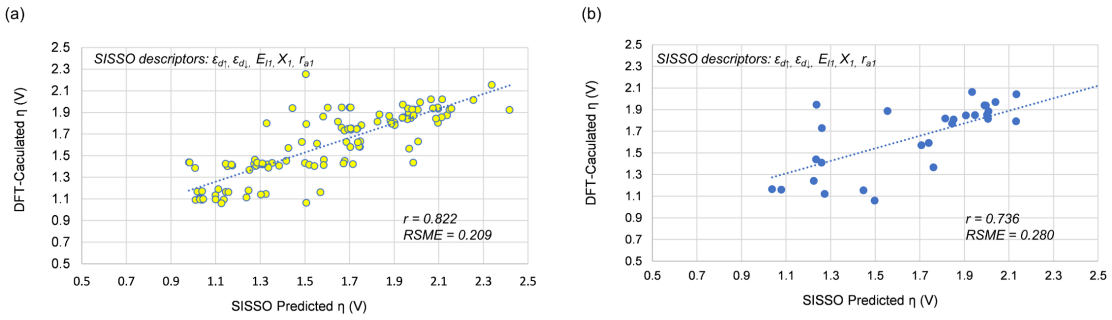

Figure 13. Comparison between DFT-computed and SISSO-predicted overpotential using refined features (RSPM) for the (a) training and (b) testing datasets.

4.3. Extra Tree Regressor Prediction Model (ETR)

Subsequently, we utilized the ETR algorithm to predict overpotential based on the 16 features. A significant disparity was noted when comparing the performance of the ETR-based model on the training data (80%) and the testing data (20%). The model performed perfectly on the training data, showing an ideal correlation coefficient of *r* = 1.000 and an RMSE value of 0.000 V (Figure 14a). However, its performance declined when applied to the testing data, producing a correlation coefficient of r = 0.856 and an RMSE value of 0.195 V (Figure 14b). This divergence is reflective of overfitting, a classic challenge encountered with smaller datasets, where the model could excessively adapt to the training data at the expense of generalization. However, even with this

noted dip in performance, our ETR model outperformed the SISSO model on the testing dataset, reinforcing the ETR's competitive edge in overpotential prediction. Most importantly, we see a clear path for the future advancement of our ETR model. We can, therefore, expect an improvement in the model prediction power with an increase in the size of the training datasets. Figure 14c clearly depicts that as the training dataset size grows, there's a marked increase in prediction accuracy. This suggests that expanding the training data could be a fruitful direction for the continued refinement and evolution of our model.

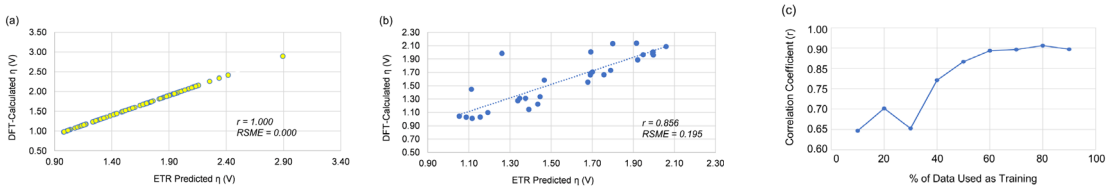

Figure 14. Comparison between DFT-computed and ETR-predicted overpotential using all the 16 features for the (a) training and (b) testing datasets. (c) Illustration of the incremental improvement in the predictive ability of the ETR model with increasing size of training datasets.

4.4. Performance Summary

Table 3 outlines the performance of the above-mentioned three ML models – the ASPM and RSPM SISSO models, and the ETR model. These models exhibit impressive performance, demonstrating the utility and effectiveness of ML in material design. Particularly, we applied these three models to predict promising M_1-M_2 combinations, using pristine Fe-N_4 (η = 1.18V) as a benchmark. As detailed in Table 4 and Table 5, the ASPM, RSPM SISSO models, and the ETR model predicted 17, 26, and 24 promising materials, respectively. DFT validations of these predictions highlighted 11, 17, and 24 successful matches, translating to success rates of 65%, 65%, and a stellar 100%, respectively.

In addition, we identified the top twenty-five catalysts via DFT calculations (Figure 4), each surpassing the benchmark of pristine Fe-N_4. We aimed to assess how many of these high-performing materials could be accurately predicted by our ML models. As detailed in Table 5, the results were fairly encouraging: the ASPM successfully predicted 44% (11 out of 25), while the RSPM identified a commendable 68% (17 out of 25), demonstrating the robust predictive capabilities of these models. In comparison to these SISSO models, the ETR model achieved a success rate of 96% (24 out of 25), although potential overfitting in the training dataset for the ETR model cannot be overlooked.

However, its promising performance for the testing set still strongly supports its capacity for the rapid identification of high-potential materials.

These findings affirm that while ML models may not be flawless, they can significantly alleviate the burden of time-consuming DFT computations and expensive experimental procedures. The enhanced performance of the RSPM model in predicting top catalysts underscores the potential of refining such models to improve prediction accuracy, thus driving the field of materials science toward more efficient and precise discovery and development.

Models	Coefficient (r)	r^2	RMSE	MAE
ASPM (Training)	0.852	0.726	0.193	0.558
ASPM (Testing)	0.747	0.558	0.271	0.994
RSPM (Training)	0.822	0.676	0.209	0.751
RSPM (Testing)	0.736	0.542	0.280	0.778
ETR (Training)	1.000	1.000	0.000	0.000
ETR (Testing)	0.856	0.733	0.195	0.724

Table 3. ASPM (training and testing), RSPM (training and testing), and ETR (training and testing) model prediction statistics. Performance quantified by r, r^2, RMSE, MAE.

M_1-M_2	Overpotential	ASPM Predicted	RSPM Predicted	ETR Predicted
Fe-Pd	0.980	0.927		0.980
Fe-Pt	0.983	0.758		0.983
Fe-Ag	1.008			1.008
Rh-Mn	1.010		1.091	1.116*
Ir-Ni	1.018		1.168	1.018
Ir-Pt	1.020	1.155	1.166	1.020
Ir-Fe	1.028	1.139	1.165	1.028
Rh-Pt	1.029		1.104	1.087*
Rh-Ni	1.030		1.095	1.155*
Ir-Mn	1.037	1.143	1.165	1.037
Rh-Fe	1.038		1.092	1.038
Ir-Pd	1.039	1.147	1.171	1.039

Rh-Pd	1.045		1.099	1.053*
Ir-Ru	1.079	1.177	1.161	1.079
Rh-Ag	1.099		1.133	1.192*
Rh-Ru	1.100		1.096	1.100
Ir-Ag	1.113	1.084		1.113
Rh-Ir	1.126		1.061	1.126
Rh-Rh	1.137		1.095	1.137
Ag-Pd	1.145			1.392*
Ir-Ir	1.146	1.172	1.166	1.146
Ag-Cu	1.153			1.153
Ir-Rh	1.157	1.179	1.164	1.157
Mn-Rh	1.171			1.171
Ag-Ag	1.175			1.175
Rh-Au	1.238		1.114	
Ir-Au	1.248	1.158	1.179	
Rh-Cu	1.273		1.121	
Fe-Cu	1.276	1.123		
Co-Au	1.303		1.141	
Co-Rh	1.325		1.145	
Co-Co	1.336	1.066		
Ir-Cu	1.448	1.148	1.154	
Co-Ru	1.498		1.06	
Rh-Co	1.505		1.064	
Co-Cu	1.506	1.153		
Ir-Co	1.57	1.153	1.162	

Table 4. ASPM, RSPM, and ETR predictability of the top twenty-five DFT-computed catalysts. Red values indicate a false prediction of material. * Indicates the testing result from ETR.

	Total # of good catalysts predicted (A)	# of good catalysts confirmed by DFT (B)	% of good catalysts confirmed by DFT (C) = (B)/(A)	% of good predicted vs. 25 good catalysts by DFT (F) = (B)/25
ASPM	17	11	65%	44%
RSPM	26	17	65%	68%
ETR	24	24	100%	96%

Table 5. Comparison of the performances of ASPM, RSPM, and ETR in predicting the top twenty-five DFT-computed catalysts.

5. Conclusion

In this work, we applied a synergistic approach of DFT calculations and ML techniques to explore the ORR performance of 144 SACs. We discovered 25 materials that outperformed the pristine Fe-N_4 benchmark, offering superior catalytic activity. Of particular interest, the Fe-Pd, Fe-Pt, and Fe-Ag catalysts emerged as top performers, delivering impressive overpotentials of 0.980 V, 0.983 V, and 1.008 V respectively, under alkaline conditions (pH = 13). This surpasses the performance of most, if not all, previously reported materials, and sets a promising precedent for the field. Especially noteworthy is the economic feasibility of Fe-Ag, given the abundant availability and cost-effectiveness of both iron (Fe) and silver (Ag). Additional catalysts, such as Ag-Cu, Ag-Pd, and Ag-Ag, showed promising performance alongside economic efficiency.

Our comprehensive analysis of adsorbate binding energies helped us pinpoint an optimal range for ΔG_{OOH*} (~1.59-1.78 eV) and ΔG_{OH*} (~0.15-0.37 eV). This range correlates with high catalytic performance, thereby providing valuable insight for future experimental optimization. Therefore, the potential to enhance overall catalyst performance through structural modifications that optimize active site binding energies is notable. To further delve into these insights, we conducted an orbital analysis on our best performing catalyst (Fe-Pd) and the least effective one (Mn-Pd). The analysis highlighted that the ideal binding strength of reaction intermediates arises from a balanced interaction between the bonding and anti-bonding orbitals in the frontier orbitals.

We trained ML models using a suite of atomic and electronic properties pertaining to the single-atom metal sites as input features to predict the overpotential of the SACs. Impressively, these models exhibited significant predictive prowess, with one of the SISSO models and the ETR model successfully reproducing 68% and 96% of the top-performing SACs, respectively. These

results highlighted the potential of ML as a tool to reduce the need for costly DFT computations and to streamline experimental trial-and-error processes.

Collectively, our research lays a firm foundation for the intelligent design and discovery of SACs. We have not only illuminated the possibilities for a more sustainable and eco-friendly future but also set a foundation for further exploration of ORR performance and the application of ML in material design. This opens up the possibility for the development of highly efficient, cost-effective catalysts that could revolutionize energy conversion and storage applications, extending far beyond catalysis.

6. References

1. Ge, X.; Sumboja, A.; Wuu, D.; An, T.; Li, B.; Goh, F. W. T.; Hor, T. S. A.; Zong, Y.; Liu, Z. Oxygen Reduction in Alkaline Media: From Mechanisms to Recent Advances of Catalysts. *ACS Catalysis* **2015**, *5* (8), 4643–4667. https://doi.org/10.1021/acscatal.5b00524.
2. Katsounaros, I.; Cherevko, S.; Zeradjanin, A. R.; Mayrhofer, K. J. J. Oxygen Electrochemistry as a Cornerstone for Sustainable Energy Conversion. *Angewandte Chemie International Edition* **2013**, *53* (1), 102–121. https://doi.org/10.1002/anie.201306588.
3. Zaman, S.; Huang, L.; Abdoulkader Ibro Douka; Yang, H.; You, B.; Bao Yu Xia. Oxygen Reduction Electrocatalysts toward Practical Fuel Cells: Progress and Perspectives. *Angewandte Chemie International Edition* **2021**, *60* (33), 17832–17852. https://doi.org/10.1002/anie.202016977.
4. Liu, M.; Xiao, X.; Li, Q.; Luo, L.; Ding, M.; Zhang, B.; Li, Y.; Zou, J.; Jiang, B. Recent Progress of Electrocatalysts for Oxygen Reduction in Fuel Cells. *Journal of Colloid and Interface Science* **2022**, *607*, 791–815. https://doi.org/10.1016/j.jcis.2021.09.008.
5. Ma, R.; Lin, G.; Zhou, Y.; Liu, Q.; Zhang, T.; Shan, G.; Yang, M.; Wang, J. A Review of Oxygen Reduction Mechanisms for Metal-Free Carbon-Based Electrocatalysts. *npj Computational Materials* **2019**, *5* (1). https://doi.org/10.1038/s41524-019-0210-3.
6. Ma, Z.; Cano, Z. P.; Yu, A.; Chen, Z.; Jiang, G.; Fu, X.; Yang, L.; Wu, T.; Bai, Z.; Lu, J. Enhancing Oxygen Reduction Activity of Pt-Based Electrocatalysts: From Theoretical Mechanisms to Practical Methods. *Angewandte Chemie* **2020**, *132* (42), 18490–18504. https://doi.org/10.1002/ange.202003654.
7. Lu, Y.; Li, X.; Compton, R. G. Oxygen Reduction Reaction at Single Entity Multiwalled Carbon Nanotubes. *The Journal of Physical Chemistry Letters* **2022**, *13* (16), 3748–3753. https://doi.org/10.1021/acs.jpclett.2c00871.
8. Wu, Z.-P.; Caracciolo, D. T.; Maswadeh, Y.; Wen, J.; Kong, Z.; Shan, S.; Vargas, J. A.; Yan, S.; Hopkins, E.; Park, K.; Sharma, A.; Ren, Y.; Petkov, V.; Wang, L.; Zhong, C.-J. Alloying–Realloying Enabled High Durability for Pt–Pd-3d-Transition Metal Nanoparticle

Fuel Cell Catalysts. *Nature Communications* **2021**, *12* (1), 859. https://doi.org/10.1038/s41467-021-21017-6.

9. Li, L.; Chang, X.; Lin, X.; Zhao, Z.-J.; Gong, J. Theoretical Insights into Single-Atom Catalysts. *Chemical Society Reviews* **2020**, *49* (22), 8156–8178. https://doi.org/10.1039/d0cs00795a.
10. Guo, J.; Liu, H.; Li, D.; Wang, J.; Djitcheu, X.; He, D.; Zhang, Q. A Minireview on the Synthesis of Single Atom Catalysts. *RSC Advances* **2022**, *12* (15), 9373–9394. https://doi.org/10.1039/D2RA00657J.
11. Wang, A.; Li, J.; Zhang, T. Heterogeneous Single-Atom Catalysis. *Nature Reviews Chemistry* **2018**, *2* (6), 65–81. https://doi.org/10.1038/s41570-018-0010-1.
12. Chen, Y.; Ji, S.; Zhao, S.; Chen, W.; Dong, J.; Cheong, W.-C.; Shen, R.; Wen, X.; Zheng, L.; Rykov, A. I.; Cai, S.; Tang, H.; Zhuang, Z.; Chen, C.; Peng, Q.; Wang, D.; Li, Y. Enhanced Oxygen Reduction with Single-Atomic-Site Iron Catalysts for a Zinc-Air Battery and Hydrogen-Air Fuel Cell. *Nature Communications* **2018**, *9* (1). https://doi.org/10.1038/s41467-018-07850-2.
13. Liu, J.; Jiao, M.; Lu, L.; Barkholtz, H. M.; Li, Y.; Wang, Y.; Jiang, L.; Wang, Y.; Liu, D.-J.; Zhuang, L.; Ma, C.; Zeng, J.; Zhang, B.; Dang Sheng Su; Zou, M.-H.; Xing, W.; Xu, W.; Jiang, Z.; Sun, G. High Performance Platinum Single Atom Electrocatalyst for Oxygen Reduction Reaction. *Nature Communications* **2017**, *8* (1). https://doi.org/10.1038/ncomms15938.
14. Rao, P.; Wu, D.; Wang, T.-J.; Li, J.; Deng, P.; Chen, Q.; Shen, Y.; Chen, Y.; Tian, X. Single Atomic Cobalt Electrocatalyst for Efficient Oxygen Reduction Reaction. *eScience* **2022**, *2* (4), 399–404. https://doi.org/10.1016/j.esci.2022.05.004.
15. Li, J.; Chen, C.; Xu, L.; Zhang, Y.; Wei, W.; Zhao, E.; Wu, Y.; Chen, C. Challenges and Perspectives of Single-Atom-Based Catalysts for Electrochemical Reactions. *Journal of the American Chemical Society* **2023**, *3* (3), 736–755. https://doi.org/10.1021/jacsau.3c00001.

16. Jain, A.; Shin, Y.; Persson, K. A. Computational Predictions of Energy Materials Using Density Functional Theory. *Nature Reviews Materials* **2016**, *1* (1), 1–13. https://doi.org/10.1038/natrevmats.2015.4.
17. Fu, C.; Liu, C.; Li, T.; Zhang, X.; Wang, F.; Yang, J.; Jiang, Y.; Cui, P.; Li, H. DFT Calculations: A Powerful Tool for Better Understanding of Electrocatalytic Oxygen Reduction Reactions on Pt-Based Metallic Catalysts. *Computational Materials Science* **2019**, *170*, 109202. https://doi.org/10.1016/j.commatsci.2019.109202.
18. Makkar, P.; Ghosh, N. N. A Review on the Use of DFT for the Prediction of the Properties of Nanomaterials. *RSC Advances* **2021**, *11* (45), 27897–27924. https://doi.org/10.1039/d1ra04876g.
19. Florian Kraushofer; Parkinson, G. S. Single-Atom Catalysis: Insights from Model Systems. *Chemical Reviews* **2022**, *122* (18), 14911–14939. https://doi.org/10.1021/acs.chemrev.2c00259.
20. Deng, C.; He, R.; Shen, W.; Li, M.; Zhang, T. A Single-Atom Catalyst of Cobalt Supported on a Defective Two-Dimensional Boron Nitride Material as a Promising Electrocatalyst for the Oxygen Reduction Reaction: A DFT Study. *Physical Chemistry Chemical Physics* **2019**, *21* (13), 6900–6907. https://doi.org/10.1039/c9cp00452a.
21. Yang, S.; Yu, Y.; Dou, M.; Zhang, Z.; Dai, L.; Wang, F. Two-Dimensional Conjugated Aromatic Networks as High-Site-Density and Single-Atom Electrocatalysts for the Oxygen Reduction Reaction. *Angewandte Chemie International Edition* **2019**, *58* (41), 14724–14730. https://doi.org/10.1002/anie.201908023.
22. Han, A.; Wang, X.; Tang, K.; Zhang, Z.; Ye, C.; Kong, K.; Hu, H.; Zheng, L.; Jiang, P.; Zhao, C.; Zhang, Q.; Wang, D.; Li, Y. An Adjacent Atomic Platinum Site Enables Single-Atom Iron with High Oxygen Reduction Reaction Performance. *Angewandte Chemie International Edition* **2021**, *60* (35), 19262–19271. https://doi.org/10.1002/anie.202105186.
23. Choudhary, K.; DeCost, B.; Chen, C.; Jain, A.; Tavazza, F.; Cohn, R.; Park, C. W.; Choudhary, A.; Agrawal, A.; Billinge, S. J. L.; Holm, E.; Ong, S. P.; Wolverton, C. Recent Advances and Applications of Deep Learning Methods in Materials Science. *npj Computational Materials* **2022**, *8* (1). https://doi.org/10.1038/s41524-022-00734-6.

24. Xu, P.; Ji, X.; Li, M.; Lu, W. Small Data Machine Learning in Materials Science. *npj Computational Materials* **2023**, *9* (1). https://doi.org/10.1038/s41524-023-01000-z.

25. Wang, S.; Jiang, J. Interpretable Catalysis Models Using Machine Learning with Spectroscopic Descriptors. *ACS Catalysis* **2023**, *13* (11), 7428–7436. https://doi.org/10.1021/acscatal.3c00611.

26. Zhang, X.; Liu, J.; Li, R.; Jian, X.; Gao, X.; Lu, Z.; Yue, X. Machine Learning Screening of High-Performance Single-Atom Electrocatalysts for Two-Electron Oxygen Reduction Reaction. *Journal of Colloid and Interface Science* **2023**, *645*, 956–963. https://doi.org/10.1016/j.jcis.2023.05.011.

27. Ghanekar, P. G.; Deshpande, S.; Greeley, J. Adsorbate Chemical Environment-Based Machine Learning Framework for Heterogeneous Catalysis. *Nature Communications* **2022**, *13* (1). https://doi.org/10.1038/s41467-022-33256-2.

28. Xie, X.; Peng, L.; Yang, H.; Waterhouse, G. I. N.; Shang, L.; Zhang, T. MIL-101-Derived Mesoporous Carbon Supporting Highly Exposed Fe Single-Atom Sites as Efficient Oxygen Reduction Reaction Catalysts. *Advanced Materials* **2021**, *33* (23), 2101038. https://doi.org/10.1002/adma.202101038.

29. Shang, H.; Zhou, X.; Dong, J.; Li, A.; Zhao, X.; Liu, Q.; Lin, Y.; Pei, J.; Li, Z.; Jiang, Z.; Zhou, D.; Zheng, L.; Wang, Y.; Zhou, J.; Yang, Z.; Cao, R.; Sarangi, R.; Sun, T.; Yang, X.; Zheng, X. Engineering Unsymmetrically Coordinated Cu-S1N3 Single Atom Sites with Enhanced Oxygen Reduction Activity. *Nature Communications* **2020**, *11* (1). https://doi.org/10.1038/s41467-020-16848-8.

30. Xiao, M.; Zhu, J.; Li, G.; Li, N.; Li, S.; Cano, Z. P.; Ma, L.; Cui, P.; Xu, P.; Jiang, G.; Jin, H.; Wang, S.; Wu, T.; Lu, J.; Yu, A.; Su, D.; Chen, Z. A Single-Atom Iridium Heterogeneous Catalyst in Oxygen Reduction Reaction. *Angewandte Chemie International Edition* **2019**, *58* (28), 9640–9645. https://doi.org/10.1002/anie.201905241.

31. Jeong, H.; Shin, D.; Kim, B.; Bae, J.; Shin, S.; Choe, C.; Han, J. W.; Lee, H. Controlling the Oxidation State of Pt Single Atoms for Maximizing Catalytic Activity. *Angewandte Chemie* **2020**, *132* (46), 20872–20877. https://doi.org/10.1002/ange.202009776.

32. Nørskov, J. K.; Rossmeisl, J.; Logadottir, A.; Lindqvist, L.; Kitchin, J. R.; Bligaard, T.; Jónsson, H. Origin of the Overpotential for Oxygen Reduction at a Fuel-Cell Cathode. *The Journal of Physical Chemistry B* **2004**, *108* (46), 17886–17892. https://doi.org/10.1021/jp047349j.
33. Sholl, D. S.; Steckel, J. A. *Density Functional Theory : A Practical Introduction*; Wiley: Hoboken, N.J., 2009.
34. Perdew, J. P.; Burke, K.; Ernzerhof, M. Generalized Gradient Approximation Made Simple. *Physical Review Letters* **1996**, *77* (18), 3865–3868. https://doi.org/10.1103/physrevlett.77.3865.
35. Blöchl, P. E. Projector Augmented-Wave Method. *Physical Review B* **1994**, *50* (24), 17953–17979. https://doi.org/10.1103/physrevb.50.17953.
36. Hanwell, M. D.; Curtis, D. E.; Lonie, D. C.; Vandermeersch, T.; Zurek, E.; Hutchison, G. R. Avogadro: An Advanced Semantic Chemical Editor, Visualization, and Analysis Platform. *Journal of Cheminformatics* **2012**, *4* (1). https://doi.org/10.1186/1758-2946-4-17.
37. Kresse, G.; Furthmüller, J. Efficient Iterative Schemes Forab Initiototal-Energy Calculations Using a Plane-Wave Basis Set. *Physical Review B* **1996**, *54* (16), 11169–11186. https://doi.org/10.1103/physrevb.54.11169.
38. Himmetoglu, B.; Floris, A.; de Gironcoli, S.; Cococcioni, M. Hubbard-Corrected DFT Energy Functionals: The LDA+U Description of Correlated Systems. *International Journal of Quantum Chemistry* **2013**, *114* (1), 14–49. https://doi.org/10.1002/qua.24521.
39. Xu, H.; Cheng, D.; Cao, D.; Zeng, X. C. A Universal Principle for a Rational Design of Single-Atom Electrocatalysts. *Nature Catalysis* **2018**, *1* (5), 339–348. https://doi.org/10.1038/s41929-018-0063-z.
40. Wang, V.; Xu, N.; Liu, J.-C.; Tang, G.; Geng, W.-T. VASPKIT: A User-Friendly Interface Facilitating High-Throughput Computing and Analysis Using VASP Code. *Computer Physics Communications* **2021**, *267*, 108033. https://doi.org/10.1016/j.cpc.2021.108033.
41. Limas, N. G.; Manz, T. A. Introducing DDEC6 Atomic Population Analysis: Part 4. Efficient Parallel Computation of Net Atomic Charges, Atomic Spin Moments, Bond

Orders, and More. *RSC Advances* **2018**, *8* (5), 2678–2707. https://doi.org/10.1039/c7ra11829e.

42. Hammer, B.; Norskov, J. K. Why Gold Is the Noblest of All the Metals. *Nature* **1995**, *376* (6537), 238–240. https://doi.org/10.1038/376238a0.
43. Ouyang, R.; Curtarolo, S.; Ahmetcik, E.; Scheffler, M.; Ghiringhelli, L. M. SISSO: A Compressed-Sensing Method for Identifying the Best Low-Dimensional Descriptor in an Immensity of Offered Candidates. *Physical Review Materials* **2018**, *2* (8). https://doi.org/10.1103/physrevmaterials.2.083802.
44. Geurts, P.; Ernst, D.; Wehenkel, L. Extremely Randomized Trees. *Machine Learning* **2006**, *63* (1), 3–42. https://doi.org/10.1007/s10994-006-6226-1.
45. Pedregosa, F.; Varoquaux, G.; Gramfort, A.; Michel, V.; Thirion, B.; Grisel, O.; Blondel, M.; Prettenhofer, P.; Weiss, R.; Dubourg, V.; Vanderplas, J.; Passos, A.; Cournapeau, D.; Brucher, M.; Perrot, M.; Duchesnay, É. Scikit-Learn: Machine Learning in Python. *Journal of Machine Learning Research* **2011**, *12* (85), 2825–2830.
46. Chen, Y.; Ji, S.; Wang, Y.; Dong, J.; Chen, W.; Li, Z.; Shen, R.; Zheng, L.; Zhuang, Z.; Wang, D.; Li, Y. Isolated Single Iron Atoms Anchored on N-Doped Porous Carbon as an Efficient Electrocatalyst for the Oxygen Reduction Reaction. *Angewandte Chemie International Edition* **2017**, *56* (24), 6937–6941. https://doi.org/10.1002/anie.201702473.
47. Li, Q.; Luo, L.; Xu, C.; Song, S.; Wang, Y.; Zhang, L.; Tang, Y.; Texter, J. Palladium Enhanced Iron Active Site – an Efficient Dual-Atom Catalyst for Oxygen Electroreduction. *Small* **2023**. https://doi.org/10.1002/smll.202303321.
48. Medford, A. J.; Vojvodic, A.; Hummelshøj, J. S.; Voss, J.; Abild-Pedersen, F.; Studt, F.; Bligaard, T.; Nilsson, A.; Nørskov, J. K. From the Sabatier Principle to a Predictive Theory of Transition-Metal Heterogeneous Catalysis. *Journal of Catalysis* **2015**, *328*, 36–42. https://doi.org/10.1016/j.jcat.2014.12.033.
49. Yang, L.; Zhang, Y.; Huang, Y.; Deng, L.; Luo, Q.; Li, X.; Jiang, J. Promoting Oxygen Reduction Reaction on Carbon-Based Materials by Selective Hydrogen Bonding. *Chemistry Europe* **2023**. https://doi.org/10.1002/cssc.202300082.

50. Mitchell, S.; Pérez-Ramírez, J. Single Atom Catalysis: A Decade of Stunning Progress and the Promise for a Bright Future. *Nature Communications* **2020**, *11* (1), 4302. https://doi.org/10.1038/s41467-020-18182-5.

51. Li, B.; Xie, H.; Yang, C.; Shi, C.; He, C.; Zhao, N.; Liu, E. Unraveling the Mechanism of Ligands Regulating Electronic Structure of MN4 Sites with Optimized ORR Catalytic Performance. *Applied Surface Science* **2022**, *595*, 153526. https://doi.org/10.1016/j.apsusc.2022.153526.

52. Rosen, A. S.; Notestein, J. M.; Snurr, R. Q. Structure–Activity Relationships That Identify Metal–Organic Framework Catalysts for Methane Activation. *ACS Catalysis* **2019**, *9* (4), 3576–3587. https://doi.org/10.1021/acscatal.8b05178.

53. Yang, Z.; Gao, W.; Jiang, Q. A Machine Learning Scheme for the Catalytic Activity of Alloys with Intrinsic Descriptors. *Journal of Materials Chemistry A* **2020**, *8* (34), 17507–17515. https://doi.org/10.1039/d0ta06203k.

7. Appendix

7.1. Appendix 1. (a) ΔG_{OH^*} Volcano Chart and (b) ΔG_{O^*} Volcano Chart

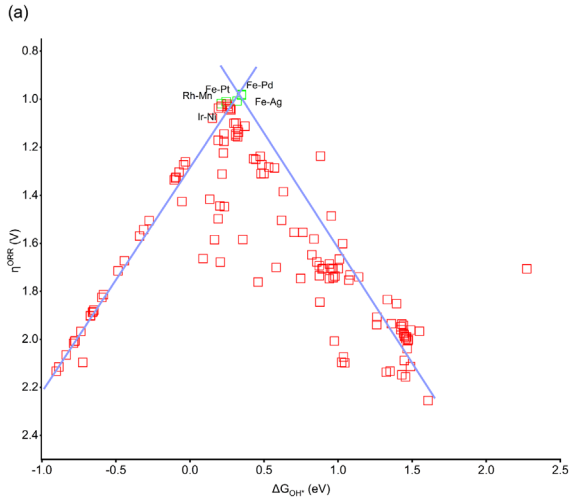

Figure A1. (a) ΔG_{OH^*} Volcano Plot for the 144 SACs. The optimal region of binding energies for ΔG_{OH^*} (~0.15-0.37 eV) is around the peak of the graph.

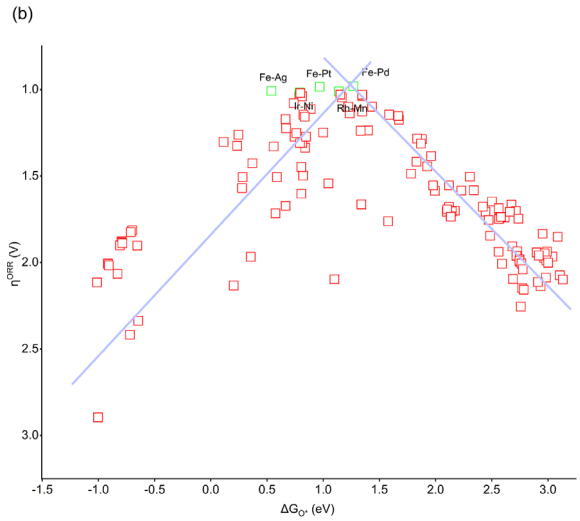

(b) ΔG_{O^*} Volcano Plot for the 144 SACs. The optimal region of binding energies for ΔG_{O^*} (~1.0-1.3 eV) is around the peak of the graph.

7.2. Appendix 2. (a) ΔG_{OH^*} Heatmap and (b) ΔG_{O^*} Heatmap

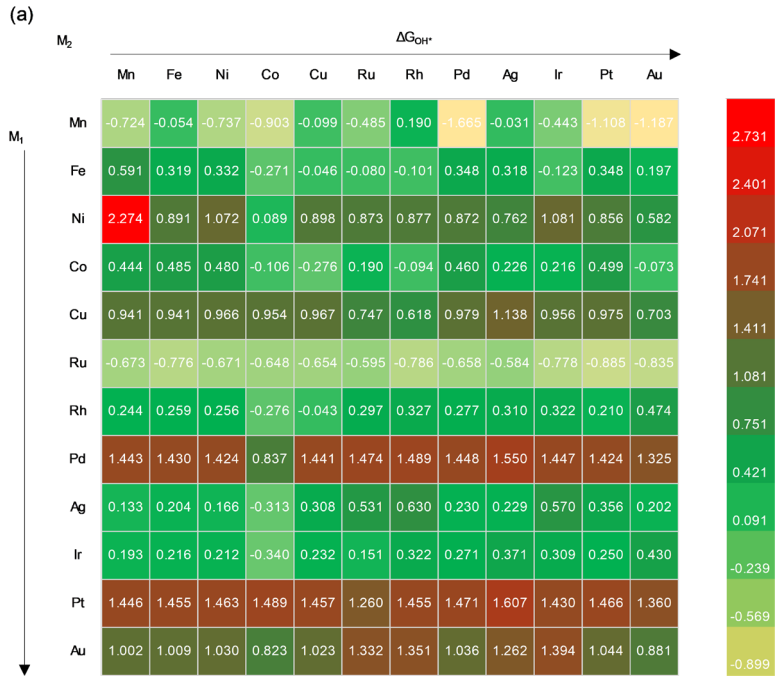

Figure A2. (a) ΔG_{OH^*} binding energy heatmap for 144 SACs. Green values indicate optimal binding energies, red values indicate too strong binding energies and yellow values indicate too weak binding energies.

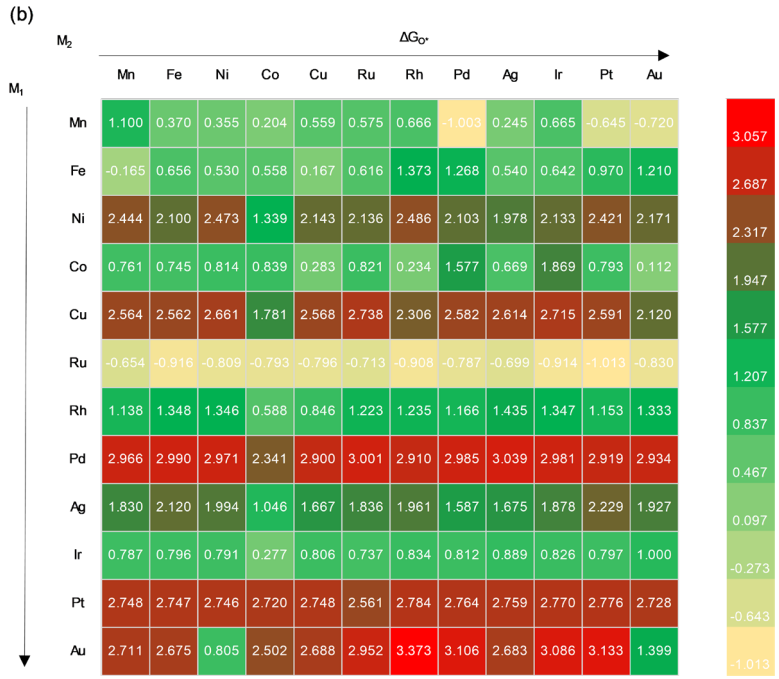

(b). ΔG_{O^*} binding energy heatmap for 144 SACs. Green values indicate optimal binding energies, red values indicate too strong binding energies and yellow values indicate too weak binding energies.

7.3. Appendix 3. Evaluating Descriptor ψ

As suggested by Yang, *et. al.* [53], the electronic descriptor ψ has shown promise in predicting adsorption energies, which are closely correlated with overpotential. The electronic descriptor ψ is defined as the following when it is describing the surface of pure transition metals (TMs):

$$\psi = \frac{S_V^2}{X^\beta}$$

X and S_V are the electronegativity of the TM and the valence electron number, respectively. β is set to $\frac{1}{2}$ for Ag and Au, and $\beta = 1$ for other Transition Metals as suggested by Yang, *et. al.* [53]. Three ETR models were constructed to gauge the predictive capability of the ψ descriptor for predicting overpotential:

1. Incorporating the ψ descriptor for both M_1 and M_2 metals as input features
2. Incorporating only the ψ descriptor for the M_1 metal as the input feature
3. Incorporating only the ψ descriptor for the M_2 metal as the input feature

For training and testing purposes, we randomly allocated 80% of the 144 metals as training data, while the remaining 20% served as testing data. The obtained results are presented in Table A1, illustrating the outcomes of the ETR models.

Models	Coefficient (r)	r^2	RMSE
ETR ψ (M_1 and M_2) Training	1.00	1.00	0.000
ETR ψ (M_1 and M_2) Testing	-0.238	0.057	0.486
ETR ψ (M_1) Training	0.927	0.860	0.142
ETR ψ (M_1) Testing	0.085	0.007	0.435
ETR ψ (M_2) Training	0.940	0.884	0.129
ETR ψ (M_2) Testing	0.231	0.054	0.458

Table A1. ψ descriptor ETR training and testing results. Three scenarios are evaluated using ETR: 1) ψ (M_1 and M_2) is trained and tested using ETR. 2) ψ (M_1 only) is trained and tested using ETR. 3) ψ (M_2 only) is trained and tested using ETR.

Upon evaluating the training and testing data, it appears that the ψ descriptor does not offer a satisfactory prediction of the overpotential. This could be attributed to overfitting. It is also possible that the descriptor is derived from the CO_2 Reduction Reaction (CO_2RR) and may not be effectively

extrapolated to ORR.

To further test the predictability of ψ in the scope of our project, we incorporated ψ as a feature within the SISSO algorithm. Intriguingly, despite its potential relevance, the SISSO algorithm did not include ψ as one of the features in the resulting equation, indicating that other descriptors had a more pronounced influence on the overpotential than the electronic descriptor.

Upon comparing the results obtained from the ETR models and the SISSO model, it becomes evident that the features selected by SISSO exert a significantly greater influence on the overpotential of the system than the electronic descriptor ψ.

7.4. Appendix 4. Predicting Binding Energies

Additionally, overpotential can be roughly estimated by the binding free energies of OOH*, O*, and OH* intermediates. To this end, we developed a third SISSO model employing all sixteen features to predict the binding energies of intermediates, subsequently utilizing these predictions to calculate the overpotential. The model exhibited strong predictability for the binding energies of intermediates, particularly with respect to ΔG_{OOH*} and ΔG_{OH*}. However, it should be noted that the calculated overpotential displayed lower predictability compared to both the ASPM and RSPM, most likely due to the accumulation of errors when predicting the binding free energies. A summary of the performance is presented in Table A2.

Models	Coefficient (r)	r^2	RMSE	MAX AE
Predicted ΔG_{O*}	0.928	0.861	0.440	1.921
Predicted ΔG_{OH*}	0.921	0.848	0.284	1.450
Predicted ΔG_{OOH*}	0.885	0.306	0.872	0.782
Predicted Overpotential η (eV) by $\Delta G_{OOH*} + \Delta G_{OH*} + \Delta G_{O*}$	0.764	0.583	0.260	0.973

Table A2. Binding Energies Prediction Model Performance.

7.5. Appendix 5: Free Energy Diagrams (M_1-M_2 Metals)

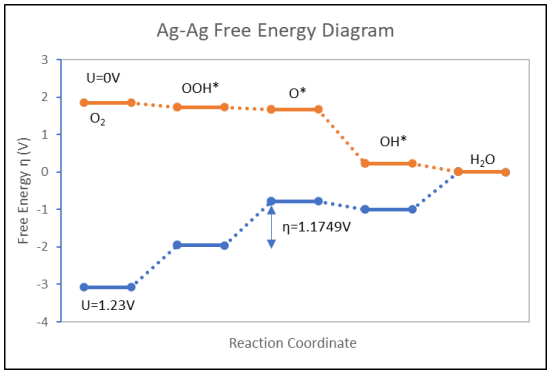

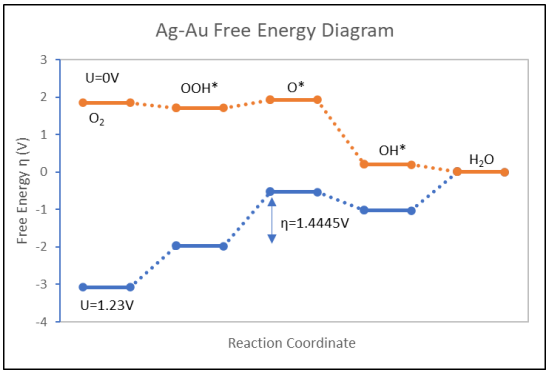

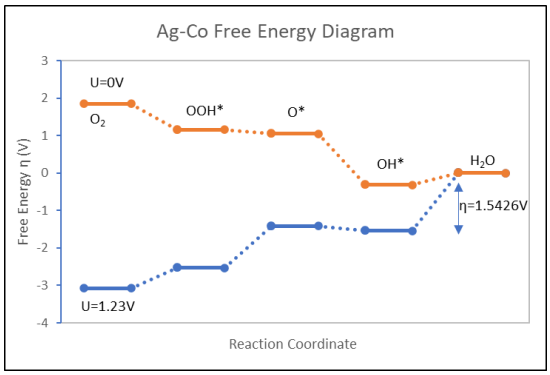

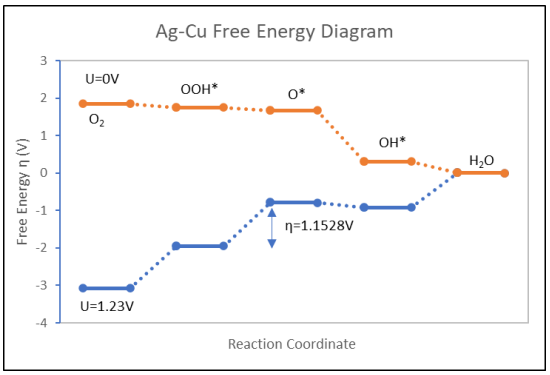

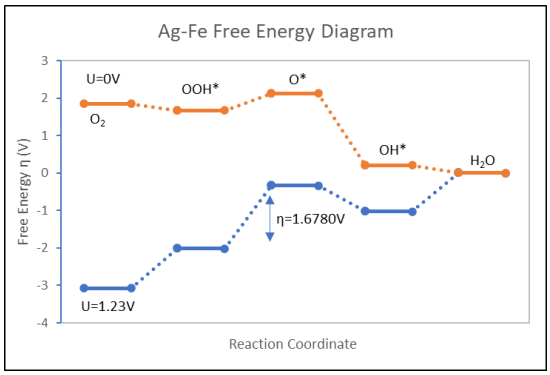

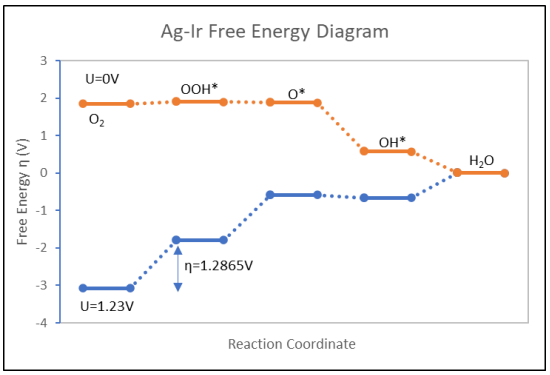

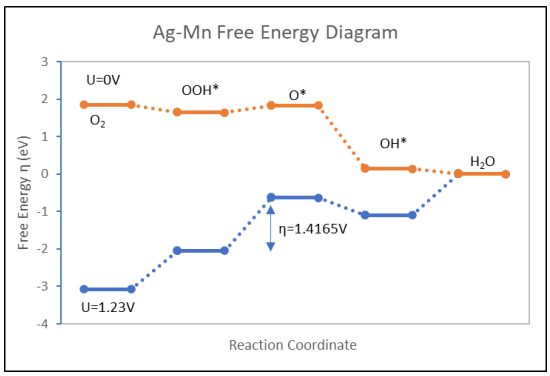

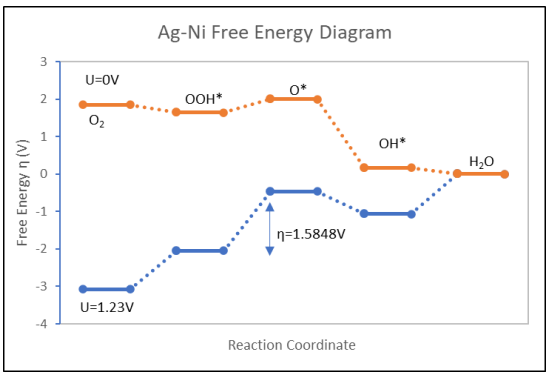

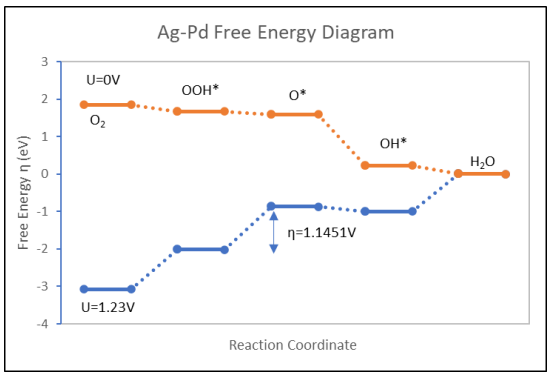
Ag-Pd Free Energy Diagram
U=0V
OOH*
O*
O2
OH*
H2O
η=1.1451V
U=1.23V
Free Energy η (eV)
Reaction Coordinate

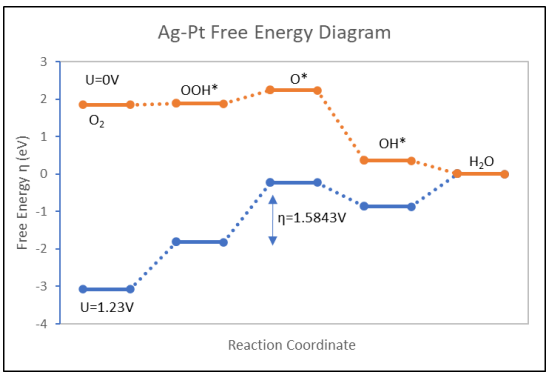
Ag-Pt Free Energy Diagram
U=0V
OOH*
O*
O2
OH*
H2O
η=1.5843V
U=1.23V
Free Energy η (eV)
Reaction Coordinate

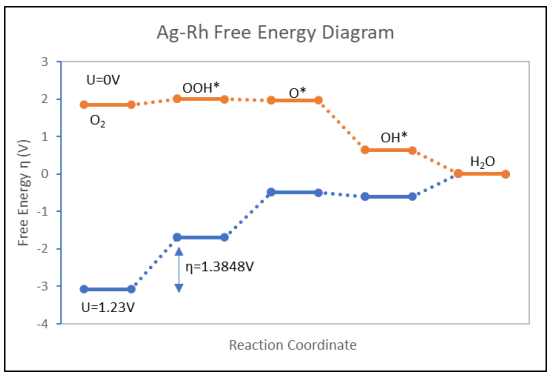
Ag-Rh Free Energy Diagram
U=0V
OOH*
O*
O2
OH*
H2O
η=1.3848V
U=1.23V
Free Energy η (V)
Reaction Coordinate

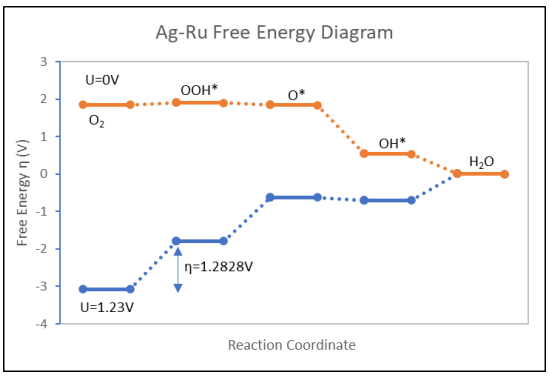
Ag-Ru Free Energy Diagram
U=0V
OOH*
O*
O2
OH*
H2O
η=1.2828V
U=1.23V
Free Energy η (V)
Reaction Coordinate

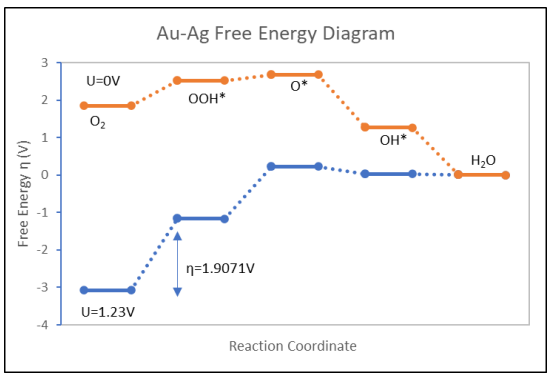
Au-Ag Free Energy Diagram
U=0V
OOH*
O*
O2
OH*
H2O
η=1.9071V
U=1.23V
Free Energy η (V)
Reaction Coordinate

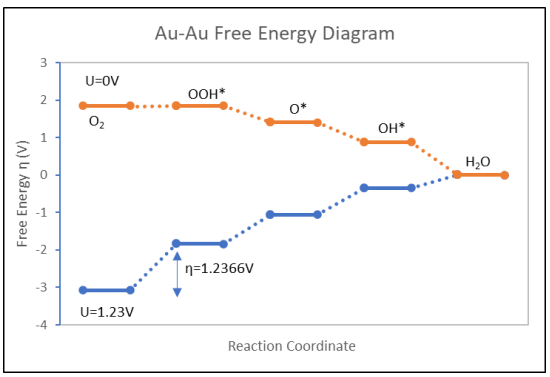
Au-Au Free Energy Diagram
U=0V
OOH*
O*
O2
OH*
H2O
η=1.2366V
U=1.23V
Free Energy η (V)
Reaction Coordinate

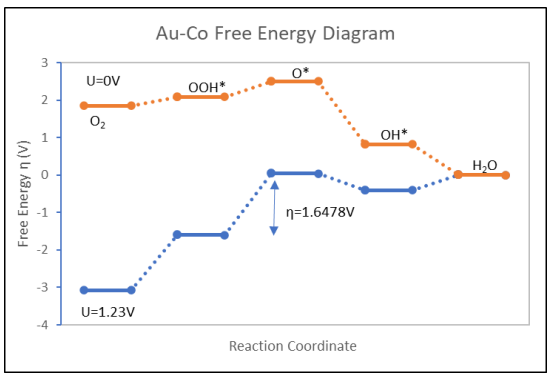
Au-Co Free Energy Diagram
U=0V
OOH*
O*
O2
OH*
H2O
η=1.6478V
U=1.23V
Free Energy η (V)
Reaction Coordinate

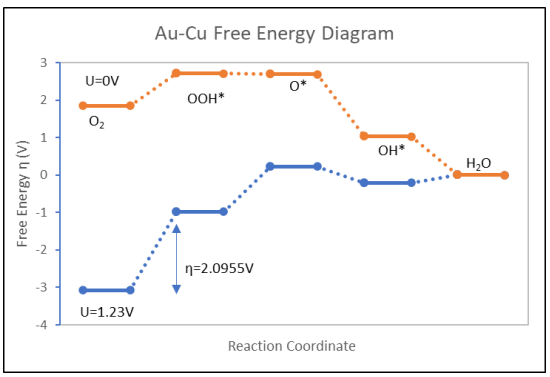
Au-Cu Free Energy Diagram
U=0V
OOH*
O*
O2
OH*
H2O
η=2.0955V
U=1.23V
Free Energy η (V)
Reaction Coordinate

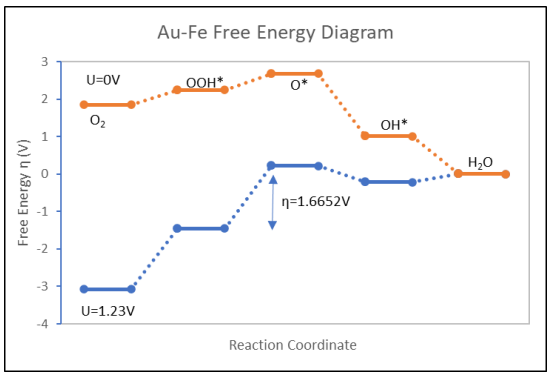
Au-Fe Free Energy Diagram
U=0V
OOH*
O*
O2
OH*
H2O
η=1.6652V
U=1.23V
Free Energy η (V)
Reaction Coordinate

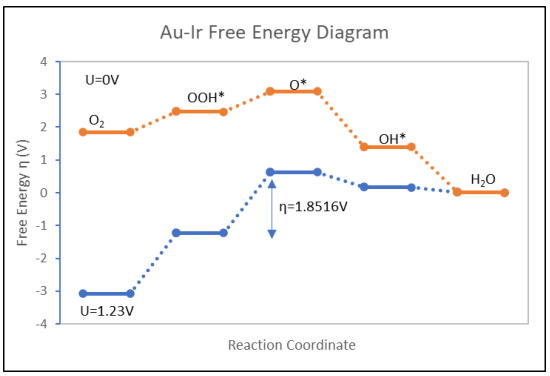
Au-Ir Free Energy Diagram
U=0V
OOH*
O*
O2
OH*
H2O
η=1.8516V
U=1.23V
Free Energy η (V)
Reaction Coordinate

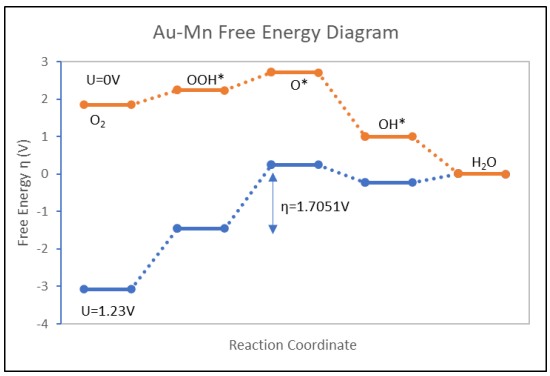
Au-Mn Free Energy Diagram
U=0V
OOH*
O*
O2
OH*
H2O
η=1.7051V
U=1.23V
Free Energy η (V)
Reaction Coordinate

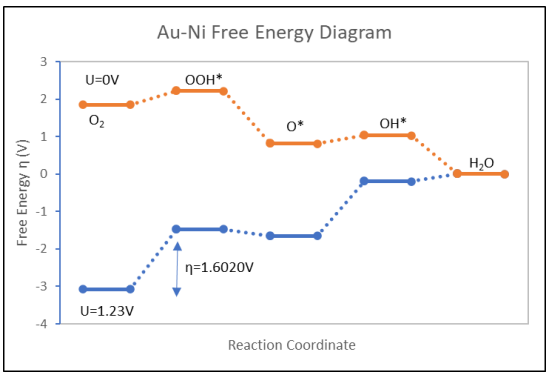
Au-Ni Free Energy Diagram
U=0V
OOH*
O*
O2
OH*
H2O
η=1.6020V
U=1.23V
Free Energy η (V)
Reaction Coordinate

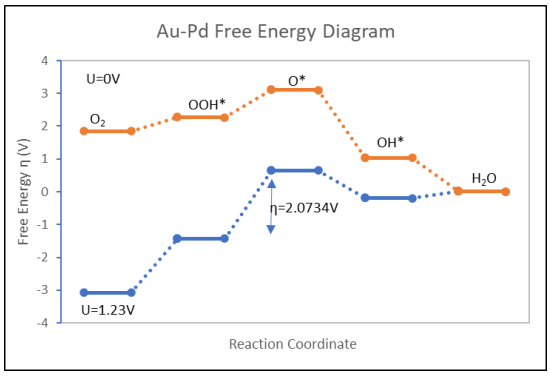
Au-Pd Free Energy Diagram
U=0V
OOH*
O*
O2
OH*
H2O
η=2.0734V
U=1.23V
Free Energy η (V)
Reaction Coordinate

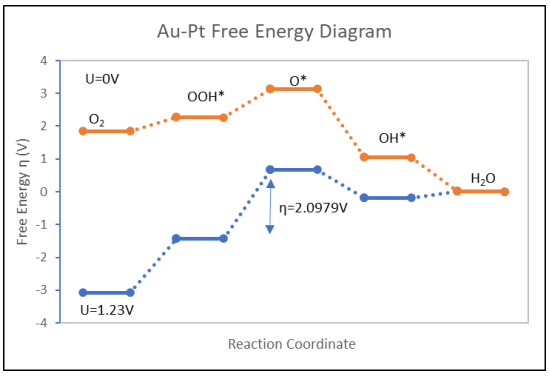
Au-Pt Free Energy Diagram
U=0V
OOH*
O*
O2
OH*
H2O
η=2.0979V
U=1.23V
Free Energy η (V)
Reaction Coordinate

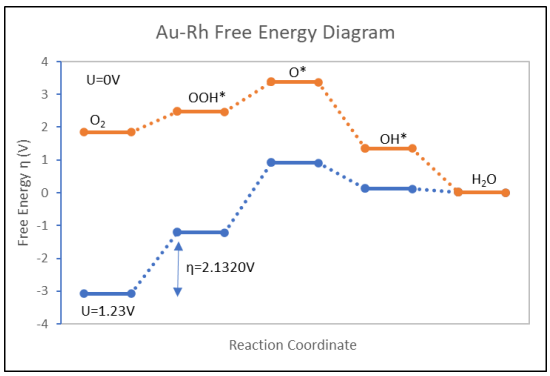
Au-Rh Free Energy Diagram
U=0V
OOH*
O*
O2
OH*
H2O
η=2.1320V
U=1.23V
Free Energy η (V)
Reaction Coordinate

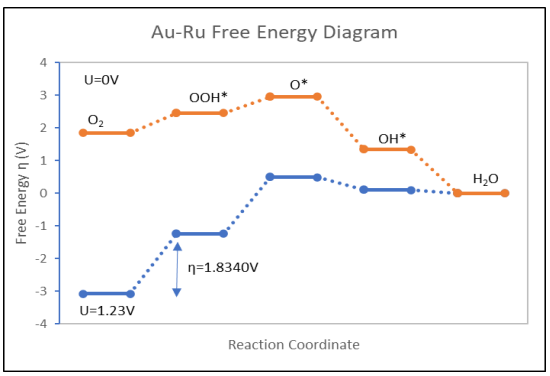
Au-Ru Free Energy Diagram
U=0V
OOH*
O*
O2
OH*
H2O
η=1.8340V
U=1.23V
Free Energy η (V)
Reaction Coordinate

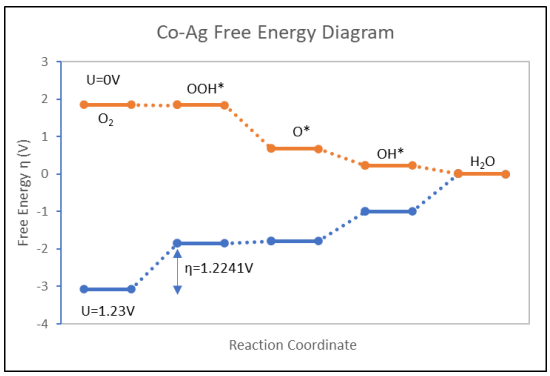
Co-Ag Free Energy Diagram
U=0V
OOH*
O*
OH*
H2O
O2
η=1.2241V
U=1.23V
Free Energy η (V)
Reaction Coordinate

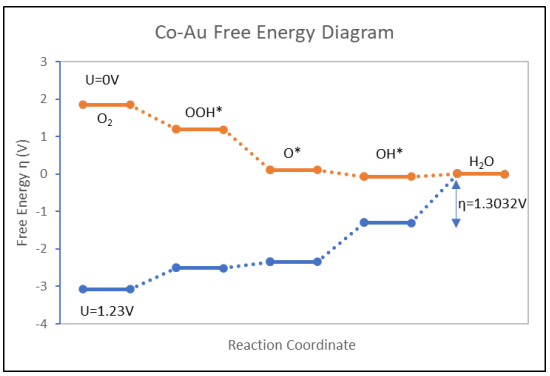
Co-Au Free Energy Diagram
U=0V
OOH*
O*
OH*
H2O
O2
η=1.3032V
U=1.23V
Free Energy η (V)
Reaction Coordinate

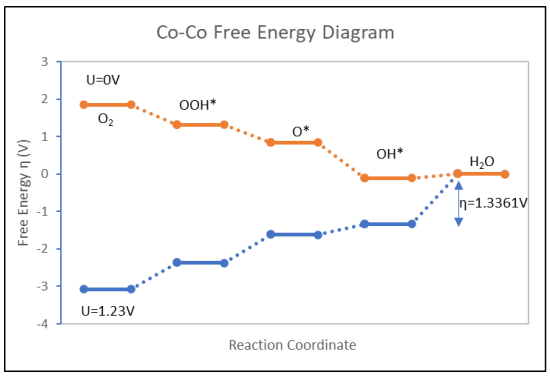
Co-Co Free Energy Diagram
U=0V
OOH*
O*
OH*
H2O
O2
η=1.3361V
U=1.23V
Free Energy η (V)
Reaction Coordinate

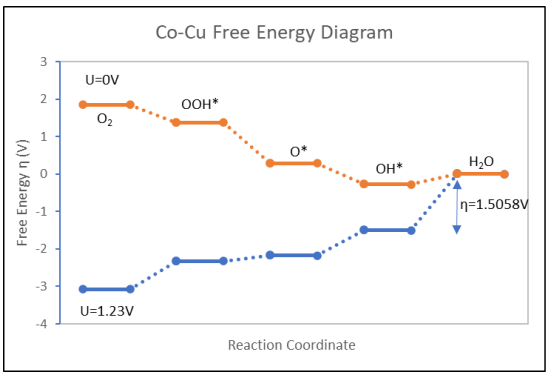
Co-Cu Free Energy Diagram
U=0V
OOH*
O*
OH*
H2O
O2
η=1.5058V
U=1.23V
Free Energy η (V)
Reaction Coordinate

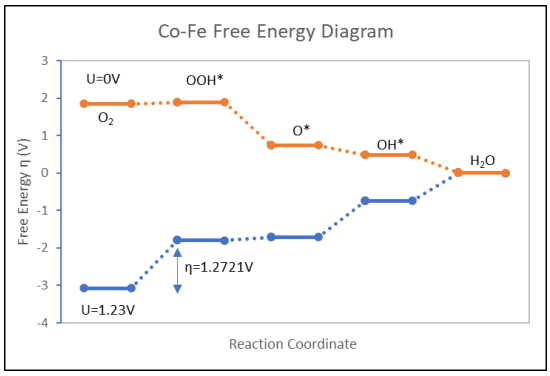
Co-Fe Free Energy Diagram
U=0V
OOH*
O*
OH*
H2O
O2
η=1.2721V
U=1.23V
Free Energy η (V)
Reaction Coordinate

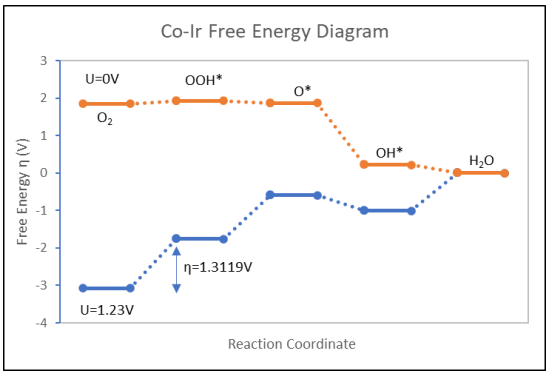
Co-Ir Free Energy Diagram
U=0V
OOH*
O*
OH*
H2O
O2
η=1.3119V
U=1.23V
Free Energy η (V)
Reaction Coordinate

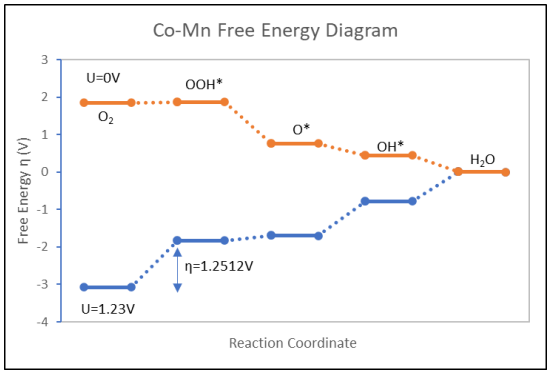
Co-Mn Free Energy Diagram
U=0V
OOH*
O*
OH*
H2O
O2
η=1.2512V
U=1.23V
Free Energy η (V)
Reaction Coordinate

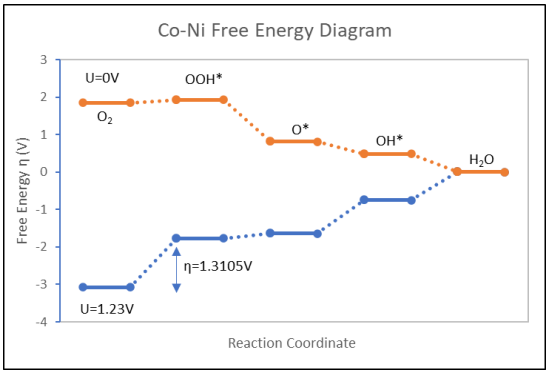
Co-Ni Free Energy Diagram
U=0V
OOH*
O*
OH*
H2O
O2
η=1.3105V
U=1.23V
Free Energy η (V)
Reaction Coordinate

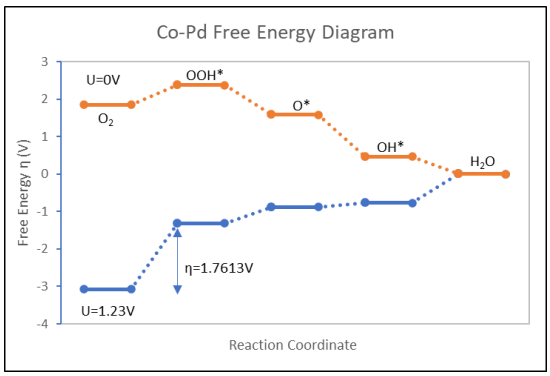
Co-Pd Free Energy Diagram
U=0V
OOH*
O*
OH*
H2O
O2
η=1.7613V
U=1.23V
Free Energy η (V)
Reaction Coordinate

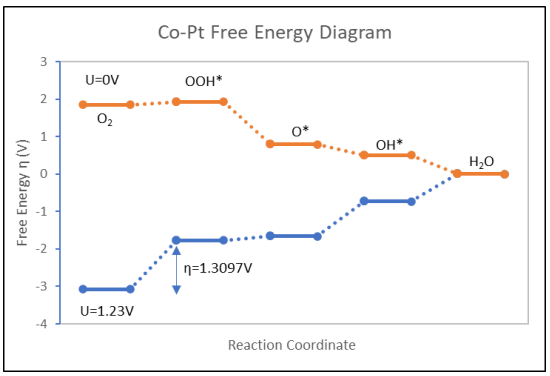
Co-Pt Free Energy Diagram
U=0V
OOH*
O*
OH*
H2O
O2
η=1.3097V
U=1.23V
Free Energy η (V)
Reaction Coordinate

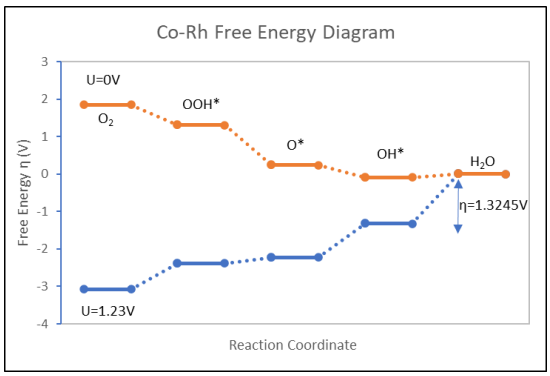
Co-Rh Free Energy Diagram
U=0V
OOH*
O*
OH*
H2O
O2
η=1.3245V
U=1.23V
Free Energy η (V)
Reaction Coordinate

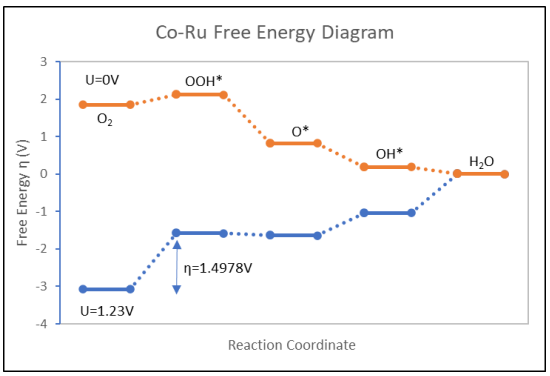
Co-Ru Free Energy Diagram
U=0V
OOH*
O*
OH*
H2O
O2
η=1.4978V
U=1.23V
Free Energy η (V)
Reaction Coordinate

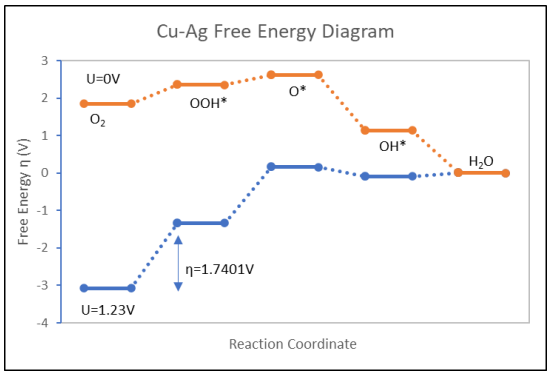
Cu-Ag Free Energy Diagram
U=0V
OOH*
O*
OH*
H2O
O2
η=1.7401V
U=1.23V
Free Energy η (V)
Reaction Coordinate

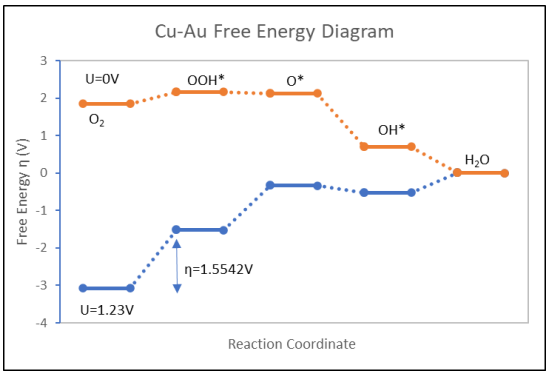
Cu-Au Free Energy Diagram
U=0V
OOH*
O*
OH*
H2O
O2
η=1.5542V
U=1.23V
Free Energy η (V)
Reaction Coordinate

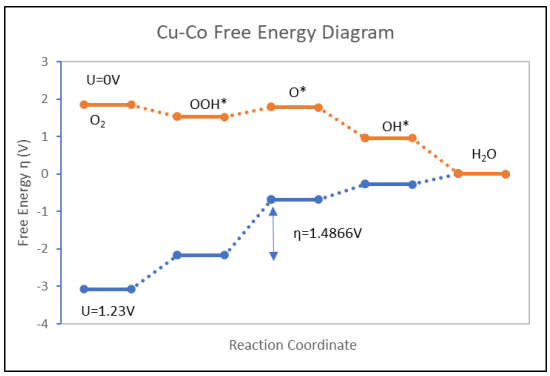
Cu-Co Free Energy Diagram
U=0V
OOH*
O*
OH*
H2O
O2
η=1.4866V
U=1.23V
Free Energy η (V)
Reaction Coordinate

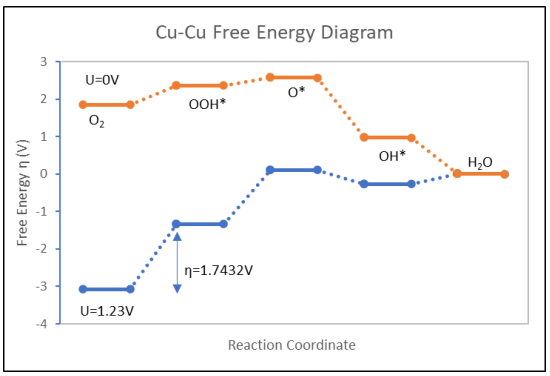
Cu-Cu Free Energy Diagram
U=0V
OOH*
O*
OH*
H2O
O2
η=1.7432V
U=1.23V
Free Energy η (V)
Reaction Coordinate

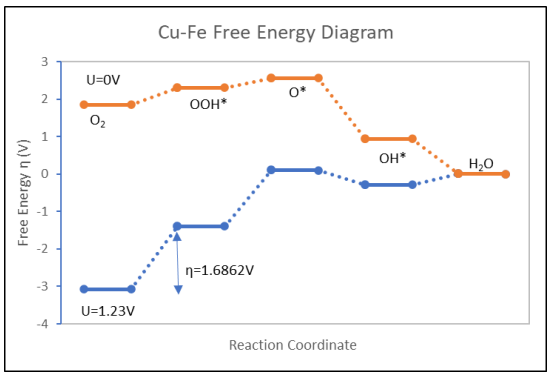
Cu-Fe Free Energy Diagram
U=0V
O2
OOH*
O*
OH*
H2O
η=1.6862V
U=1.23V
Free Energy η (V)
Reaction Coordinate

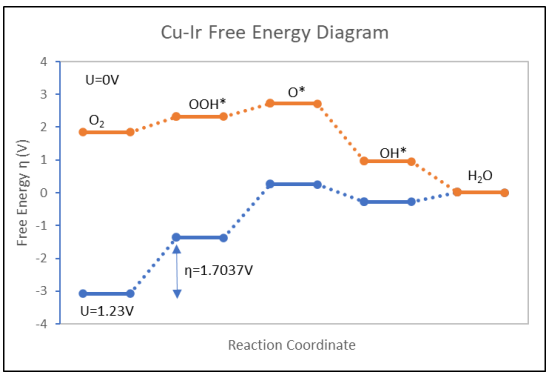
Cu-Ir Free Energy Diagram
U=0V
O2
OOH*
O*
OH*
H2O
η=1.7037V
U=1.23V
Free Energy η (V)
Reaction Coordinate

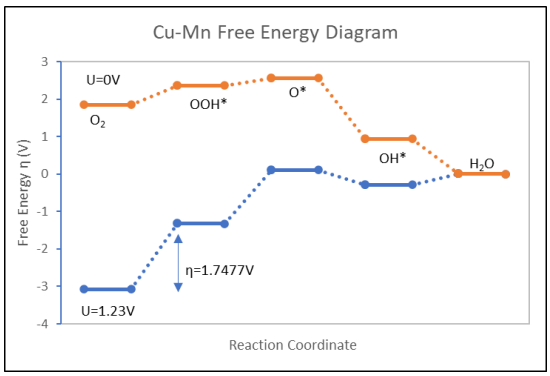
Cu-Mn Free Energy Diagram
U=0V
O2
OOH*
O*
OH*
H2O
η=1.7477V
U=1.23V
Free Energy η (V)
Reaction Coordinate

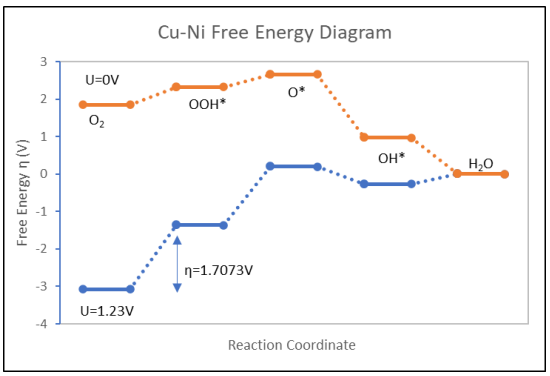
Cu-Ni Free Energy Diagram
U=0V
O2
OOH*
O*
OH*
H2O
η=1.7073V
U=1.23V
Free Energy η (V)
Reaction Coordinate

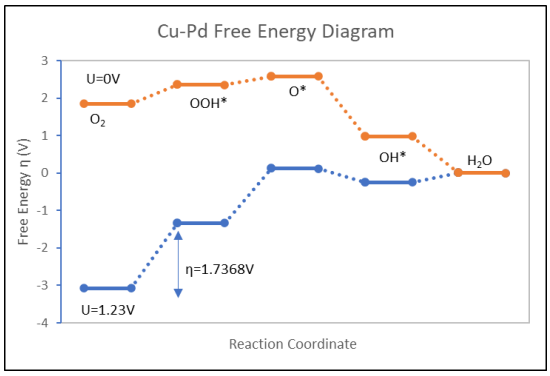
Cu-Pd Free Energy Diagram
U=0V
O2
OOH*
O*
OH*
H2O
η=1.7368V
U=1.23V
Free Energy η (V)
Reaction Coordinate

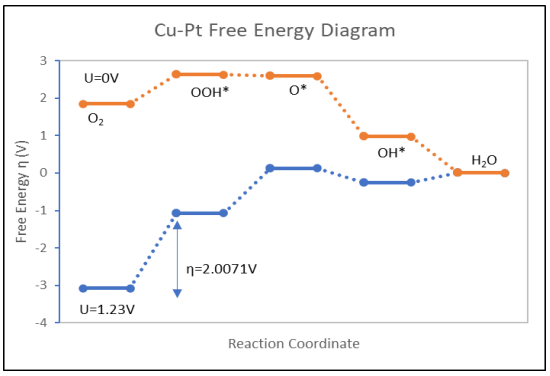
Cu-Pt Free Energy Diagram
U=0V
O2
OOH*
O*
OH*
H2O
η=2.0071V
U=1.23V
Free Energy η (V)
Reaction Coordinate

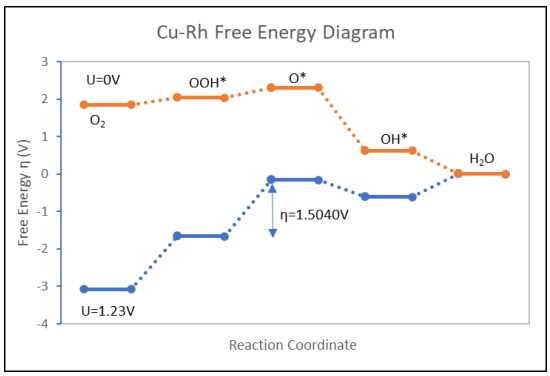
Cu-Rh Free Energy Diagram
U=0V
O2
OOH*
O*
OH*
H2O
η=1.5040V
U=1.23V
Free Energy η (V)
Reaction Coordinate

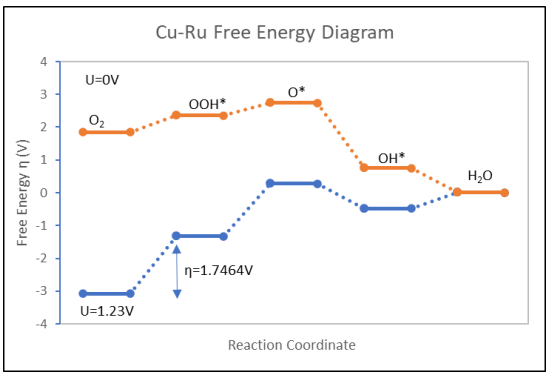
Cu-Ru Free Energy Diagram
U=0V
O2
OOH*
O*
OH*
H2O
η=1.7464V
U=1.23V
Free Energy η (V)
Reaction Coordinate

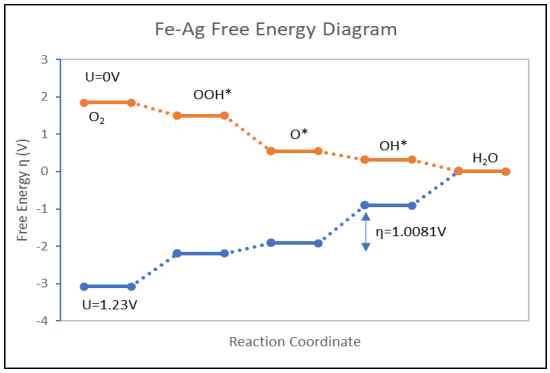
Fe-Ag Free Energy Diagram
U=0V
OOH*
O*
OH*
H2O
O2
η=1.0081V
U=1.23V
Free Energy η (V)
Reaction Coordinate

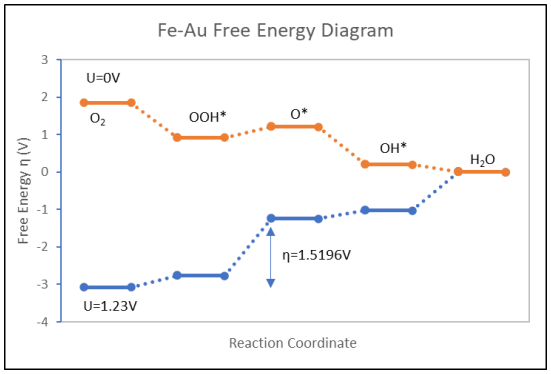
Fe-Au Free Energy Diagram
U=0V
OOH*
O*
OH*
H2O
O2
η=1.5196V
U=1.23V
Free Energy η (V)
Reaction Coordinate

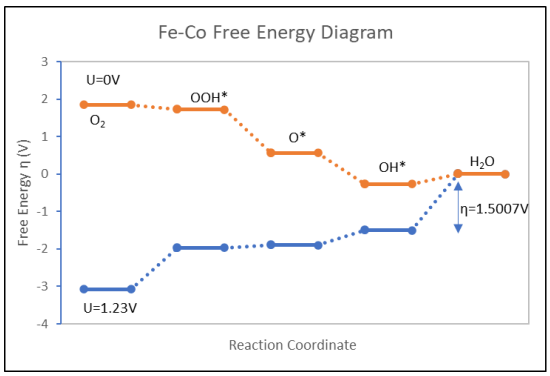
Fe-Co Free Energy Diagram
U=0V
OOH*
O*
OH*
H2O
O2
η=1.5007V
U=1.23V
Free Energy η (V)
Reaction Coordinate

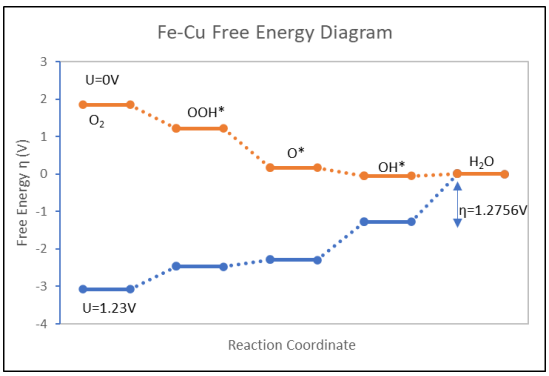
Fe-Cu Free Energy Diagram
U=0V
OOH*
O*
OH*
H2O
O2
η=1.2756V
U=1.23V
Free Energy η (V)
Reaction Coordinate

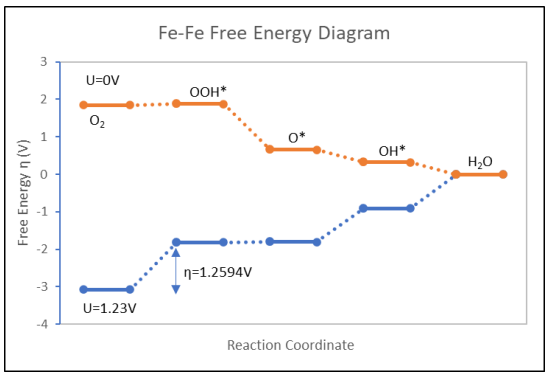
Fe-Fe Free Energy Diagram
U=0V
OOH*
O*
OH*
H2O
O2
η=1.2594V
U=1.23V
Free Energy η (V)
Reaction Coordinate

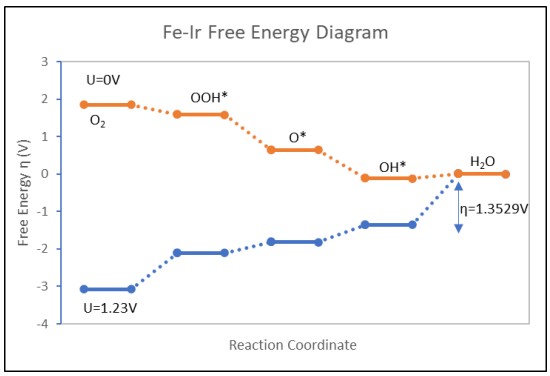
Fe-Ir Free Energy Diagram
U=0V
OOH*
O*
OH*
H2O
O2
η=1.3529V
U=1.23V
Free Energy η (V)
Reaction Coordinate

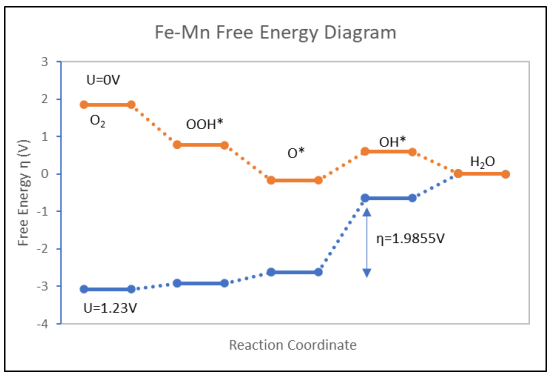
Fe-Mn Free Energy Diagram
U=0V
OOH*
O*
OH*
H2O
O2
η=1.9855V
U=1.23V
Free Energy η (V)
Reaction Coordinate

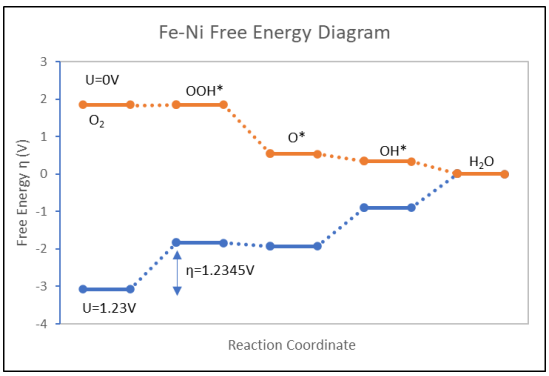
Fe-Ni Free Energy Diagram
U=0V
OOH*
O*
OH*
H2O
O2
η=1.2345V
U=1.23V
Free Energy η (V)
Reaction Coordinate

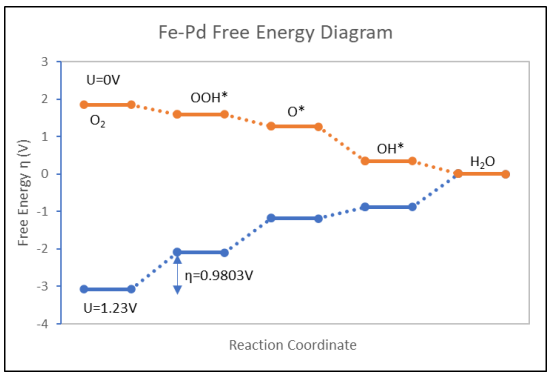
Fe-Pd Free Energy Diagram
U=0V
O2
OOH*
O*
OH*
H2O
η=0.9803V
U=1.23V
Free Energy η (V)
Reaction Coordinate

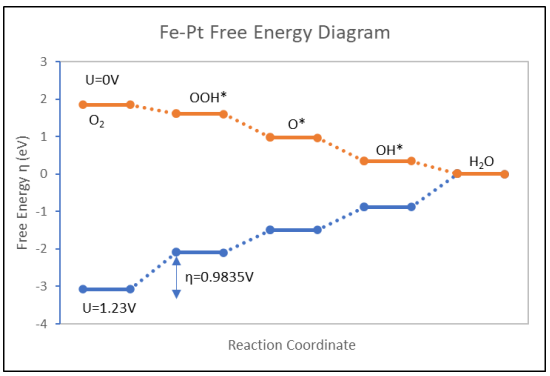
Fe-Pt Free Energy Diagram
U=0V
O2
OOH*
O*
OH*
H2O
η=0.9835V
U=1.23V
Free Energy η (eV)
Reaction Coordinate

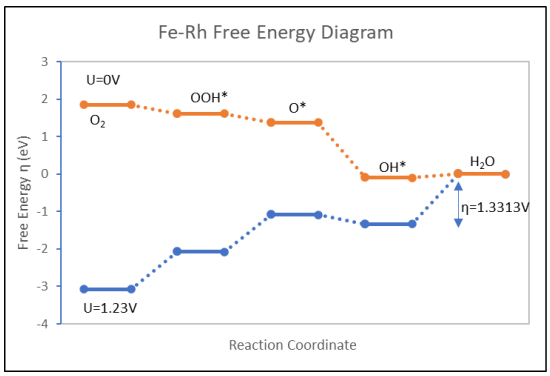
Fe-Rh Free Energy Diagram
U=0V
O2
OOH*
O*
OH*
H2O
η=1.3313V
U=1.23V
Free Energy η (eV)
Reaction Coordinate

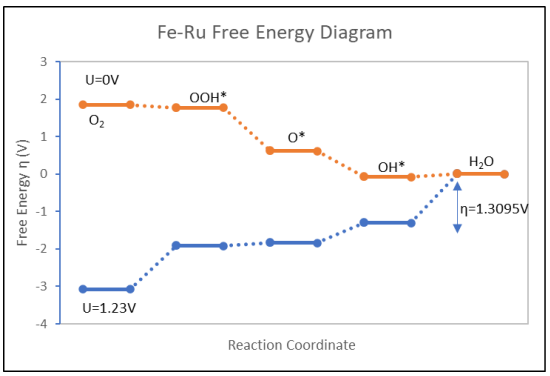
Fe-Ru Free Energy Diagram
U=0V
O2
OOH*
O*
OH*
H2O
η=1.3095V
U=1.23V
Free Energy η (V)
Reaction Coordinate

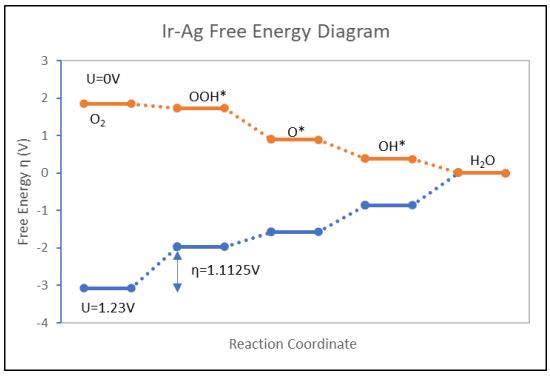
Ir-Ag Free Energy Diagram
U=0V
O2
OOH*
O*
OH*
H2O
η=1.1125V
U=1.23V
Free Energy η (V)
Reaction Coordinate

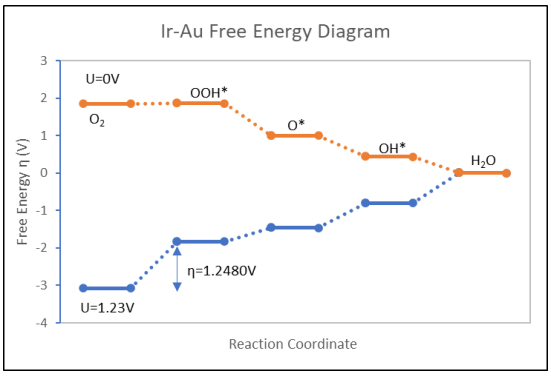
Ir-Au Free Energy Diagram
U=0V
O2
OOH*
O*
OH*
H2O
η=1.2480V
U=1.23V
Free Energy η (V)
Reaction Coordinate

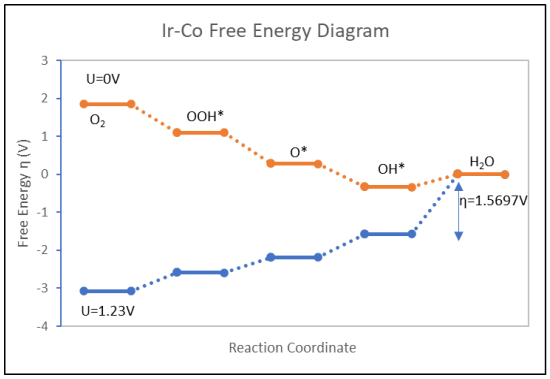
Ir-Co Free Energy Diagram
U=0V
O2
OOH*
O*
OH*
H2O
η=1.5697V
U=1.23V
Free Energy η (V)
Reaction Coordinate

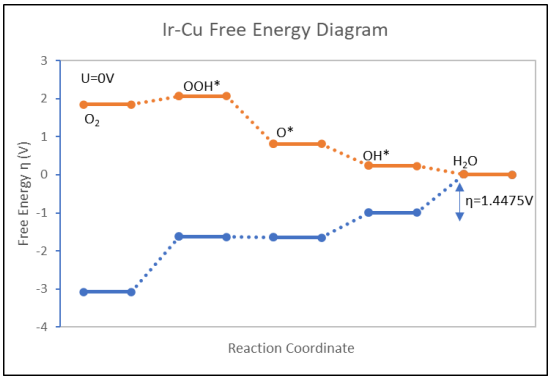
Ir-Cu Free Energy Diagram
U=0V
O2
OOH*
O*
OH*
H2O
η=1.4475V
U=1.23V
Free Energy η (V)
Reaction Coordinate

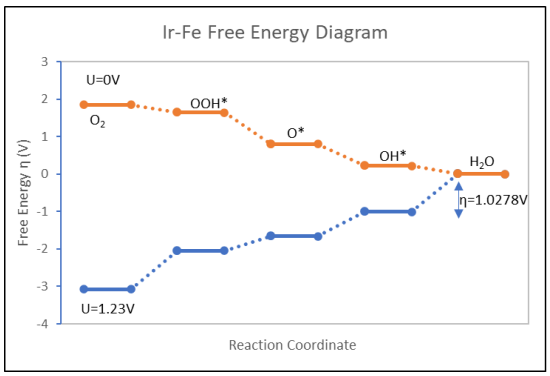
Ir-Fe Free Energy Diagram
U=0V
O2
OOH*
O*
OH*
H2O
η=1.0278V
U=1.23V
Free Energy η (V)
Reaction Coordinate

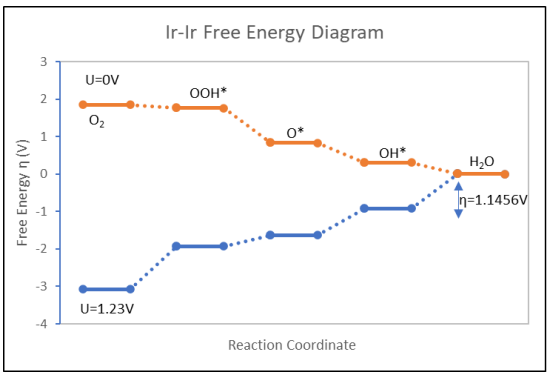
Ir-Ir Free Energy Diagram
U=0V
O2
OOH*
O*
OH*
H2O
η=1.1456V
U=1.23V
Free Energy η (V)
Reaction Coordinate

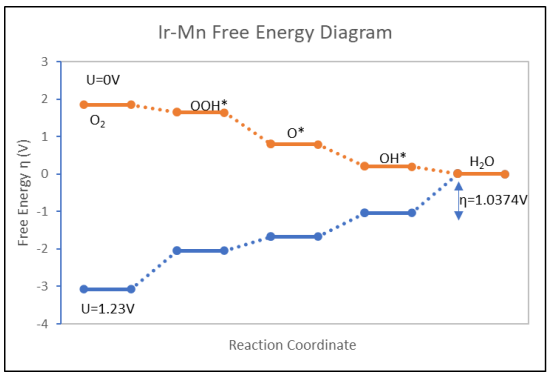
Ir-Mn Free Energy Diagram
U=0V
O2
OOH*
O*
OH*
H2O
η=1.0374V
U=1.23V
Free Energy η (V)
Reaction Coordinate

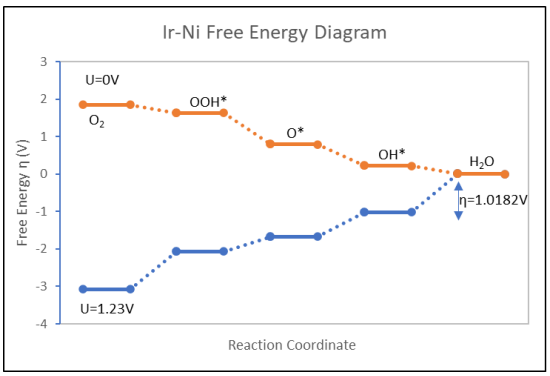
Ir-Ni Free Energy Diagram
U=0V
O2
OOH*
O*
OH*
H2O
η=1.0182V
U=1.23V
Free Energy η (V)
Reaction Coordinate

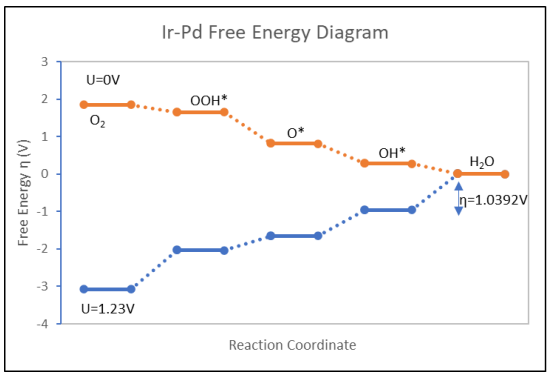
Ir-Pd Free Energy Diagram
U=0V
O2
OOH*
O*
OH*
H2O
η=1.0392V
U=1.23V
Free Energy η (V)
Reaction Coordinate

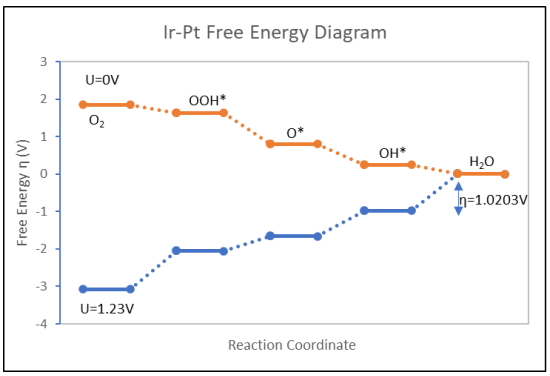
Ir-Pt Free Energy Diagram
U=0V
O2
OOH*
O*
OH*
H2O
η=1.0203V
U=1.23V
Free Energy η (V)
Reaction Coordinate

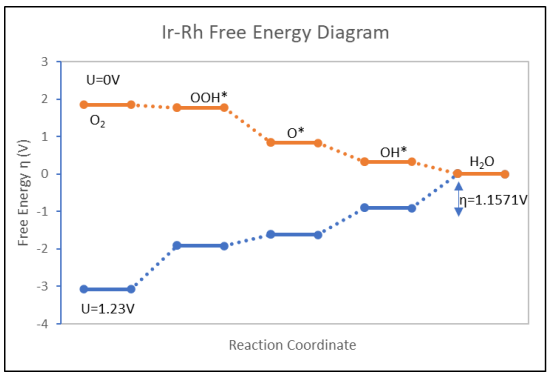
Ir-Rh Free Energy Diagram
U=0V
O2
OOH*
O*
OH*
H2O
η=1.1571V
U=1.23V
Free Energy η (V)
Reaction Coordinate

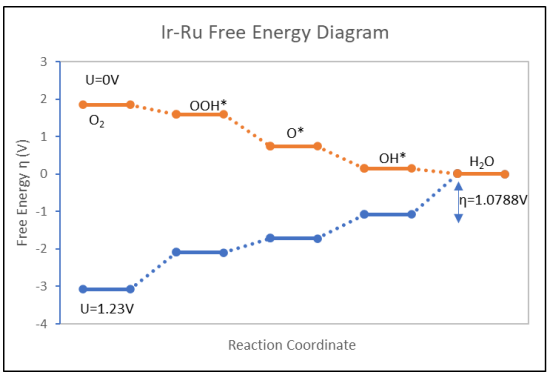
Ir-Ru Free Energy Diagram
U=0V
O2
OOH*
O*
OH*
H2O
η=1.0788V
U=1.23V
Free Energy η (V)
Reaction Coordinate

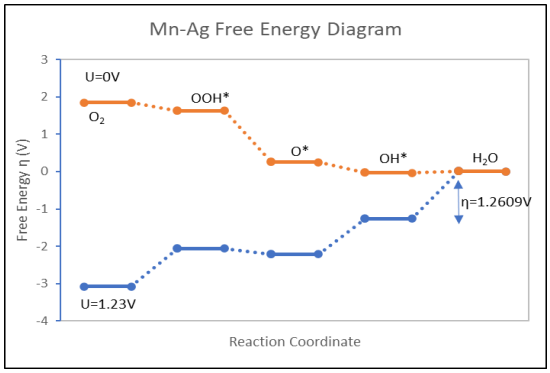
Mn-Ag Free Energy Diagram
U=0V
O2
OOH*
O*
OH*
H2O
η=1.2609V
U=1.23V
Free Energy η (V)
Reaction Coordinate

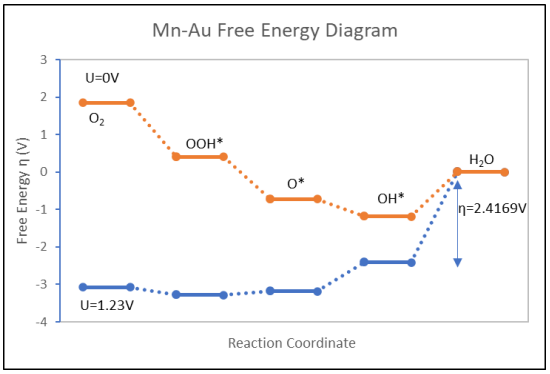
Mn-Au Free Energy Diagram
U=0V
O2
OOH*
O*
OH*
H2O
η=2.4169V
U=1.23V
Free Energy η (V)
Reaction Coordinate

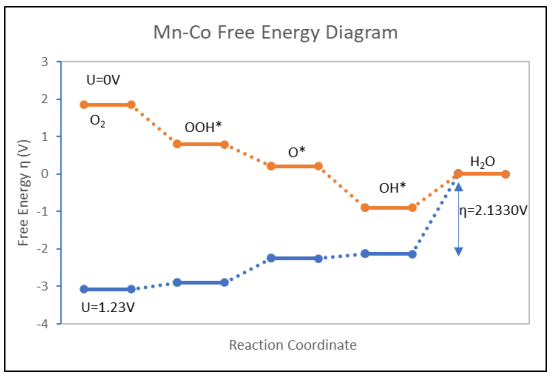
Mn-Co Free Energy Diagram
U=0V
O2
OOH*
O*
OH*
H2O
η=2.1330V
U=1.23V
Free Energy η (V)
Reaction Coordinate

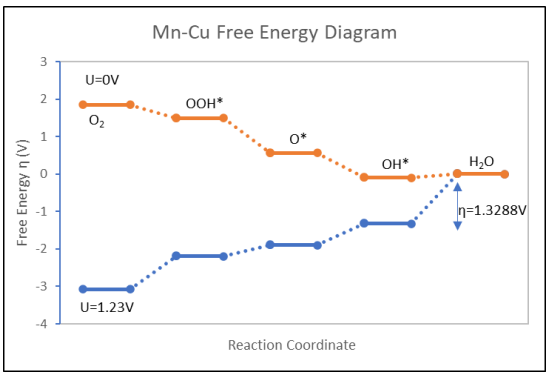
Mn-Cu Free Energy Diagram
U=0V
O2
OOH*
O*
OH*
H2O
η=1.3288V
U=1.23V
Free Energy η (V)
Reaction Coordinate

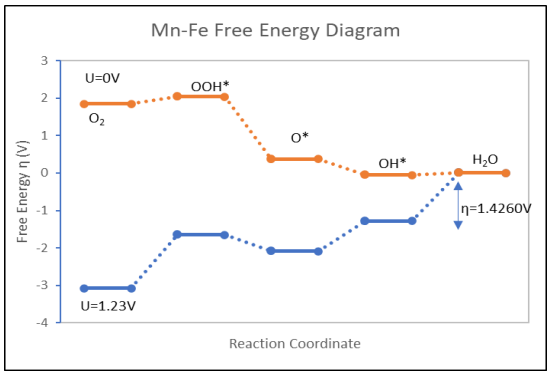
Mn-Fe Free Energy Diagram
U=0V
O2
OOH*
O*
OH*
H2O
η=1.4260V
U=1.23V
Free Energy η (V)
Reaction Coordinate

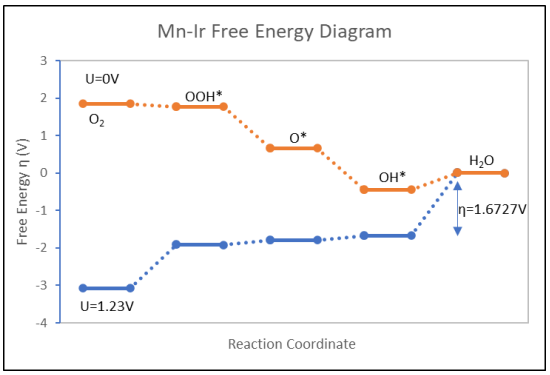
Mn-Ir Free Energy Diagram
U=0V
O2
OOH*
O*
OH*
H2O
η=1.6727V
U=1.23V
Free Energy η (V)
Reaction Coordinate

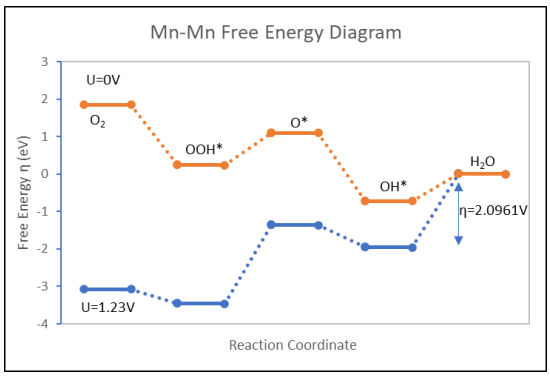
Mn-Mn Free Energy Diagram
U=0V
O2
OOH*
O*
OH*
H2O
η=2.0961V
U=1.23V
Free Energy η (eV)
Reaction Coordinate

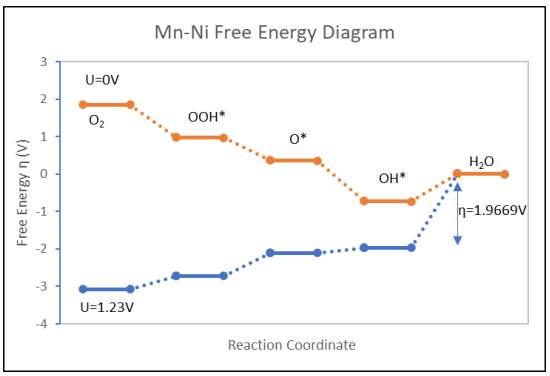
Mn-Ni Free Energy Diagram
U=0V
O2
OOH*
O*
OH*
H2O
η=1.9669V
U=1.23V
Free Energy η (V)
Reaction Coordinate

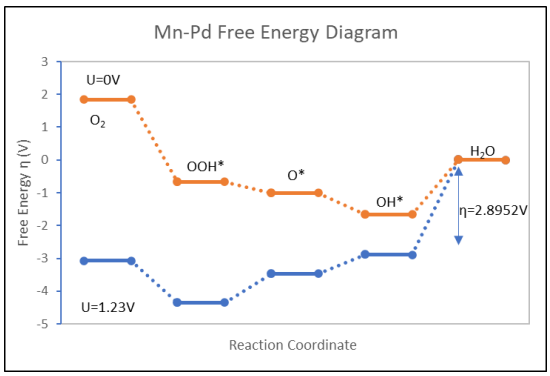
Mn-Pd Free Energy Diagram
U=0V
O2
OOH*
O*
OH*
H2O
η=2.8952V
U=1.23V
Free Energy η (V)
Reaction Coordinate

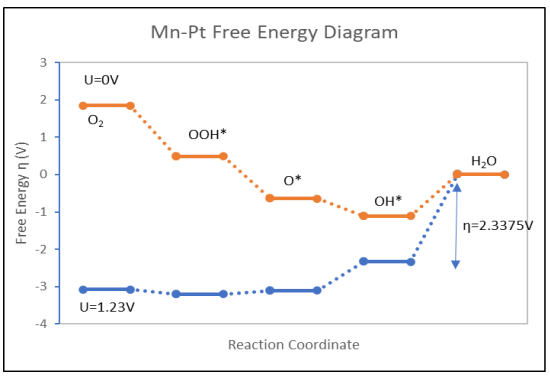
Mn-Pt Free Energy Diagram
U=0V
O2
OOH*
O*
OH*
H2O
η=2.3375V
U=1.23V
Free Energy η (V)
Reaction Coordinate

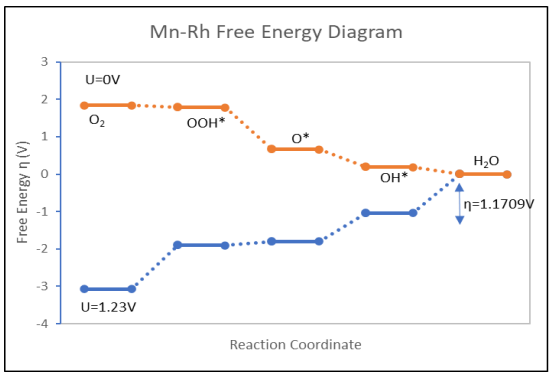
Mn-Rh Free Energy Diagram
U=0V
O2
OOH*
O*
OH*
H2O
η=1.1709V
U=1.23V
Free Energy η (V)
Reaction Coordinate

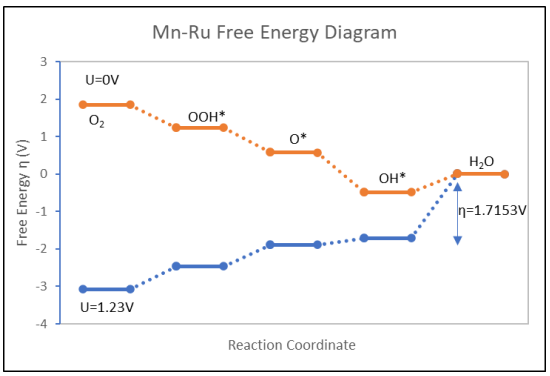
Mn-Ru Free Energy Diagram
U=0V
O2
OOH*
O*
OH*
H2O
η=1.7153V
U=1.23V
Free Energy η (V)
Reaction Coordinate

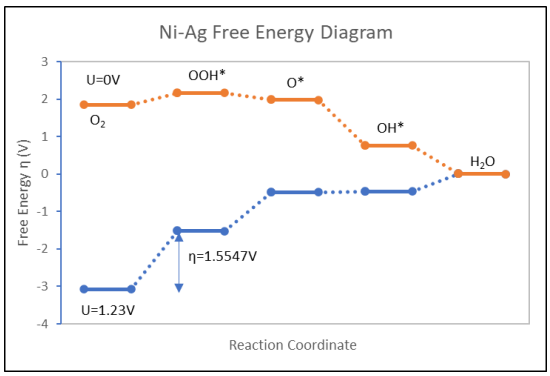
Ni-Ag Free Energy Diagram
U=0V
O2
OOH*
O*
OH*
H2O
η=1.5547V
U=1.23V
Free Energy η (V)
Reaction Coordinate

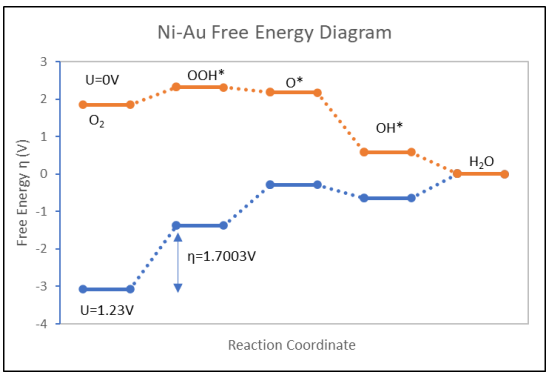
Ni-Au Free Energy Diagram
U=0V
O2
OOH*
O*
OH*
H2O
η=1.7003V
U=1.23V
Free Energy η (V)
Reaction Coordinate

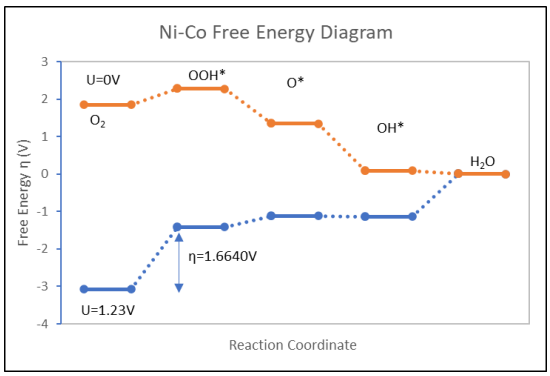
Ni-Co Free Energy Diagram
U=0V
O2
OOH*
O*
OH*
H2O
η=1.6640V
U=1.23V
Free Energy η (V)
Reaction Coordinate

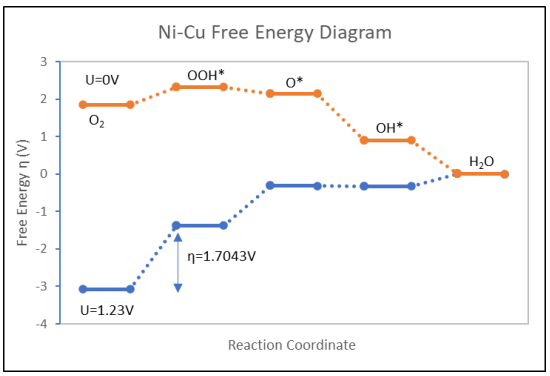
Ni-Cu Free Energy Diagram
U=0V
O2
OOH*
O*
OH*
H2O
η=1.7043V
U=1.23V
Free Energy η (V)
Reaction Coordinate

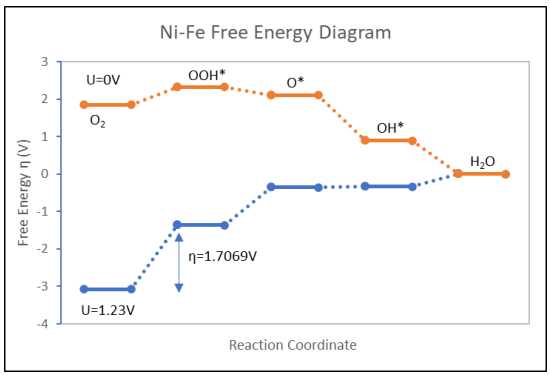
Ni-Fe Free Energy Diagram
U=0V
OOH*
O*
OH*
O_2
H_2O
η=1.7069V
U=1.23V
Free Energy η (V)
Reaction Coordinate

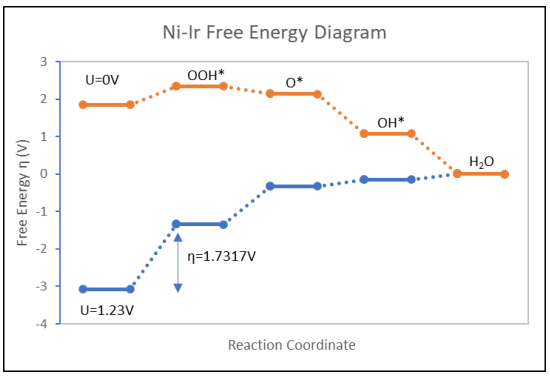
Ni-Ir Free Energy Diagram
U=0V
OOH*
O*
OH*
H_2O
η=1.7317V
U=1.23V
Free Energy η (V)
Reaction Coordinate

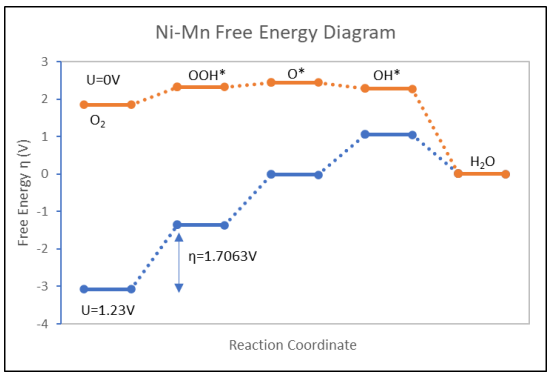
Ni-Mn Free Energy Diagram
U=0V
OOH*
O*
OH*
O_2
H_2O
η=1.7063V
U=1.23V
Free Energy η (V)
Reaction Coordinate

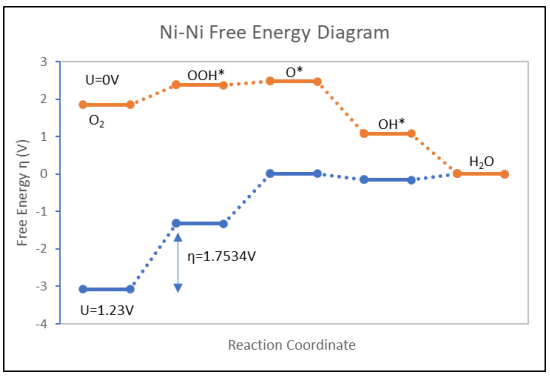
Ni-Ni Free Energy Diagram
U=0V
OOH*
O*
OH*
O_2
H_2O
η=1.7534V
U=1.23V
Free Energy η (V)
Reaction Coordinate

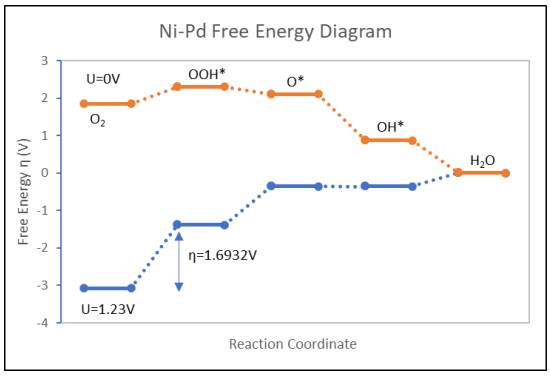
Ni-Pd Free Energy Diagram
U=0V
OOH*
O*
OH*
O_2
H_2O
η=1.6932V
U=1.23V
Free Energy η (V)
Reaction Coordinate

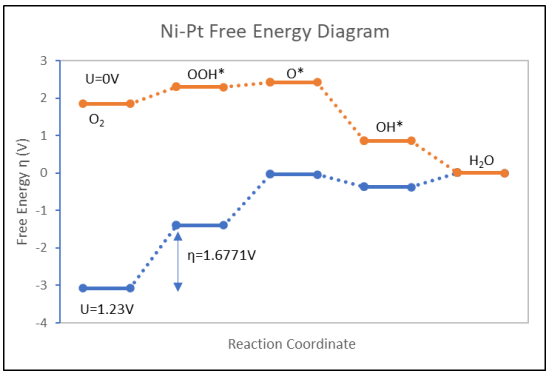
Ni-Pt Free Energy Diagram
U=0V
OOH*
O*
OH*
O_2
H_2O
η=1.6771V
U=1.23V
Free Energy η (V)
Reaction Coordinate

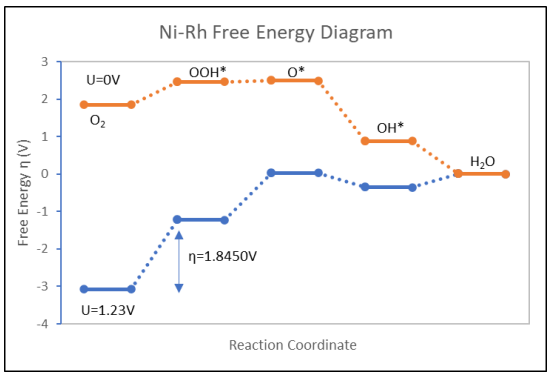
Ni-Rh Free Energy Diagram
U=0V
OOH*
O*
OH*
O_2
H_2O
η=1.8450V
U=1.23V
Free Energy η (V)
Reaction Coordinate

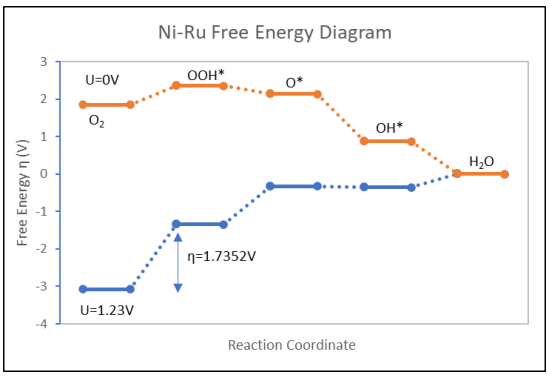
Ni-Ru Free Energy Diagram
U=0V
OOH*
O*
OH*
O_2
H_2O
η=1.7352V
U=1.23V
Free Energy η (V)
Reaction Coordinate

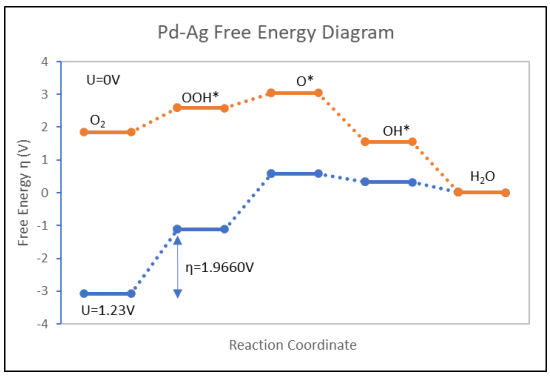
Pd-Ag Free Energy Diagram
U=0V
O2
OOH*
O*
OH*
H2O
η=1.9660V
U=1.23V
Free Energy η (V)
Reaction Coordinate

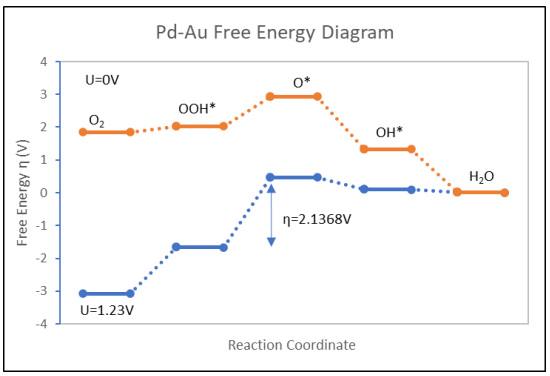
Pd-Au Free Energy Diagram
U=0V
O2
OOH*
O*
OH*
H2O
η=2.1368V
U=1.23V
Free Energy η (V)
Reaction Coordinate

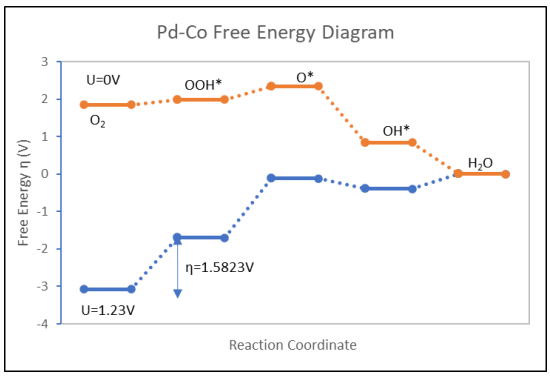
Pd-Co Free Energy Diagram
U=0V
O2
OOH*
O*
OH*
H2O
η=1.5823V
U=1.23V
Free Energy η (V)
Reaction Coordinate

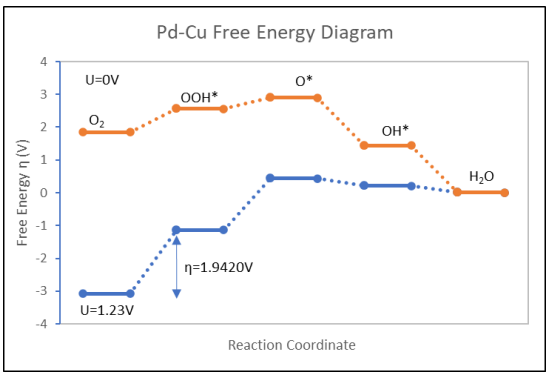
Pd-Cu Free Energy Diagram
U=0V
O2
OOH*
O*
OH*
H2O
η=1.9420V
U=1.23V
Free Energy η (V)
Reaction Coordinate

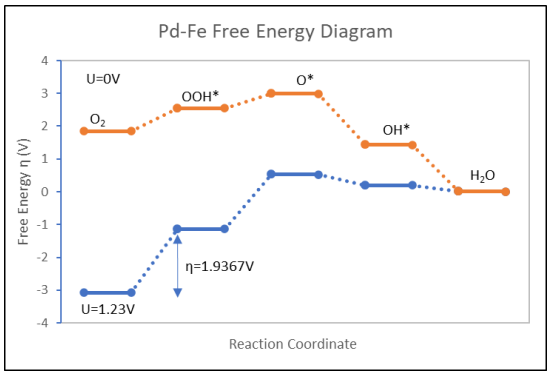
Pd-Fe Free Energy Diagram
U=0V
O2
OOH*
O*
OH*
H2O
η=1.9367V
U=1.23V
Free Energy η (V)
Reaction Coordinate

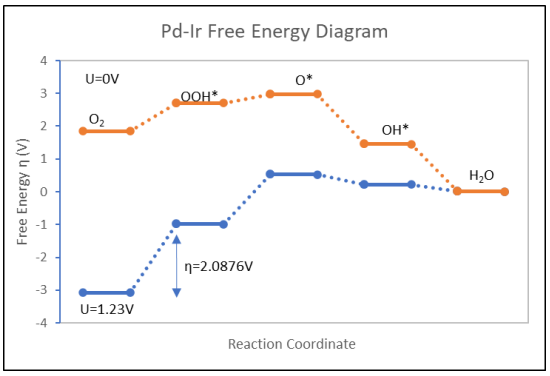
Pd-Ir Free Energy Diagram
U=0V
O2
OOH*
O*
OH*
H2O
η=2.0876V
U=1.23V
Free Energy η (V)
Reaction Coordinate

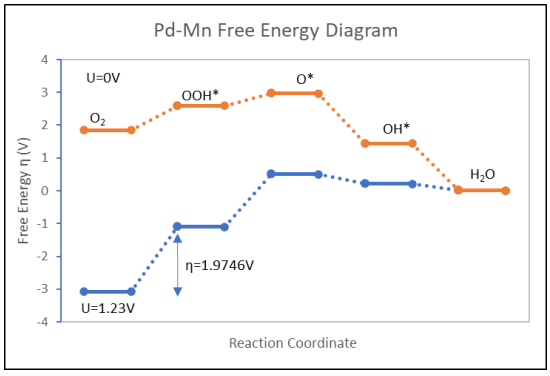
Pd-Mn Free Energy Diagram
U=0V
O2
OOH*
O*
OH*
H2O
η=1.9746V
U=1.23V
Free Energy η (V)
Reaction Coordinate

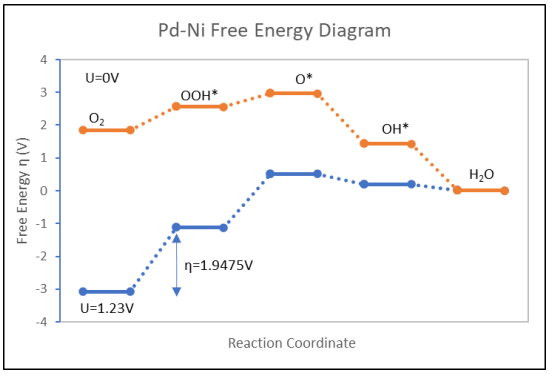
Pd-Ni Free Energy Diagram
U=0V
O2
OOH*
O*
OH*
H2O
η=1.9475V
U=1.23V
Free Energy η (V)
Reaction Coordinate

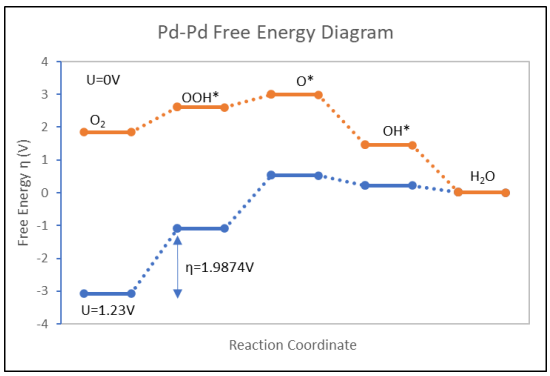
Pd-Pd Free Energy Diagram
U=0V
O2
OOH*
O*
OH*
H2O
η=1.9874V
U=1.23V
Free Energy η (V)
Reaction Coordinate

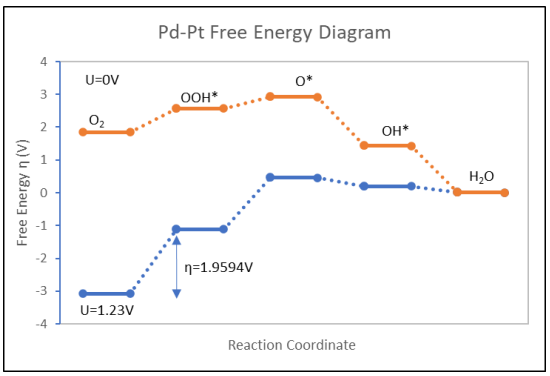
Pd-Pt Free Energy Diagram
U=0V
O2
OOH*
O*
OH*
H2O
η=1.9594V
U=1.23V
Free Energy η (V)
Reaction Coordinate

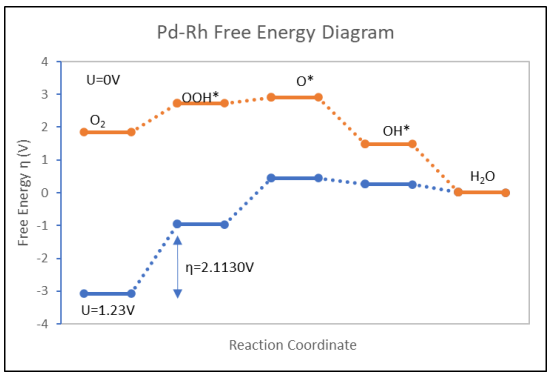
Pd-Rh Free Energy Diagram
U=0V
O2
OOH*
O*
OH*
H2O
η=2.1130V
U=1.23V
Free Energy η (V)
Reaction Coordinate

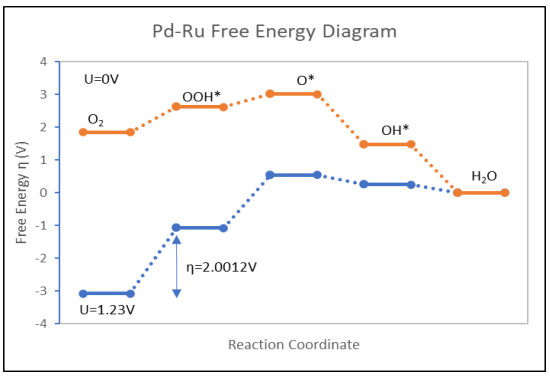
Pd-Ru Free Energy Diagram
U=0V
O2
OOH*
O*
OH*
H2O
η=2.0012V
U=1.23V
Free Energy η (V)
Reaction Coordinate

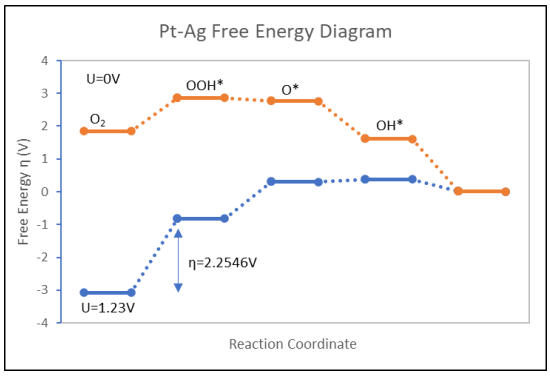
Pt-Ag Free Energy Diagram
U=0V
O2
OOH*
O*
OH*
η=2.2546V
U=1.23V
Free Energy η (V)
Reaction Coordinate

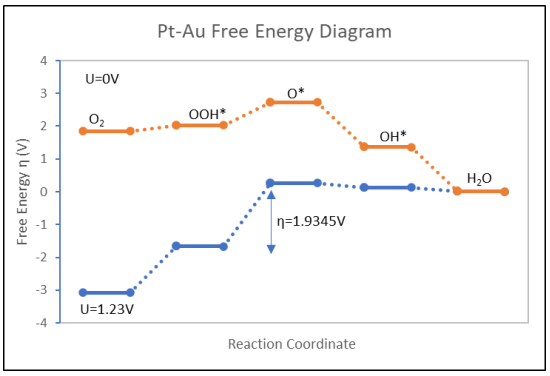
Pt-Au Free Energy Diagram
U=0V
O2
OOH*
O*
OH*
H2O
η=1.9345V
U=1.23V
Free Energy η (V)
Reaction Coordinate

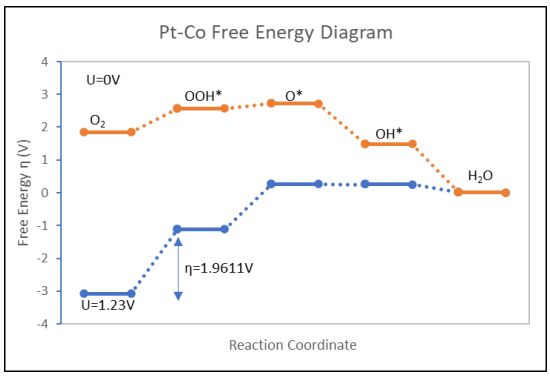
Pt-Co Free Energy Diagram
U=0V
O2
OOH*
O*
OH*
H2O
η=1.9611V
U=1.23V
Free Energy η (V)
Reaction Coordinate

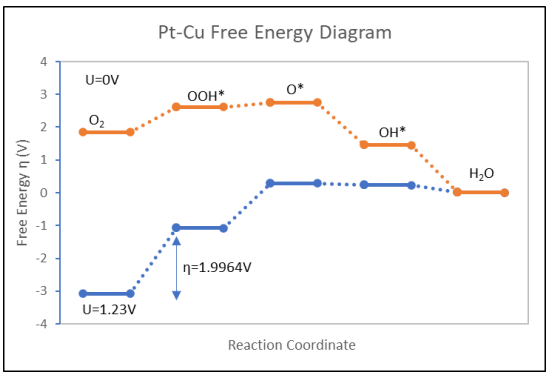
Pt-Cu Free Energy Diagram
U=0V
O2
OOH*
O*
OH*
H2O
η=1.9964V
U=1.23V
Free Energy η (V)
Reaction Coordinate

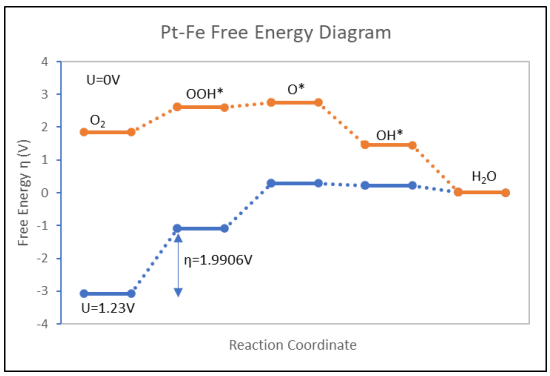
Pt-Fe Free Energy Diagram
U=0V
OOH*
O*
O2
OH*
H2O
η=1.9906V
U=1.23V
Free Energy η (V)
Reaction Coordinate

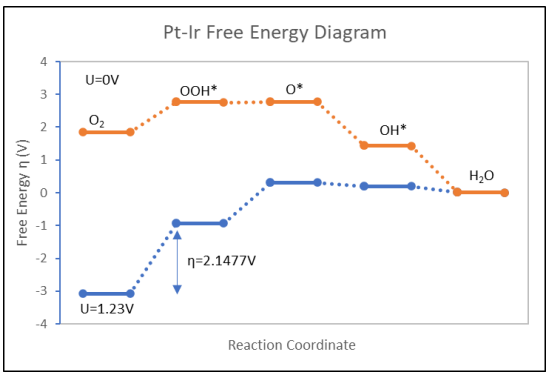
Pt-Ir Free Energy Diagram
U=0V
OOH*
O*
O2
OH*
H2O
η=2.1477V
U=1.23V
Free Energy η (V)
Reaction Coordinate

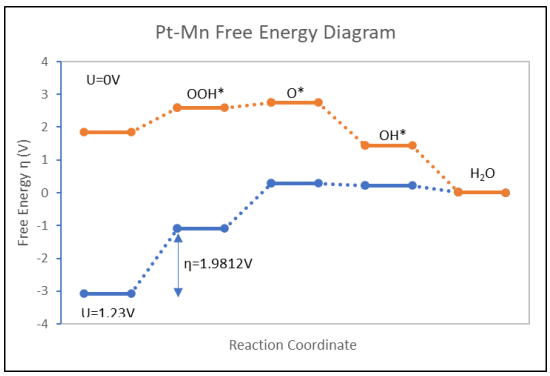
Pt-Mn Free Energy Diagram
U=0V
OOH*
O*
OH*
H2O
η=1.9812V
Free Energy η (V)
Reaction Coordinate

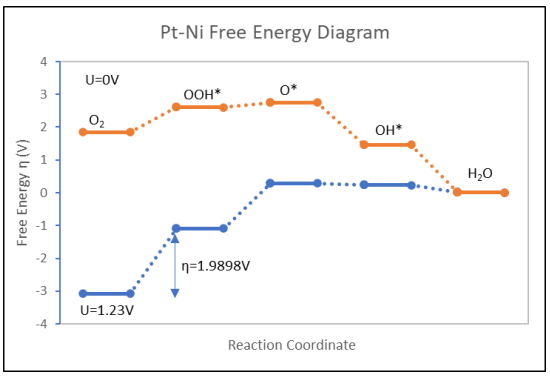
Pt-Ni Free Energy Diagram
U=0V
OOH*
O*
O2
OH*
H2O
η=1.9898V
U=1.23V
Free Energy η (V)
Reaction Coordinate

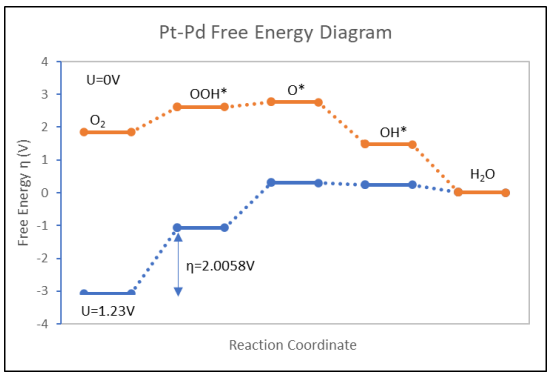
Pt-Pd Free Energy Diagram
U=0V
OOH*
O*
O2
OH*
H2O
η=2.0058V
U=1.23V
Free Energy η (V)
Reaction Coordinate

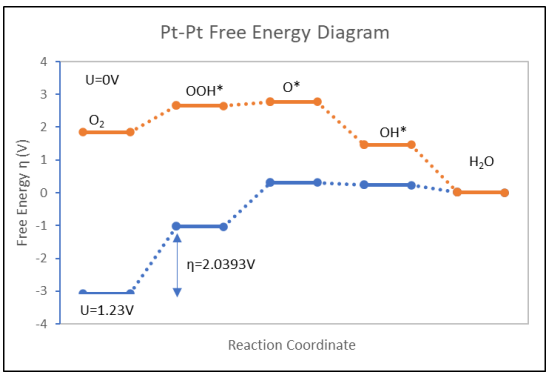
Pt-Pt Free Energy Diagram
U=0V
OOH*
O*
O2
OH*
H2O
η=2.0393V
U=1.23V
Free Energy η (V)
Reaction Coordinate

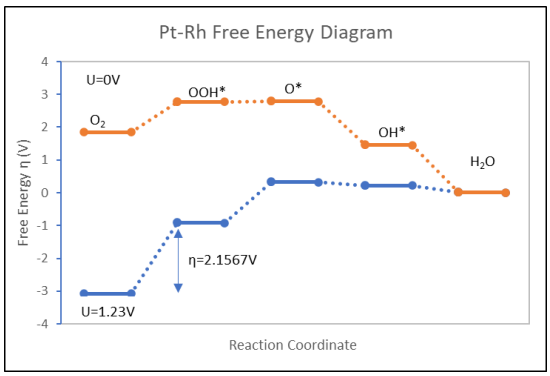
Pt-Rh Free Energy Diagram
U=0V
OOH*
O*
O2
OH*
H2O
η=2.1567V
U=1.23V
Free Energy η (V)
Reaction Coordinate

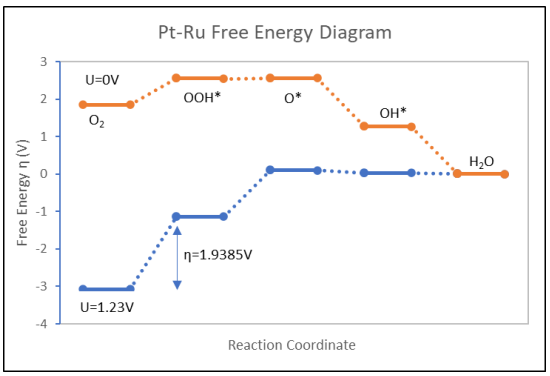
Pt-Ru Free Energy Diagram
U=0V
OOH*
O*
O2
OH*
H2O
η=1.9385V
U=1.23V
Free Energy η (V)
Reaction Coordinate

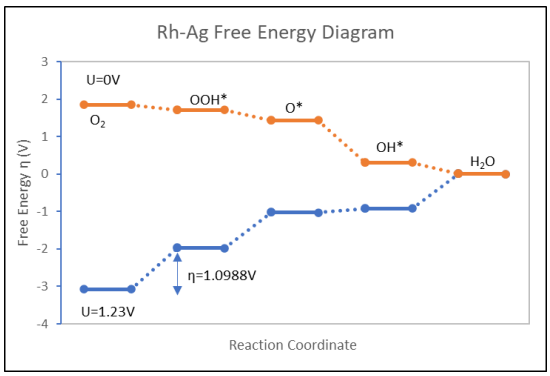
Rh-Ag Free Energy Diagram
U=0V
OOH*
O*
OH*
H2O
O2
η=1.0988V
U=1.23V
Free Energy η (V)
Reaction Coordinate

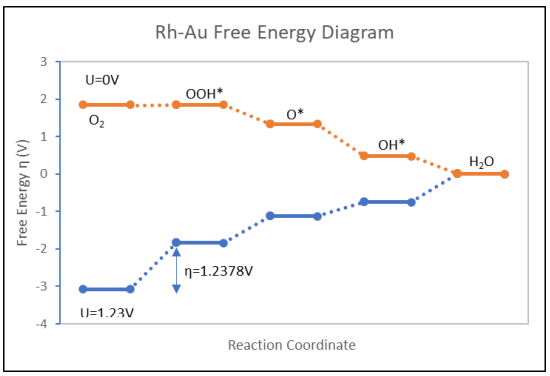
Rh-Au Free Energy Diagram
U=0V
OOH*
O*
OH*
H2O
O2
η=1.2378V
Free Energy η (V)
Reaction Coordinate

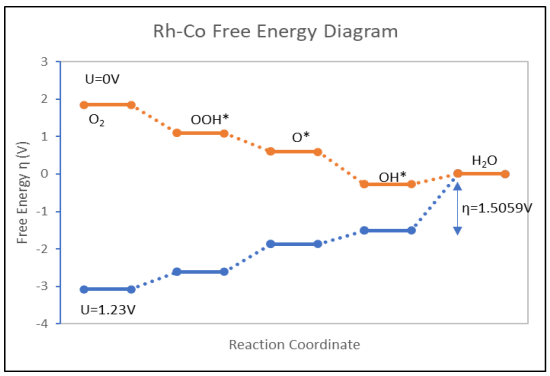
Rh-Co Free Energy Diagram
U=0V
OOH*
O*
OH*
H2O
O2
η=1.5059V
U=1.23V
Free Energy η (V)
Reaction Coordinate

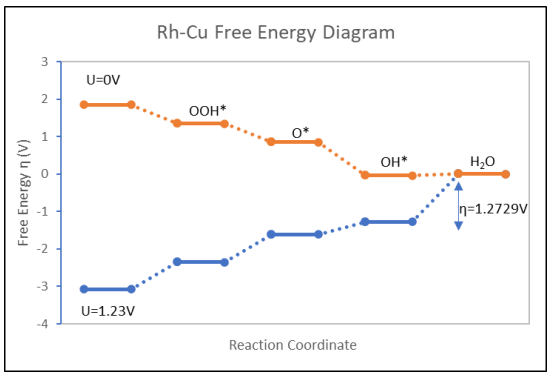
Rh-Cu Free Energy Diagram
U=0V
OOH*
O*
OH*
H2O
η=1.2729V
U=1.23V
Free Energy η (V)
Reaction Coordinate

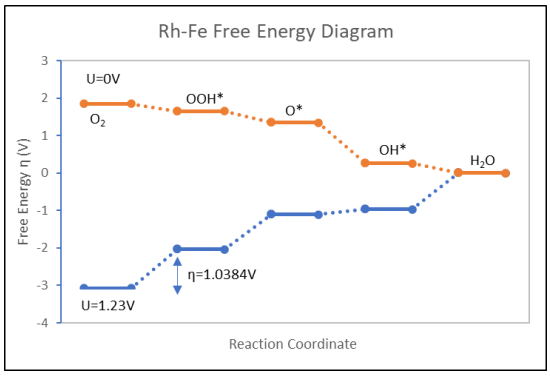
Rh-Fe Free Energy Diagram
U=0V
OOH*
O*
OH*
H2O
O2
η=1.0384V
U=1.23V
Free Energy η (V)
Reaction Coordinate

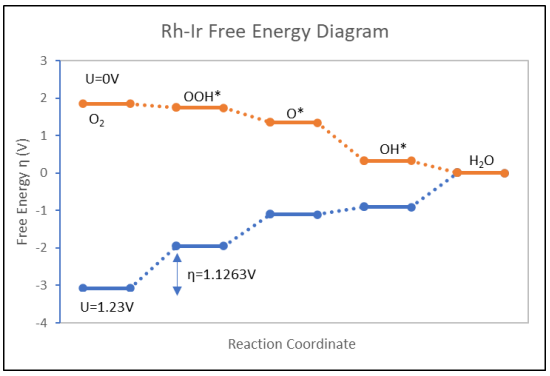
Rh-Ir Free Energy Diagram
U=0V
OOH*
O*
OH*
H2O
O2
η=1.1263V
U=1.23V
Free Energy η (V)
Reaction Coordinate

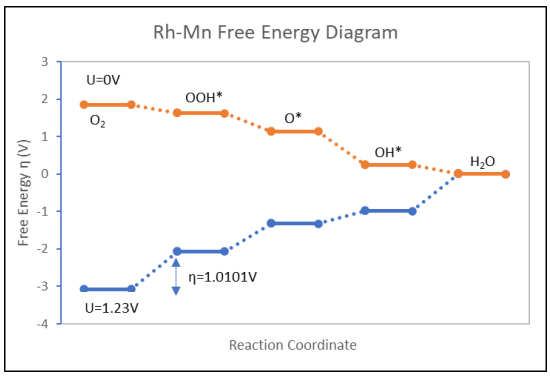
Rh-Mn Free Energy Diagram
U=0V
OOH*
O*
OH*
H2O
O2
η=1.0101V
U=1.23V
Free Energy η (V)
Reaction Coordinate

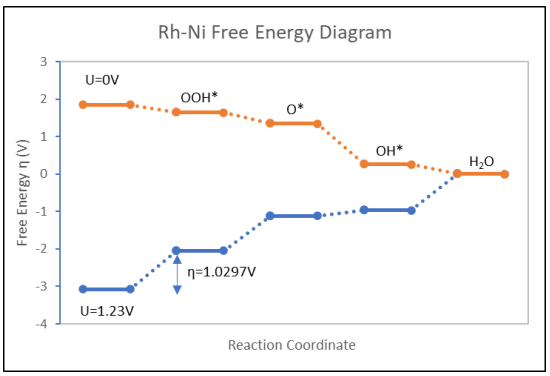
Rh-Ni Free Energy Diagram
U=0V
OOH*
O*
OH*
H2O
O2
η=1.0297V
U=1.23V
Free Energy η (V)
Reaction Coordinate

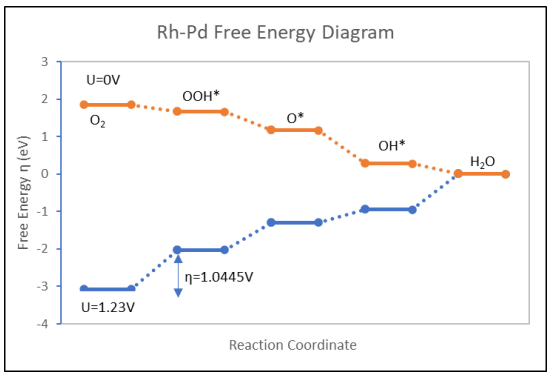
Rh-Pd Free Energy Diagram
U=0V
O2
OOH*
O*
OH*
H2O
η=1.0445V
U=1.23V
Free Energy η (eV)
Reaction Coordinate

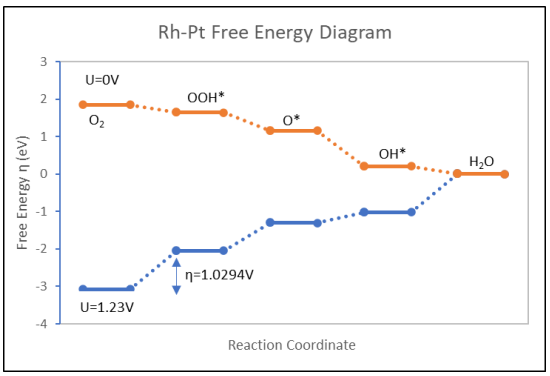
Rh-Pt Free Energy Diagram
U=0V
O2
OOH*
O*
OH*
H2O
η=1.0294V
U=1.23V
Free Energy η (eV)
Reaction Coordinate

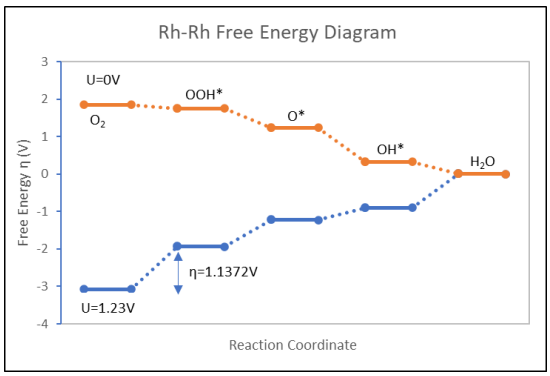
Rh-Rh Free Energy Diagram
U=0V
O2
OOH*
O*
OH*
H2O
η=1.1372V
U=1.23V
Free Energy η (V)
Reaction Coordinate

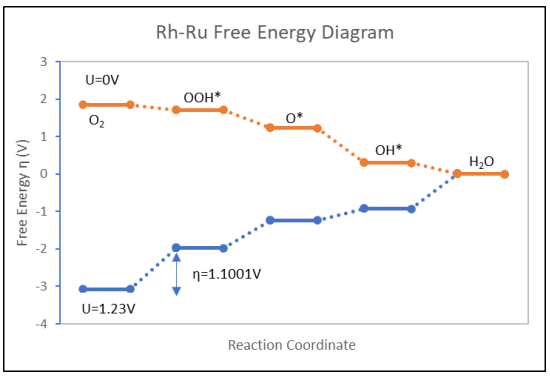
Rh-Ru Free Energy Diagram
U=0V
O2
OOH*
O*
OH*
H2O
η=1.1001V
U=1.23V
Free Energy η (V)
Reaction Coordinate

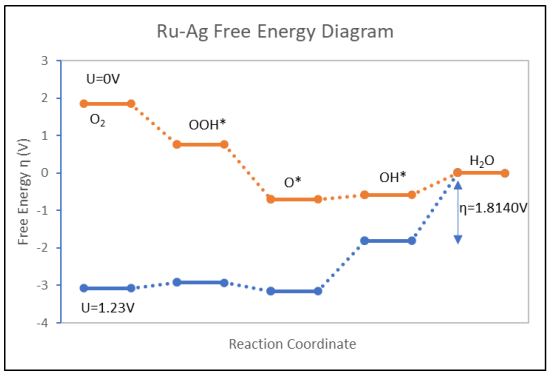
Ru-Ag Free Energy Diagram
U=0V
O2
OOH*
O*
OH*
H2O
η=1.8140V
U=1.23V
Free Energy η (V)
Reaction Coordinate

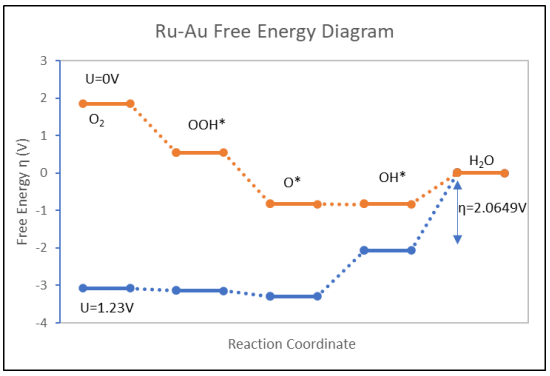
Ru-Au Free Energy Diagram
U=0V
O2
OOH*
O*
OH*
H2O
η=2.0649V
U=1.23V
Free Energy η (V)
Reaction Coordinate

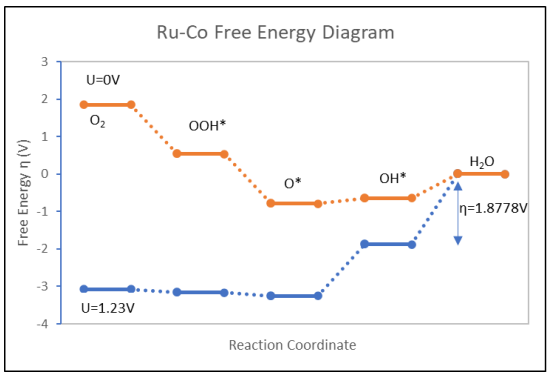
Ru-Co Free Energy Diagram
U=0V
O2
OOH*
O*
OH*
H2O
η=1.8778V
U=1.23V
Free Energy η (V)
Reaction Coordinate

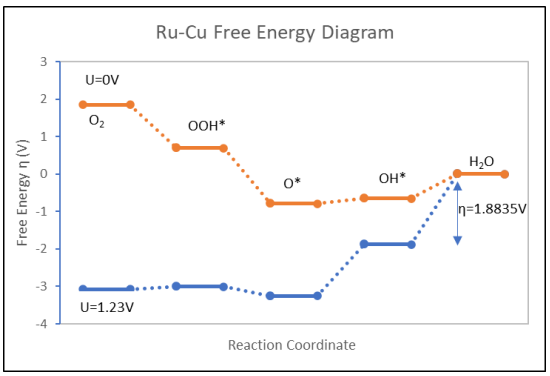
Ru-Cu Free Energy Diagram
U=0V
O2
OOH*
O*
OH*
H2O
η=1.8835V
U=1.23V
Free Energy η (V)
Reaction Coordinate

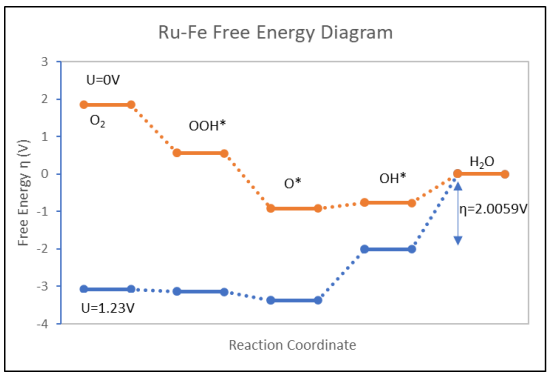
Ru-Fe Free Energy Diagram
Free Energy η (V)
Reaction Coordinate
U=0V
O2
OOH*
O*
OH*
H2O
η=2.0059V
U=1.23V

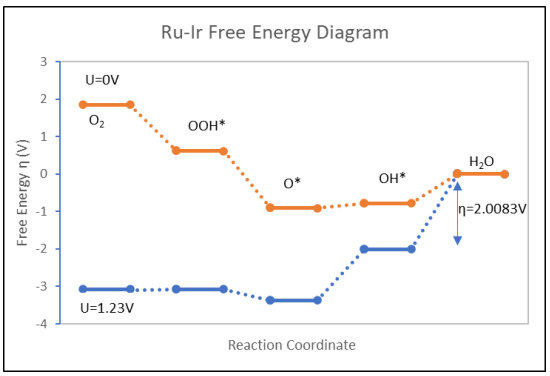
Ru-Ir Free Energy Diagram
Free Energy η (V)
Reaction Coordinate
U=0V
O2
OOH*
O*
OH*
H2O
η=2.0083V
U=1.23V

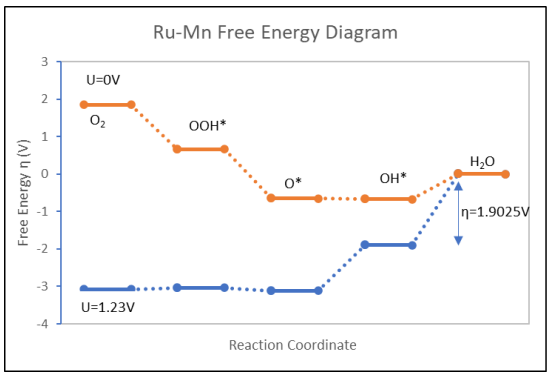
Ru-Mn Free Energy Diagram
Free Energy η (V)
Reaction Coordinate
U=0V
O2
OOH*
O*
OH*
H2O
η=1.9025V
U=1.23V

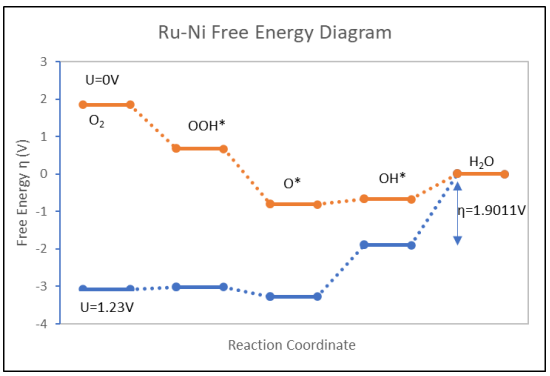
Ru-Ni Free Energy Diagram
Free Energy η (V)
Reaction Coordinate
U=0V
O2
OOH*
O*
OH*
H2O
η=1.9011V
U=1.23V

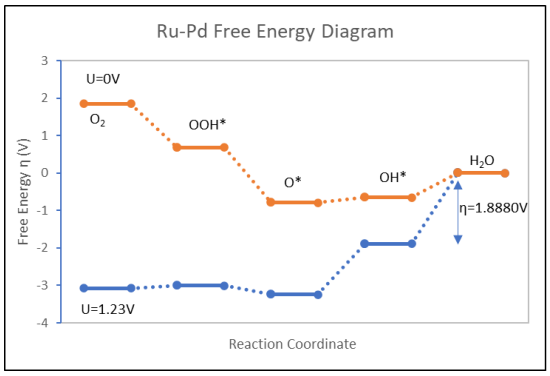
Ru-Pd Free Energy Diagram
Free Energy η (V)
Reaction Coordinate
U=0V
O2
OOH*
O*
OH*
H2O
η=1.8880V
U=1.23V

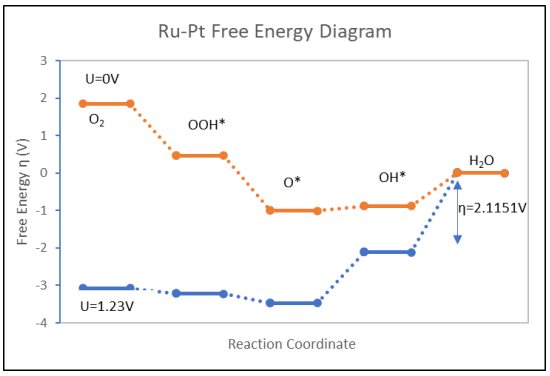
Ru-Pt Free Energy Diagram
Free Energy η (V)
Reaction Coordinate
U=0V
O2
OOH*
O*
OH*
H2O
η=2.1151V
U=1.23V

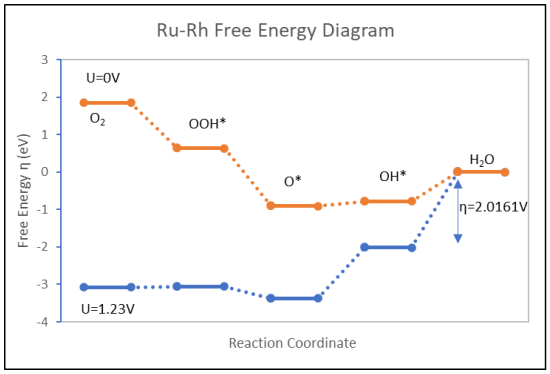
Ru-Rh Free Energy Diagram
Free Energy η (eV)
Reaction Coordinate
U=0V
O2
OOH*
O*
OH*
H2O
η=2.0161V
U=1.23V

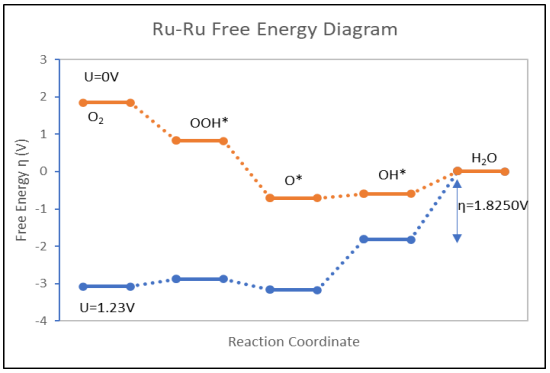
Ru-Ru Free Energy Diagram
Free Energy η (V)
Reaction Coordinate
U=0V
O2
OOH*
O*
OH*
H2O
η=1.8250V
U=1.23V

7.6. Appendix 5. DFT-computed data on reaction intermediate binding free energies and intrinsic/electronic features of catalysts.

M1-M2	Overpotential η	ΔG_{OOH*}	ΔG_{OH*}	ΔG_{O*}	Ionization (M1)	Ionization (M2)	HOMO-LUMO Gap Up	HOMO-LUMO Gap Down	d-band Spin Up	d-band Spin Down	Spin Density (M1)	Spin Density (M2)	Partial Charge (M1)	Partial-Charge (M2)	Electro-negativity (M1)	Electro-negativity (M2)	Atomic Radius (M1)	Atomic Radius (M2)	Atomic Mass (M1)	Atomic Mass (M2)
Ag-Ag	1.1749	1.7297	0.2292	1.6746	7.5800	7.5800	0.0060	0.1500	-4.7940	-4.7940	-0.6621	0.6614	0.5173	0.5411	1.9300	1.9300	165.0000	165.0000	107.8680	107.8680
Ag-Au	1.4445	1.7121	0.2015	1.9265	7.5800	7.8800	0.0250	0.0250	-2.8700	-2.8700	0.0000	0.0000	0.3323	0.6113	1.9300	2.5400	165.0000	174.0000	107.8680	196.9665
Ag-Co	1.5426	1.1576	-0.3126	1.0463	7.5800	7.7300	0.0880	0.0060	-4.6300	-4.9070	-0.6809	-0.0051	0.5507	0.1785	1.9300	1.8800	165.0000	152.0000	107.8680	58.9332
Ag-Cu	1.1528	1.7445	0.3085	1.6673	7.5800	7.9000	0.2000	0.0680	-4.5090	-4.8320	-0.6708	-0.6857	0.5222	0.5824	1.9300	1.9000	165.0000	145.0000	107.8680	63.5460
Ag-Fe	1.6780	1.6720	0.2039	2.1200	7.5800	8.9700	0.0060	0.0060	-4.9940	-4.9950	-0.0005	2.1582	0.5435	0.5610	1.9300	1.8300	165.0000	156.0000	107.8680	55.8470
Ag-Ir	1.2865	1.9003	0.5697	1.8779	7.5800	7.6400	0.0130	0.0130	-4.9370	-4.9380	0.0000	0.0000	0.5559	-0.0101	1.9300	2.2000	165.0000	180.0000	107.8680	192.2170
Ag-Mn	1.4165	1.6440	0.1328	1.8305	7.5800	8.3400	0.0060	0.0060	-4.9950	-4.9950	0.0006	3.4478	0.5438	0.7104	1.9300	1.5500	165.0000	161.0000	107.8680	54.9380
Ag-Ni	1.5848	1.6395	0.1661	1.9943	7.5800	7.4300	0.0060	0.0060	-5.0260	-5.0250	0.0006	0.0000	0.5472	0.3437	1.9300	1.9100	165.0000	149.0000	107.8680	58.7000
Ag-Pd	1.1451	1.6716	0.2302	1.5866	7.5800	8.9600	0.0060	0.0060	-4.9000	-4.9000	0.0001	0.0000	0.5347	0.3187	1.9300	2.2000	165.0000	169.0000	107.8680	106.4000
Ag-Pt	1.5843	1.8744	0.3563	2.2287	7.5800	7.4600	0.1560	0.2250	-4.7480	-4.4320	0.6469	-0.0004	0.5257	0.2690	1.9300	2.2800	165.0000	177.0000	107.8680	195.0900
Ag-Rh	1.3848	1.9985	0.6300	1.9615	7.5800	7.3600	0.0060	0.0060	-4.4700	-4.7710	-0.6310	0.0091	0.5357	0.0301	1.9300	2.2800	165.0000	173.0000	107.8680	102.9055
Ag-Ru	1.2828	1.8966	0.5314	1.8361	7.5800	9.2300	0.0060	0.0060	-4.7850	-4.4860	0.5212	1.6102	0.5365	0.3016	1.9300	2.2000	165.0000	178.0000	107.8680	101.0700
Au-Ag	1.9071	2.5208	1.2618	2.6831	7.8800	7.5800	0.1940	0.1940	-5.8320	-5.8320	0.0000	0.0000	0.5864	0.3555	2.5400	1.9300	174.0000	165.0000	196.9665	107.8680
Au-Au	1.2366	1.8503	0.8814	1.3988	7.8800	7.8800	0.0060	0.0060	-6.2450	-6.2450	0.0001	0.0000	0.5846	0.6147	2.5400	2.5400	174.0000	174.0000	196.9665	196.9665
Au-Co	1.6478	2.0838	0.8226	2.5016	7.8800	7.7300	0.3630	0.3630	-5.7620	-5.7620	0.0000	-0.0023	0.5921	0.1580	2.5400	1.8800	174.0000	152.0000	196.9665	58.9332
Au-Cu	2.0955	2.7092	1.0234	2.6883	7.8800	7.9000	0.0070	0.0070	-6.2430	-6.2390	0.0149	-0.7901	0.5846	0.5799	2.5400	1.9000	174.0000	145.0000	196.9665	63.5460
Au-Fe	1.6652	2.2402	1.0086	2.6754	7.8800	8.9700	0.0070	0.3320	-6.2680	-6.2550	0.0263	2.3685	0.5819	0.5627	2.5400	1.8300	174.0000	156.0000	196.9665	55.8470
Au-Ir	1.8516	2.4645	1.3938	3.0861	7.8800	7.6400	0.3560	0.3560	-5.7500	-5.7500	0.0000	0.0000	0.5932	-0.0196	2.5400	2.2000	174.0000	180.0000	196.9665	192.2170
Au-Mn	1.7051	2.2354	1.0019	2.7106	7.8800	8.3400	0.0070	0.2880	-6.2670	-6.2570	0.0256	3.5718	0.5832	0.7089	2.5400	1.5500	174.0000	161.0000	196.9665	54.9380
Au-Ni	1.6020	2.2157	1.0298	0.8050	7.8800	7.4300	0.0060	0.0060	-6.2990	-6.2990	0.0000	0.0000	0.5897	0.3472	2.5400	1.9100	174.0000	149.0000	196.9665	58.7000
Au-Pd	2.0734	2.2626	1.0362	3.1060	7.8800	8.9600	0.0070	0.0070	-6.1430	-6.1490	-0.0163	0.0002	0.5700	0.3198	2.5400	2.2000	174.0000	169.0000	196.9665	106.4000
Au-Pt	2.0979	2.2649	1.0445	3.1328	7.8800	7.4600	0.0060	0.0060	-6.1200	-6.1180	-0.0009	0.0000	0.5673	0.2712	2.5400	2.2800	174.0000	177.0000	196.9665	195.0900
Au-Rh	2.1320	2.4707	1.3510	3.3727	7.8800	7.3600	0.3940	0.3940	-5.7170	-5.7170	0.0000	0.0000	0.5927	0.0322	2.5400	2.2800	174.0000	173.0000	196.9665	102.9055
Au-Ru	1.8340	2.4478	1.3321	2.9524	7.8800	9.2300	0.3930	0.0060	-5.9170	-5.9170	-0.0047	1.1442	0.5885	0.1956	2.5400	2.2000	174.0000	178.0000	196.9665	101.0700
Co-Ag	1.2241	1.8378	0.2263	0.6694	7.7300	7.5800	0.0060	0.0060	-1.3060	-2.9420	-1.1762	-0.5502	0.4062	0.5525	1.8800	1.9300	152.0000	165.0000	58.9332	107.8680
Co-Au	1.3032	1.1805	-0.0732	0.1121	7.7300	7.8800	0.1320	0.1250	-0.5050	-0.5060	-0.0007	0.0000	0.1462	0.6131	1.8800	2.5400	152.0000	174.0000	58.9332	196.9665
Co-Co	1.3361	1.3184	-0.1061	0.8392	7.7300	7.7300	0.2250	0.2500	-1.0720	-3.9750	-2.8541	-1.0985	0.6999	0.5458	1.8800	1.8800	152.0000	152.0000	58.9332	58.9332
Co-Cu	1.5058	1.3697	-0.2758	0.2833	7.7300	7.9000	0.2250	0.2560	-4.6680	-0.4150	2.8275	-0.7277	0.6347	0.5855	1.8800	1.9000	152.0000	145.0000	58.9332	63.5460
Co-Fe	1.2721	1.8858	0.4848	0.7446	7.7300	8.9700	0.2620	0.2190	-2.7780	-1.2580	1.0300	2.2334	0.5350	0.5569	1.8800	1.8300	152.0000	156.0000	58.9332	55.8470
Co-Ir	1.3119	1.9256	0.2159	1.8692	7.7300	7.6400	0.0060	0.0060	-2.7820	-1.2230	1.3486	0.2600	0.5412	-0.0008	1.8800	2.2000	152.0000	180.0000	58.9332	192.2170
Co-Mn	1.2512	1.8649	0.4439	0.7614	7.7300	8.3400	0.2560	0.2560	-2.7130	-1.0680	0.9209	3.5183	0.4083	0.7078	1.8800	1.5500	152.0000	161.0000	58.9332	54.9380
Co-Ni	1.3105	1.9242	0.4798	0.8141	7.7300	7.4300	0.2620	0.2560	-2.7630	-1.2490	1.1167	-0.0001	0.5390	0.3395	1.8800	1.9100	152.0000	149.0000	58.9332	58.7000
Co-Pd	1.7613	2.3751	0.4597	1.5771	7.7300	8.9600	0.2620	0.2500	-2.7080	-1.0740	1.0729	0.0002	0.4084	0.3187	1.8800	2.2000	152.0000	169.0000	58.9332	106.4000
Co-Pt	1.3097	1.9234	0.4992	0.7934	7.7300	7.4600	0.2810	0.2620	-2.7640	-1.2460	1.1168	-0.0001	0.5377	0.2696	1.8800	2.2800	152.0000	177.0000	58.9332	195.0900
Co-Rh	1.3245	1.3033	-0.0945	0.2342	7.7300	7.3600	0.0500	0.0500	-0.6810	-0.6910	-0.0053	-0.0010	0.1935	0.0382	1.8800	2.2800	152.0000	173.0000	58.9332	102.9055
Co-Ru	1.4978	2.1115	0.1897	0.8208	7.7300	9.2300	0.0060	0.0060	-1.0960	-2.7100	-1.0955	1.4771	0.4117	0.2939	1.8800	2.2000	152.0000	178.0000	58.9332	101.0700
Cu-Ag	1.7401	2.3538	1.1384	2.6144	7.9000	7.5800	0.0060	0.0060	-4.1200	-5.1640	-0.7263	0.6398	0.5689	0.5500	1.9000	1.9300	145.0000	165.0000	63.5460	107.8680
Cu-Au	1.5542	2.1679	0.7029	2.1199	7.9000	7.8800	0.0060	0.0060	-4.0760	-4.9950	-0.6366	0.0046	0.5324	0.6120	1.9000	2.5400	145.0000	174.0000	63.5460	196.9665
Cu-Co	1.4866	1.5247	0.9535	1.7813	7.9000	7.7300	0.2320	0.1940	-3.9720	-5.0290	-0.7377	2.8549	0.5738	0.7017	1.9000	1.8800	145.0000	152.0000	63.5460	58.9332
Cu-Cu	1.7432	2.3569	0.9668	2.5684	7.9000	7.9000	0.2380	0.2250	-4.5400	-4.5290	0.7429	-0.7341	0.5754	0.5829	1.9000	1.9000	145.0000	145.0000	63.5460	63.5460
Cu-Fe	1.6862	2.2999	0.9408	2.5620	7.9000	8.9700	0.2440	0.2250	-3.9700	-5.0340	-0.7689	2.1800	0.5752	0.5584	1.9000	1.8300	145.0000	156.0000	63.5460	55.8470
Cu-Ir	1.7037	2.3174	0.9561	2.7149	7.9000	7.6400	0.0060	0.0060	-5.0020	-3.9490	0.7976	0.2997	0.5850	0.0021	1.9000	2.2000	145.0000	180.0000	63.5460	192.2170
Cu-Mn	1.7477	2.3614	0.9408	2.5637	7.9000	8.3400	0.2380	0.2690	-3.9490	-5.0190	-0.8143	3.4150	0.5776	0.7099	1.9000	1.5500	145.0000	161.0000	63.5460	54.9380
Cu-Ni	1.7073	2.3210	0.9656	2.6610	7.9000	7.4300	0.2570	0.2440	-5.0370	-3.9660	0.7190	0.0002	0.5759	0.3405	1.9000	1.9100	145.0000	149.0000	63.5460	58.7000
Cu-Pd	1.7368	2.3505	0.9790	2.5823	7.9000	8.9600	0.2440	0.2560	-3.9790	-5.0390	-0.7196	0.0001	0.5789	0.3197	1.9000	2.2000	145.0000	169.0000	63.5460	106.4000
Cu-Pt	2.0071	2.6208	0.9746	2.5907	7.9000	7.4600	0.2630	0.2750	-3.9550	-5.0210	-0.7193	0.0003	0.5822	0.2689	1.9000	2.2800	145.0000	177.0000	63.5460	195.0900
Cu-Rh	1.5040	2.0316	0.6184	2.3056	7.9000	7.3600	0.0250	0.0250	-3.2980	-3.2980	0.0001	0.0000	0.4558	0.0464	1.9000	2.2800	145.0000	173.0000	63.5460	102.9055
Cu-Ru	1.7464	2.3601	0.7471	2.7377	7.9000	9.2300	0.0060	0.0060	-4.9970	-3.9410	0.6006	1.6648	0.5814	0.3076	1.9000	2.2000	145.0000	178.0000	63.5460	101.0700

Table A3. DFT-computed data (M_1 = Ag to Cu)

M1-M2	Overpotential η	ΔG_{OOH*}	ΔG_{OH*}	ΔG_{O*}	Ionization (M1)	Ionization (M2)	HOMO-LUMO Gap Up	HOMO-LUMO Gap Down	d-band Spin Up	d-band Spin Down	Spin Density (M1)	Spin Density (M2)	Partial Charge (M1)	Partial-Charge (M2)	Electro-negativity (M1)	Electro-negativity (M2)	Atomic Radius (M1)	Atomic Radius (M2)	Atomic Mass (M1)	Atomic Mass (M2)
Fe-Ag	1.0081	1.4962	0.3176	0.5395	8.9700	7.5800	0.2250	0.0060	-2.9690	0.0250	2.1766	-0.6710	0.5452	0.5494	1.8300	1.9300	156.0000	165.0000	55.8470	107.8680
Fe-Au	1.5196	0.9200	0.1965	1.2096	8.9700	7.8800	0.0060	0.0060	-3.3080	-0.3380	2.1789	0.0013	0.5498	0.6122	1.8300	2.5400	156.0000	174.0000	55.8470	196.9665
Fe-Co	1.5007	1.7236	-0.2707	0.5577	8.9700	7.7300	0.2570	0.2060	-2.7620	0.2000	2.2161	1.0263	0.5444	0.5065	1.8300	1.8800	156.0000	152.0000	55.8470	58.9332
Fe-Cu	1.2756	1.2194	-0.0456	0.1672	8.9700	7.9000	0.2320	0.1930	-4.7620	0.8290	3.9251	-0.7330	0.7652	0.5813	1.8300	1.9000	156.0000	145.0000	55.8470	63.5460
Fe-Fe	1.2594	1.8731	0.3186	0.6565	8.9700	8.9700	0.2560	0.1870	-2.8320	0.1320	2.1406	2.1507	0.5451	0.5564	1.8300	1.8300	156.0000	156.0000	55.8470	55.8470
Fe-Ir	1.3530	1.5815	-0.1230	0.6419	8.9700	7.6400	0.0060	0.0060	-2.7810	0.2250	2.4158	-0.0831	0.5546	-0.0153	1.8300	2.2000	156.0000	180.0000	55.8470	192.2170
Fe-Mn	1.9855	0.7695	0.5907	-0.1648	8.9700	8.3400	0.2310	0.2250	-2.7530	0.2100	2.3213	-1.2439	0.5455	0.6299	1.8300	1.5500	156.0000	161.0000	55.8470	54.9380
Fe-Ni	1.2345	1.8482	0.3317	0.5296	8.9700	7.4300	0.2560	0.2250	-2.7490	0.2320	2.1496	0.0001	0.5447	0.3391	1.8300	1.9100	156.0000	149.0000	55.8470	58.7000
Fe-Pd	0.9803	1.5940	0.3477	1.2681	8.9700	8.9600	0.2630	0.2130	-2.7510	0.2290	2.1499	0.0001	0.5462	0.3179	1.8300	2.2000	156.0000	169.0000	55.8470	106.4000
Fe-Pt	0.9835	1.5972	0.3480	0.9699	8.9700	7.4600	0.2750	0.2310	-2.7530	0.2220	2.1494	0.0001	0.5466	0.2686	1.8300	2.2800	156.0000	177.0000	55.8470	195.0900
Fe-Rh	1.3313	1.6118	-0.1013	1.3727	8.9700	7.3600	0.0060	0.0060	-2.8230	0.1850	2.2035	0.0023	0.5539	0.0218	1.8300	2.2800	156.0000	173.0000	55.8470	102.9055
Fe-Ru	1.3095	1.7665	-0.0795	0.6163	8.9700	9.2300	0.0060	0.0060	-2.7910	0.2090	2.1939	1.3650	0.5537	0.2839	1.8300	2.2000	156.0000	178.0000	55.8470	101.0700
Ir-Ag	1.1125	1.7262	0.3711	0.8894	7.6400	7.5800	0.2000	0.2000	-1.0960	-1.0960	0.0000	0.0000	-0.0225	0.5679	2.2000	1.9300	180.0000	165.0000	192.2170	107.8680
Ir-Au	1.2480	1.8617	0.4301	0.9997	7.6400	7.8800	0.1120	0.1120	-1.1460	-1.1460	0.0000	0.0000	-0.0400	0.6129	2.2000	2.5400	180.0000	174.0000	192.2170	196.9665
Ir-Co	1.5697	1.0973	-0.3397	0.2772	7.6400	7.7300	0.0320	0.0320	-1.2340	-1.2340	-0.0009	0.0011	-0.0004	0.1674	2.2000	1.8800	180.0000	152.0000	192.2170	58.9332
Ir-Cu	1.4475	2.0612	0.2324	0.8057	7.6400	7.9000	0.0070	0.0070	-1.1800	-1.2660	-0.2869	-0.7140	-0.0100	0.5926	2.2000	1.9000	180.0000	145.0000	192.2170	63.5460
Ir-Fe	1.0278	1.6416	0.2162	0.7962	7.6400	8.9700	0.0070	0.0070	-1.2120	-1.2140	-0.0176	2.2376	-0.0158	0.5665	2.2000	1.8300	180.0000	156.0000	192.2170	55.8470
Ir-Ir	1.1456	1.7593	0.3086	0.8255	7.6400	7.6400	0.0060	0.0060	-1.2110	-1.2110	-0.0001	-0.0001	0.0056	-0.0082	2.2000	2.2000	180.0000	180.0000	192.2170	192.2170
Ir-Mn	1.0374	1.6398	0.1926	0.7871	7.6400	8.3400	0.0060	0.0060	-1.2160	-1.2140	-0.0088	3.3892	-0.0119	0.7139	2.2000	1.5500	180.0000	161.0000	192.2170	54.9380
Ir-Ni	1.0182	1.6265	0.2118	0.7913	7.6400	7.4300	0.0060	0.0060	-1.2000	-1.2000	0.0012	0.0000	-0.0130	0.3513	2.2000	1.9100	180.0000	149.0000	192.2170	58.7000
Ir-Pd	1.0392	1.6529	0.2710	0.8123	7.6400	8.9600	0.0060	0.0060	-1.1850	-1.1850	-0.0009	0.0000	-0.0122	0.3229	2.2000	2.2000	180.0000	169.0000	192.2170	106.4000
Ir-Pt	1.0204	1.6341	0.2496	0.7973	7.6400	7.4600	0.0060	0.0060	-1.2080	-1.2080	0.0009	0.0000	-0.0073	0.2760	2.2000	2.2800	180.0000	177.0000	192.2170	195.0900
Ir-Rh	1.1571	1.7709	0.3222	0.8343	7.6400	7.3600	0.0630	0.0630	-1.2180	-1.2200	0.0000	0.0000	0.0053	0.0375	2.2000	2.2800	180.0000	173.0000	192.2170	102.9055
Ir-Ru	1.0788	1.5947	0.1512	0.7366	7.6400	9.2300	0.0060	0.0060	-1.3120	-1.2450	0.2249	-0.1561	0.0087	0.2465	2.2000	2.2000	180.0000	178.0000	192.2170	101.0700
Mn-Ag	1.2609	1.6311	-0.0309	0.2454	8.3400	7.5800	0.0880	0.2320	-3.9620	2.4870	5.1675	0.4464	0.7847	0.5436	1.5500	1.9300	161.0000	165.0000	54.9380	107.8680
Mn-Au	2.4169	0.4080	-1.1869	-0.7203	8.3400	7.8800	0.3120	0.0060	-0.0530	-1.5470	-1.1975	-0.0044	0.5535	0.6132	1.5500	2.5400	161.0000	174.0000	54.9380	196.9665
Mn-Co	2.1329	0.7906	-0.9029	0.2042	8.3400	7.7300	0.1940	0.2310	-1.8830	2.0010	3.1717	-1.1633	0.5886	0.4111	1.5500	1.8800	161.0000	152.0000	54.9380	58.9332
Mn-Cu	1.3288	1.4944	-0.0988	0.5591	8.3400	7.9000	0.2000	0.2380	-3.8360	2.5970	4.9104	-0.7281	0.7817	0.5797	1.5500	1.9000	161.0000	145.0000	54.9380	63.5460
Mn-Fe	1.4260	2.0397	-0.0539	0.3701	8.3400	8.9700	0.2690	0.0060	-3.2060	1.1750	3.4869	2.0167	0.6751	0.5564	1.5500	1.8300	161.0000	156.0000	54.9380	55.8470
Mn-Ir	1.6727	1.7671	-0.4427	0.6650	8.3400	7.6400	0.4000	0.0500	-4.3470	0.7160	3.9887	0.0484	0.8285	-0.0221	1.5500	2.2000	161.0000	180.0000	54.9380	192.2170
Mn-Mn	2.0961	0.2337	-0.7236	1.0998	8.3400	8.3400	0.2370	0.2560	-1.4600	0.0220	-1.3315	3.5683	0.5609	0.7098	1.5500	1.5500	161.0000	161.0000	54.9380	54.9380
Mn-Ni	1.9669	0.9666	-0.7369	0.3550	8.3400	7.4300	0.2750	0.0190	-3.2200	1.1630	3.3706	-0.0003	0.6784	0.3402	1.5500	1.9100	161.0000	149.0000	54.9380	58.7000
Mn-Pd	2.8953	-0.6637	-1.6653	-1.0032	8.3400	8.9600	0.0060	0.0060	-0.3900	-0.3820	0.0000	-0.0001	0.5257	0.3205	1.5500	2.2000	161.0000	169.0000	54.9380	106.4000
Mn-Pt	2.3375	0.4879	-1.1075	-0.6451	8.3400	7.4600	0.2560	0.2560	0.5280	-0.9560	-0.9809	-0.0001	0.5414	0.2689	1.5500	2.2800	161.0000	177.0000	54.9380	195.0900
Mn-Rh	1.1709	1.7846	0.1898	0.6659	8.3400	7.3600	0.3940	0.1130	-4.2950	0.7540	3.9928	0.0258	0.8251	0.0273	1.5500	2.2800	161.0000	173.0000	54.9380	102.9055
Mn-Ru	1.7153	1.2309	-0.4853	0.5753	8.3400	9.2300	0.3500	0.0070	-3.7610	1.0330	3.8087	1.2547	0.7633	0.2794	1.5500	2.2000	161.0000	178.0000	54.9380	101.0700
Ni-Ag	1.5547	2.1684	0.7624	1.9779	7.4300	7.5800	0.0060	0.0060	-2.8400	-2.8400	0.0000	0.0000	0.3363	0.5787	1.9100	1.9300	149.0000	165.0000	58.7000	107.8680
Ni-Au	1.7003	2.3140	0.5820	2.1709	7.4300	7.8800	0.0060	0.0060	-3.1330	-3.1330	0.0000	0.0000	0.3435	0.6145	1.9100	2.5400	149.0000	174.0000	58.7000	196.9665
Ni-Co	1.6640	2.2777	0.0885	1.3393	7.4300	7.7300	0.2000	0.2500	-2.5740	-2.5730	-0.0009	-2.8303	0.3342	0.6992	1.9100	1.8800	149.0000	152.0000	58.7000	58.9332
Ni-Cu	1.7043	2.3180	0.8980	2.1433	7.4300	7.9000	0.2500	0.2560	-2.5600	-2.5620	0.0001	0.7105	0.3343	0.5848	1.9100	1.9000	149.0000	145.0000	58.7000	63.5460
Ni-Fe	1.7069	2.3207	0.8911	2.1003	7.4300	8.9700	0.2620	0.2320	-2.5630	-2.5630	0.0001	2.1541	0.3354	0.5546	1.9100	1.8300	149.0000	156.0000	58.7000	55.8470
Ni-Ir	1.7318	2.3455	1.0809	2.1333	7.4300	7.6400	0.0060	0.0060	-2.5500	-2.5500	0.0000	-0.0021	0.3447	-0.0124	1.9100	2.2000	149.0000	180.0000	58.7000	192.2170
Ni-Mn	1.7063	2.3200	2.2736	2.4438	7.4300	8.3400	0.2690	0.2750	-2.5450	-2.5400	0.0016	3.4020	0.3363	0.7098	1.9100	1.5500	149.0000	161.0000	58.7000	54.9380
Ni-Ni	1.7534	2.3671	1.0722	2.4727	7.4300	7.4300	0.2630	0.2630	-2.6150	-2.6150	0.0000	0.0000	0.3353	0.3416	1.9100	1.9100	149.0000	149.0000	58.7000	58.7000
Ni-Pd	1.6932	2.3069	0.8721	2.1028	7.4300	8.9600	0.2690	0.2690	-2.5530	-2.5530	0.0000	0.0000	0.3381	0.3185	1.9100	2.2000	149.0000	169.0000	58.7000	106.4000
Ni-Pt	1.6771	2.2908	0.8565	2.4207	7.4300	7.4600	0.2880	0.2880	-2.5270	-2.5270	0.0000	0.0000	0.3399	0.2691	1.9100	2.2800	149.0000	177.0000	58.7000	195.0900
Ni-Rh	1.8450	2.4587	0.8772	2.4857	7.4300	7.3600	0.0060	0.0060	-2.5940	-2.5940	0.0000	0.0000	0.3418	0.0247	1.9100	2.2800	149.0000	173.0000	58.7000	102.9055
Ni-Ru	1.7352	2.3489	0.8731	2.1358	7.4300	9.2300	0.0060	0.0060	-2.5560	-2.5540	0.0040	1.4541	0.3402	0.2993	1.9100	2.2000	149.0000	178.0000	58.7000	101.0700

Table A4. DFT-computed data (M_1 = Fe to Ni)

M1-M2	Overpotential η	ΔG_{OOH*}	ΔG_{OH*}	ΔG_{O*}	Ionization (M1)	Ionization (M2)	HOMO-LUMO Gap Up	HOMO-LUMO Gap Down	d-band Spin Up	d-band Spin Down	Spin Density (M1)	Spin Density (M2)	Partial Charge (M1)	Partial-Charge (M2)	Electro-negativity (M1)	Electro-negativity (M2)	Atomic Radius (M1)	Atomic Radius (M2)	Atomic Mass (M1)	Atomic Mass (M2)
Pd-Ag	1.9660	2.5797	1.5497	3.0391	8.9600	7.5800	0.0060	0.0060	-3.0400	-3.0430	0.0001	0.6351	0.3011	0.5469	2.2000	1.9300	169.0000	165.0000	106.4000	107.8680
Pd-Au	2.1368	2.0268	1.3253	2.9337	8.9600	7.8800	0.0070	0.0070	-3.3630	-3.3630	0.0000	0.0000	0.3067	0.6154	2.2000	2.5400	169.0000	174.0000	106.4000	196.9665
Pd-Co	1.5823	1.9884	0.8370	2.3407	8.9600	7.7300	0.0070	0.0070	-2.8650	-2.8650	0.0001	-0.0001	0.3047	0.1598	2.2000	1.8800	169.0000	152.0000	106.4000	58.9332
Pd-Cu	1.9420	2.5557	1.4408	2.8996	8.9600	7.9000	0.2250	0.2250	-2.8500	-2.8500	0.0001	-0.7135	0.3003	0.5827	2.2000	1.9000	169.0000	145.0000	106.4000	63.5460
Pd-Fe	1.9367	2.5504	1.4298	2.9899	8.9600	8.9700	0.2370	0.2060	-2.8390	-2.8310	0.0005	2.1560	0.2990	0.5593	2.2000	1.8300	169.0000	156.0000	106.4000	55.8470
Pd-Ir	2.0876	2.7013	1.4469	2.9814	8.9600	7.6400	0.0070	0.0070	-2.8150	-2.8140	0.0001	-0.0002	0.3061	-0.0155	2.2000	2.2000	169.0000	180.0000	106.4000	192.2170
Pd-Mn	1.9746	2.5883	1.4432	2.9662	8.9600	8.3400	0.2370	0.2560	-2.8270	-2.8250	0.0017	3.4055	0.3029	0.7121	2.2000	1.5500	169.0000	161.0000	106.4000	54.9380
Pd-Ni	1.9475	2.5612	1.4240	2.9707	8.9600	7.4300	0.2430	0.2430	-2.8290	-2.8290	0.0000	0.0000	0.3026	0.3448	2.2000	1.9100	169.0000	149.0000	106.4000	58.7000
Pd-Pd	1.9874	2.6011	1.4481	2.9848	8.9600	8.9600	0.2380	0.2380	-2.9050	-2.9050	0.0000	0.0000	0.3020	0.3181	2.2000	2.2000	169.0000	169.0000	106.4000	106.4000
Pd-Pt	1.9594	2.5731	1.4235	2.9188	8.9600	7.4600	0.2560	0.2560	-2.7960	-2.7960	0.0000	0.0000	0.3032	0.2705	2.2000	2.2800	169.0000	177.0000	106.4000	195.0900
Pd-Rh	2.1130	2.7267	1.4889	2.9105	8.9600	7.3600	0.0060	0.0060	-2.8490	-2.8490	0.0000	0.0000	0.3053	0.0250	2.2000	2.2800	169.0000	173.0000	106.4000	102.9055
Pd-Ru	2.0012	2.6149	1.4745	3.0012	8.9600	9.2300	0.0070	0.0070	-2.8410	-2.8400	0.0050	1.4436	0.3043	0.2955	2.2000	2.2000	169.0000	178.0000	106.4000	101.0700
Pt-Ag	2.2546	2.8683	1.6066	2.7591	7.4600	7.5800	0.0070	0.0070	-2.8690	-2.8680	0.0008	-0.6350	0.2412	0.5451	2.2800	1.9300	177.0000	165.0000	195.0900	107.8680
Pt-Au	1.9345	2.0236	1.3595	2.7281	7.4600	7.8800	0.0060	0.0060	-3.2130	-3.2130	0.0000	0.0000	0.2477	0.6155	2.2800	2.5400	177.0000	174.0000	195.0900	196.9665
Pt-Co	1.9611	2.5748	1.4894	2.7202	7.4600	7.7300	0.2060	0.2380	-2.6830	-2.6830	-0.0020	-1.0732	0.2450	0.4159	2.2800	1.8800	177.0000	152.0000	195.0900	58.9332
Pt-Cu	1.9964	2.6101	1.4572	2.7482	7.4600	7.9000	0.2130	0.2120	-2.6870	-2.6860	0.0005	-0.7140	0.2439	0.5837	2.2800	1.9000	177.0000	145.0000	195.0900	63.5460
Pt-Fe	1.9906	2.6043	1.4548	2.7472	7.4600	8.9700	0.2370	0.2070	-2.6920	-2.6890	0.0008	2.1553	0.2420	0.5600	2.2800	1.8300	177.0000	156.0000	195.0900	55.8470
Pt-Ir	2.1477	2.7614	1.4298	2.7704	7.4600	7.6400	0.0060	0.0060	-2.6620	-2.6630	0.0000	-0.0003	0.2507	-0.0167	2.2800	2.2000	177.0000	180.0000	195.0900	192.2170
Pt-Mn	1.9812	2.5949	1.4459	2.7481	7.4600	8.3400	0.2440	0.2620	-2.6690	-2.6640	0.0029	3.4060	0.2447	0.7109	2.2800	1.5500	177.0000	161.0000	195.0900	54.9380
Pt-Ni	1.9898	2.6036	1.4625	2.7462	7.4600	7.4300	0.2440	0.2440	-2.6620	-2.6620	0.0000	0.0000	0.2445	0.3454	2.2800	1.9100	177.0000	149.0000	195.0900	58.7000
Pt-Pd	2.0058	2.6195	1.4707	2.7639	7.4600	8.9600	0.2250	0.2250	-2.6600	-2.6600	0.0000	0.0000	0.2435	0.3199	2.2800	2.2000	177.0000	169.0000	195.0900	106.4000
Pt-Pt	2.0393	2.6530	1.4657	2.7756	7.4600	7.4600	0.2500	0.2500	-2.7510	-2.7510	0.0000	0.0000	0.2462	0.2714	2.2800	2.2800	177.0000	177.0000	195.0900	195.0900
Pt-Rh	2.1567	2.7704	1.4547	2.7842	7.4600	7.3600	0.0060	0.0060	-2.6790	-2.6800	0.0000	0.0000	0.2512	0.0262	2.2800	2.2800	177.0000	173.0000	195.0900	102.9055
Pt-Ru	1.9385	2.5522	1.2604	2.5609	7.4600	9.2300	0.0070	0.0070	-2.7620	-2.7580	0.0079	-0.8052	0.2498	0.2124	2.2800	2.2000	177.0000	178.0000	195.0900	101.0700
Rh-Ag	1.0988	1.7126	0.3102	1.4349	7.3600	7.5800	0.1690	0.1690	-0.8490	-0.8490	0.0000	0.0000	0.0306	0.5739	2.2800	1.9300	173.0000	165.0000	102.9055	107.8680
Rh-Au	1.2378	1.8516	0.4741	1.3332	7.3600	7.8800	0.1190	0.1190	-0.8900	-0.8900	0.0000	0.0000	0.0147	0.6133	2.2800	2.5400	173.0000	174.0000	102.9055	196.9665
Rh-Co	1.5059	1.0838	-0.2759	0.5885	7.3600	7.7300	0.0620	0.0620	-1.0010	-1.0010	0.0001	0.0000	0.0463	0.1722	2.2800	1.8800	173.0000	152.0000	102.9055	58.9332
Rh-Cu	1.2729	1.3389	-0.0429	0.8463	7.3600	7.9000	0.1250	0.1250	-0.8740	-0.8740	-0.0001	0.0001	0.0401	0.4705	2.2800	1.9000	173.0000	145.0000	102.9055	63.5460
Rh-Fe	1.0384	1.6521	0.2589	1.3480	7.3600	8.9700	0.0060	0.0060	-0.9400	-0.9380	0.0038	2.1557	0.0219	0.5665	2.2800	1.8300	173.0000	156.0000	102.9055	55.8470
Rh-Ir	1.1263	1.7400	0.3219	1.3472	7.3600	7.6400	0.0130	0.0130	-1.0100	-1.0100	0.0000	0.0000	0.0506	-0.0072	2.2800	2.2000	173.0000	180.0000	102.9055	192.2170
Rh-Mn	1.0101	1.6238	0.2443	1.1385	7.3600	8.3400	0.0070	0.0070	-0.9540	-0.9340	0.0158	3.3983	0.0238	0.7118	2.2800	1.5500	173.0000	161.0000	102.9055	54.9380
Rh-Ni	1.0297	1.6435	0.2561	1.3464	7.3600	7.4300	0.0060	0.0060	-0.9310	-0.9310	0.0000	0.0000	0.0254	0.3500	2.2800	1.9100	173.0000	149.0000	102.9055	58.7000
Rh-Pd	1.0445	1.6582	0.2766	1.1663	7.3600	8.9600	0.0060	0.0060	-0.9220	-0.9220	0.0000	0.0000	0.0266	0.3225	2.2800	2.2000	173.0000	169.0000	102.9055	106.4000
Rh-Pt	1.0294	1.6431	0.2101	1.1532	7.3600	7.4600	0.0060	0.0060	-0.9120	-0.9120	0.0000	0.0000	0.0280	0.2734	2.2800	2.2800	173.0000	177.0000	102.9055	195.0900
Rh-Rh	1.1372	1.7510	0.3275	1.2351	7.3600	7.3600	0.0810	0.0810	-0.9320	-0.9320	0.0000	0.0000	0.0527	0.0409	2.2800	2.2800	173.0000	173.0000	102.9055	102.9055
Rh-Ru	1.1001	1.7138	0.2972	1.2231	7.3600	9.2300	0.1000	0.1930	-0.9480	-0.9200	0.0816	-1.3149	0.0519	0.2886	2.2800	2.2000	173.0000	178.0000	102.9055	101.0700
Ru-Ag	1.8140	0.7580	-0.5840	-0.6992	9.2300	7.5800	0.1500	0.0070	-1.1750	-0.4010	1.4848	-0.3893	0.2823	0.5661	2.2000	1.9300	178.0000	165.0000	101.0700	107.8680
Ru-Au	2.0649	0.5440	-0.8349	-0.8302	9.2300	7.8800	0.0060	0.0060	-0.5140	-0.5150	-0.0001	0.0000	0.1158	0.6158	2.2000	2.5400	178.0000	174.0000	101.0700	196.9665
Ru-Co	1.8778	0.5287	-0.6478	-0.7927	9.2300	7.7300	0.0060	0.0060	-0.4080	-1.1760	-1.4991	-2.7819	0.2610	0.7107	2.2000	1.8800	178.0000	152.0000	101.0700	58.9332
Ru-Cu	1.8838	0.6885	-0.6538	-0.7958	9.2300	7.9000	0.0060	0.0060	-1.1690	-0.3960	1.6433	0.5870	0.2665	0.5896	2.2000	1.9000	178.0000	145.0000	101.0700	63.5460
Ru-Fe	2.0059	0.5498	-0.7759	-0.9161	9.2300	8.9700	0.0060	0.0060	-1.1770	-0.4110	1.4126	2.0938	0.2637	0.4162	2.2000	1.8300	178.0000	156.0000	101.0700	55.8470
Ru-Ir	2.0083	0.6139	-0.7783	-0.9141	9.2300	7.6400	0.0060	0.0060	-0.7860	-0.6510	0.3817	-0.1868	0.2696	0.0037	2.2000	2.2000	178.0000	180.0000	101.0700	192.2170
Ru-Mn	1.9026	0.6583	-0.6726	-0.6544	9.2300	8.3400	0.0060	0.0060	-1.2520	-0.4300	1.4038	3.5398	0.3095	0.7039	2.2000	1.5500	178.0000	161.0000	101.0700	54.9380
Ru-Ni	1.9011	0.6697	-0.6711	-0.8089	9.2300	7.4300	0.0060	0.0060	-1.2010	-0.4070	1.5400	0.0003	0.2830	0.3475	2.2000	1.9100	178.0000	149.0000	101.0700	58.7000
Ru-Pd	1.8880	0.6849	-0.6580	-0.7873	9.2300	8.9600	0.0060	0.0060	-1.2170	-0.4230	1.5221	0.0008	0.2832	0.3214	2.2000	2.2000	178.0000	169.0000	101.0700	106.4000
Ru-Pt	2.1151	0.4677	-0.8851	-1.0129	9.2300	7.4600	0.0070	0.0070	-0.5140	-0.5150	0.0001	0.0000	0.1153	0.2783	2.2000	2.2800	178.0000	177.0000	101.0700	195.0900
Ru-Rh	2.0161	0.6314	-0.7861	-0.9077	9.2300	7.3600	0.0060	0.0060	-0.5600	-0.5580	0.0014	-0.0004	0.1189	0.0540	2.2000	2.2800	178.0000	173.0000	101.0700	102.9055
Ru-Ru	1.8250	0.8154	-0.5950	-0.7126	9.2300	9.2300	0.0070	0.0070	-0.8350	-0.8190	1.4260	-1.4044	0.3140	0.2938	2.2000	2.2000	178.0000	178.0000	101.0700	101.0700

Table A5. DFT-computed data (M_1 = Pd to Ru)